Etude du comportement dynamique des sources laser ultrarapides à base de fibres actives fortement dispersives

Mincheng Tang

Normandie Université

THÈSE

Pour obtenir le diplôme de doctorat

Spécialité PHYSIQUE

Préparée au sein de CORIA, Université de Rouen Normandie

Etude du comportement dynamique des sources laser ultrarapides à base de fibres actives fortement dispersives

Présentée et soutenue par
Mincheng TANG

Thèse soutenue publiquement le 23/06/2017 devant le jury composé de		
M. Thibaut SYLVESTRE	Directeur de Recherche, Institut FEMTO-ST, Besançon	Rapporteur
M. Sébastien FEVRIER	Maître de Conférences, XLIM, Université de Limoges	Rapporteur
M. Jean-Louis OUDAR	Directeur de Recherche, LPN, Marcoussis	Examinateur
M. Laurent BIGOT	Chargé de Recherche, PhLAM, Villeneuve d'Ascq	Examinateur
Mme. Angela VELLA	Professeur, GPM, Université de Rouen Normandie	Examinateur
M. Claude ROZE	Professeur, CORIA, Université de Rouen Normandie	Examinateur
M. Ammar HIDEUR	Maître de Conférences, CORIA, Université de Rouen Normandie	Directeur de thèse
M. Thomas GODIN	Maître de Conférences, CORIA, Université de Rouen Normandie	Coencadrant de thèse

Thèse dirigée par Ammar HIDEUR et Thomas GODIN, laboratoire CORIA

UNIVERSITÉ DE ROUEN NORMANDIE

SPM ECOLE DOCTORALE

UMR 6614 CORIA COMPLEXE DE RECHERCHE INTERPROFESSIONNEL EN AEROTHERMOCHIMIE

This page is intentionally left Blank.

Résumé

Les lasers ultra-rapides fibrés sont aujourd'hui incontournables dans de nombreuses applications industrielles et scientifiques du fait de leur stabilité, de leur compacité et des hautes puissances disponibles. Les performances actuelles, rendues accessibles par le développement de fibres à larges aires modales et le concept d'amplification à dérive de fréquence, sont toutefois complexes à mettre œuvre et limitées par l'utilisation de composants massifs pour les étapes de compression et d'étirement des impulsions. Ces travaux de thèse, à la fois expérimentaux et numériques, avaient pour objectif d'explorer des régimes dynamiques originaux basés sur l'utilisation de fibres actives spécifiques combinant large aire modale et propriétés dispersives adéquates pour la génération d'impulsions ultra-courtes de haute énergie. Les études numériques ont ainsi permis de montrer que des régimes impulsionnels à haute dispersion normale pouvaient être atteints en exploitant les phénomènes de résonnance et de couplage de modes dans des fibres de Bragg ou à profil en W. L'étude de l'influence des paramètres de la cavité laser sur le mécanisme de verrouillage de modes a permis d'identifier des configurations attractives pour la montée en puissance. La mise en œuvre expérimentale de ces concepts a notamment permis le développement d'une source laser à soliton dissipatif produisant des impulsions énergétiques (38 nJ, 700 fs après compression) à des longueurs d'ondes autour de 1560 nm, record pour ce type d'oscillateur. La réalisation expérimentale de sources ultra-rapides basées sur des fibres actives spécifiques combinées au phénomène de couplage de mode ont permis d'identifier les potentialités et limitations de ces architectures originales à fortes dispersions totales pour la montée en énergie.

Mots clés : laser à fibre, laser ultra-rapide, absorbant saturable à semi-conducteur, fibre de Bragg, haute énergie.

Abstract

Ultrafast fiber lasers represent today a ubiquitous technology in various industrial and research applications thanks to their inherent advantages such as compactness, stability and high power. The best performances to date, mostly relying on large mode area fibers and chirped pulse amplification, however require complex experimental developments and are limited by the use of bulk components for pulse stretching and compression. The experimental and numerical work presented in this PhD thesis aimed at exploring original dynamical regimes based on specific active fibers combining large mode area and high dispersions for the generation of high-energy ultra-short pulses. The numerical studies then showed that pulsed regimes with high normal dispersions could be reached by exploiting resonance and mode-coupling phenomena in Bragg or W-type fibers. Studying the influence of the cavity parameters on mode-locking mechanisms allowed to target attractive configurations for energy scaling. The experimental implementation of this concept allowed the development of a dissipative soliton source delivering record high-energy chirped pulses (38 nJ, 700 fs after compression) at 1560 nm. The realization of ultrafast sources based on specific active fibers combined to mode-coupling phenomena then brought the possibility to identify the potentiality and limitations of these particular architectures with high dispersions for energy scaling.

Keywords: fibre laser, ultrafast laser, semiconductor saturable absorber, Bragg fibre, high energy.

Index

List of figures

List of Tables

This page is intentionally left BLANK

Introduction

Applications of ultrafast pulsed radiation are increasingly based on fiber laser technology due to its inherent advantages such as compactness, stability, high power, and turn-key operation. Driven by several industrial and scientific applications such as material processing, nonlinear microscopy, precision metrology and high-field physics, the output power of ultrafast pulsed fiber laser systems has undergone an unparalleled growth during the past decade. This impressive growth was made possible thanks to the development of advanced fiber technologies offering extra-large mode areas in combination with novel pulse amplification schemes [1][2]. Indeed, the combination of large mode area fibers with the chirped pulse amplification scheme has already permitted the achievement of impressive performances in terms of average power and pulse energy from ultrafast fiber laser systems [3][4]. Moreover, the combination of spatial and temporal coherent pulse combination techniques with extra-large mode area fibers has led to record performances at high-repetition rates [5][6][7]. However, these high-energy laser systems are based on rod-type large mode area fibers, who leads to relatively cumbersome systems. The development of highly integrated all-fiber systems with energy levels matching requirements from industrial applications is another direction of research and has attracted much interest in recent years. In this context, research efforts concern the development of flexible large mode area fibers [8][9][10][11] or the exploitation of high order mode (HOM) fibers [12]. In particular, the combination of flexible large mode area fibers with the parabolic pulse amplification concept has led to high performances laser systems with relatively simplified architectures [13][14]. For applications in metrology and biophotonics, the noise figure of the laser system constitutes a key parameter which needs to be optimized. In general, the largely used master-oscillator power amplifier scheme leads to a degradation of the noise figure of the seed oscillator. So, the best way to meet this requirement consist to use mode-locked oscillators directly delivering high-energy ultrashort pulses. To achieve this goal, early studies especially from A Chong et al. [15][16], showed that it is possible to realized energy scaling in mode-locked fiber lasers via high normal intra-cavity dispersion. In particular, the combination of this concept with large mode area fibers has permitted the achievement of record performances at 1 μm and the production ultrashort pulses with more than 60 W average powers [17]. The dynamics of lasers in such regimes as well as the cavity parameters thereby need to be deeply studied in order to reach competitive performances. Moreover, the extension of these performances to flexible fiber-based lasers is highly desired to enlarge their use for industrial applications. This is the main goal of this thesis, which aims at investigating numerically and experimentally the dynamics of ultrafast sources based on high-dispersion

fibers. Specifically, this work focuses on the simulation and realization of high-energy mode-locked lasers by exploring original propagation regimes in specific active fibers (Bragg and W-type fibers) combining large mode area and high dispersion through a tailored modal coupling. This approach aims to explore the energy scaling potential of the parabolic pulse regimes inside a mode-locked oscillator. The development of such sources now requires a better understanding of the laser dynamics and pulse stabilization mechanisms within the laser cavity, which result of an overall balance between several linear and nonlinear processes. Investigation of the pulse dynamics within these new sources is thus essential to find optimal configurations that are favorable for energy scaling. The work presented in this thesis then aims at showing that ultrafast laser architectures based on high normal dispersions are promising candidates to answer the requirements of many industrial and research applications.

Outline of the thesis

My PhD studies have been carried out at the CORIA laboratory within the Optics and Lasers Department and have been focused on the development of original mode-locked lasers based on cavities featuring high normal dispersions introduced by particular active and passive components. This manuscript presents some of the work I have conducted during three years and is divided as follows.

In the **first Chapter**, a state-of-the-art of the different experimental techniques used nowadays for mode-locking of fiber lasers is presented as well as the dispersive and nonlinear processes involved in the propagation of ultra-short pulses in optical fibers. The theoretical basis used for modeling such phenomena is also described. In the frame of the energy scaling of such sources, methods based on active fibers featuring high normal dispersions are highlighted, as they constitute the keystone of the studies presented in next chapters.

The **second Chapter** will be focused on the detailed numerical study of the parameters and mechanisms driving the dynamics of mode-locked fiber lasers operating at high normal dispersion. The influence of parameters of components such as the saturable absorber, the intra-cavity spectral filtering and, in particular, of the dispersive elements is discussed. This work allows to highlight the key parameters stabilizing the pulsed regimes at high normal dispersion as well as the limits arising from high order dispersion terms. The simulations presented in this chapter pave the way for the identification of promising oscillator configurations for energy scaling.

The **third Chapter** reports the experimental development of an erbium-doped fiber laser featuring large normal dispersion provided by a long segment of passive fiber. The laser performances under different cavity configurations will be compared and the energy scaling

ability evolution with respect to the cavity dispersion will be carefully investigated. The stability of the source will also be analyzed through noise measurements. Finally, an application of this laser as a pump for an optical parametric oscillator delivering ps pulses around 1700nm will be presented.

The fourth Chapter will be dedicated to the experimental implementation of mode-locked lasers with cavities comprising specialty Yb-doped Bragg fibers and Er-doped W-type fibers allowing to obtain high normal dispersion through mode-coupling. The spatio-temporal characteristics of the output pulses will be studied when operating in different regimes, far or close to the resonance wavelength. The potentialities and limitations of such high-dispersion mode-locked oscillators in the frame of energy scaling will finally be discussed.

Chapter 1. High-energy mode-locked fiber lasers: fundamentals

The generation of ultra-short optical pulses relies mostly on mode-locked lasers which consists to lock the longitudinal modes of a laser cavity. The best performances in terms of pulse duration are obtained using passive mode-locking processes. For a fiber laser, mode-locking is a result of a delicate double balance between gain and losses in one hand, dispersion and Kerr nonlinearity on the other hand. Moreover, the nonlinear dissipation effects could play a key role in pulse stabilization notably when the overall intra-cavity dispersion is increased to high normal values. So, in this chapter, it will be first introduced some basics of nonlinear pulse propagation in fiber optics. As they are key elements in ultrafast lasers, the mode-locking mechanisms will also be concerned, among which the most frequently used mechanisms will be detailed. We will then review the main operation regimes observed in ultrafast fiber lasers with a focus on mode-locked lasers operating in the normal dispersion regime to get more insights about the main parameters impacting their performances. At the end of this chapter, we will introduce the high-dispersion fiber structures used in this work.

1.1 Pulse propagation in optical fibers

Ultrashort pulse propagation along a fiber optics waveguide is governed by the Helmholtz equation [18]:

$$\nabla^2 E + \epsilon(\omega) k_0^2 E = 0$$

Which can be solved by assuming the following solution:

$$E(r, \omega - \omega_0) = F(x, y) A(z, \omega - \omega_0) \exp(i\beta z)$$

Where the pulse envelope amplitude $A(z, \omega - \omega_0)$ is a slowly varying function of z in the frequency domain, β is the wave number and $F(x, y)$ is the spatial intensity distribution of the beam. To simplify the problem, here we consider only the situation of single mode fibers and assume the spatial distribution to be quasi-Gaussian with an affective area A_{eff}. By taking into account the dielectric properties of silica glass and by neglecting the fiber losses, the propagation of the slowly varying envelope of the electrical field can be described by the nonlinear Schrödinger equation (NLSE) [19]：

$$i\frac{\partial A}{\partial z} = \sum_{m\geq 2} \frac{i^{m+1}}{m!}\beta_m \frac{\partial^m A}{\partial t^m} - \gamma|A|^2 A \qquad \text{Eq 1.1}$$

For practical reasons, A is commonly normalized in a way that $|A|^2$ represents the optical power. The nonlinear parameter γ is then defined as:

$$\gamma = \frac{n_2\omega_0}{cA_{eff}}$$

where n_2 is the nonlinear index of silica.

This term corresponds to the contribution from Kerr non-linearity through self-phase modulation [20].

The sum in the right-hand side of equation (1.1) corresponds to the dispersion terms resulting from the Taylor-expansion of the mode-propagation constant β around the central wavelength ω_0 of the pulse spectrum:

$$\beta(\omega) = n(\omega)\frac{\omega}{c} = \beta_0 + \beta_1(\omega-\omega_0) + \frac{1}{2}\beta_2(\omega-\omega_0)^2 + \cdots$$

Where

$$\beta_m = \left(\frac{d^m\beta}{d\omega^m}\right)_{\omega=\omega_0}$$

Among whom β_1 is related to group velocity at which the envelope of an optical pulse travels, and β_2 represents the dispersion of group velocity and is thus responsible for pulse broadening. This phenomenon is termed “group velocity dispersion (GVD)”, and β_2 is the GVD parameter. One may also find it convenient in certain cases to define the GVD parameter as:

$$D = \frac{d\beta_1}{d\lambda} = -\frac{2\pi c}{\lambda^2}\beta_2$$

Higher order dispersion terms should be taken into account in certain cases. In the case of standard fibers with slow dispersion slope, the third-order dispersion (TOD) β_3 can be neglected except when the wavelength is around the zero-dispersion wavelength of the fiber where $\beta_2 \approx 0$, or when an ultra-short pulse is concerned [19]. The fibers considered in this work exhibit high second order dispersion in a limited wavelength as a results of mode coupling. This results in relatively important high-order dispersion terms that should be taken into account. If pulse with very broadband optical spectra or very special dispersion curves are dealt with, it could be necessary to consider up to the 4th or even 5th and 6th order dispersion. To the ultimate extreme, the concept of Taylor expansion could lose its value when too many orders should be considered.

It is worth noting that equation (1.1) corresponds to propagation inside a passive fiber. When generalizing the NLSE to propagation inside a doped-fiber, it should be taken into account the contribution from the amplification medium with a limited gain bandwidth and the effect of gain saturation. This situation will be discussed more deeply in Chapter 2.

1.2 Mode-locked fiber lasers

1.2.1 Mode-locking principles

A laser cavity of finite length L can support numerous longitudinal modes whose wavelength λ satisfies $n\lambda = L$, where n is an integer. As gain media have a limited gain bandwidth and non-uniform gain value for different wavelengths, the output of a CW laser normally has single or few wavelength components due to mode competition. Instability of the frequency or of the power distribution among the output frequencies are common problems and many techniques such as Pound–Drever–Hall laser frequency stabilization [21] are introduced to solve these problems.

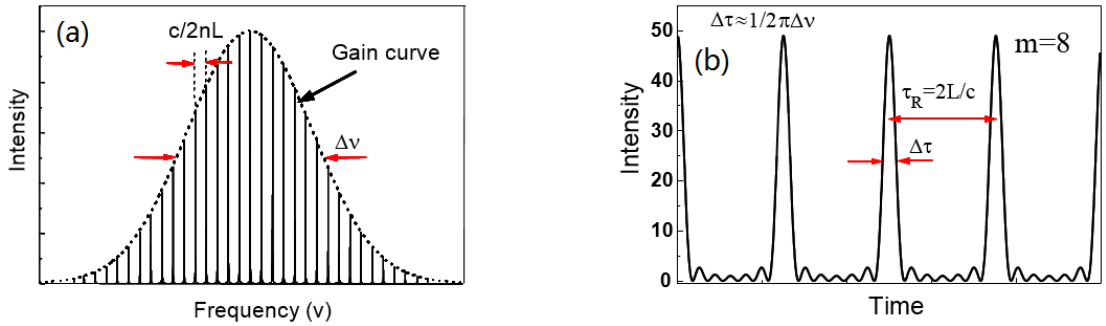

Figure 1-1 (a) overall spectrum of a mode-locking regime and spectra of its corresponding longitudinal modes. (b) temporal intensity profile obtained by mode-locking 8 longitudinal modes.

But to have a laser working in an ultra-short pulse regime is another story. From the Fourier transformation, it can be derived that a strongly-temporally-localized signal must have a finite distribution in frequency domain, so a spectrum with infinitesimal bandwidth such as that of a CW regime is not what one should expect from an ultra-short pulse regime. Figure 1-1(a) shows a typical spectrum of a mode-locking regime. The envelope is what is commonly observed from an optical spectrum analyzer (OSA). The discrete individual peaks in the spectrum each stands for a different longitudinal mode. The density of the modes is normally too high for the OSA to discern each of them.

Assuming there are M modes in the spectrum, the electric field can be written as:

$$E(t) = \sum_{n=1}^{M} E_n \exp(i(\varphi_n - \omega_n t))$$

where E_n, φ_n and ω_n represent the amplitude of the electric field, the initial phase and the frequency associated with the n-th mode respectively. If the phase differences between each pair longitudinal modes are random, the intensity of total electric field would be like that of a CW laser. But if the phase differences between each pair longitudinal modes are constants, the intensity of total electric field $I(t) = \langle |E|^2 \rangle$ can be expressed as:

$$I(t) = I_0 \frac{sin^2(M\pi\Delta\nu t + \varphi/2)}{sin^2(\pi\Delta\nu t + \varphi/2)}$$

Figure 1-1(b) shows the intensity profile in temporal domain for m=8. We note that the signal is in the form of a train of pulses with an interval of the traveling time for one round-trip in the cavity, with FWHM inversely proportional to the spectral bandwidth $\Delta\nu$.

1.2.2 Mode-locking mechanism

To make the laser work properly in a desired pulsing regime, specific mechanisms need to be introduced into the laser cavity. Figure 1-2 summarizes the mode-locking mechanisms commonly used. The method for active mode locking is based on the use of an intra-cavity modulator, which modulates the amplitude, or the phase of the optical field. Two kinds of modulators are commonly used: the acousto-optic modulators (AOM) and the electro-optic modulators (EOM). Although it could be an easy way to achieve mode-locking regimes by active mode locking, the pulse duration is dictated and limited by the efficiency of the modulator and is generally in the picosecond range.

So, in most cases where ultra-short pulse generation is required, passive mode-locking mechanisms are much preferred because they need no external source and can produce sub-picosecond pulses. The most common techniques for passive mode-locking are figure eight loop (8FL) [22], additive pulse mode-locking [23], saturable absorbers and nonlinear polarization evolution. In the following sections, two of the mechanisms which have been routinely used during my PhD thesis, namely saturable absorbers mirrors and NPE, will be detailed.

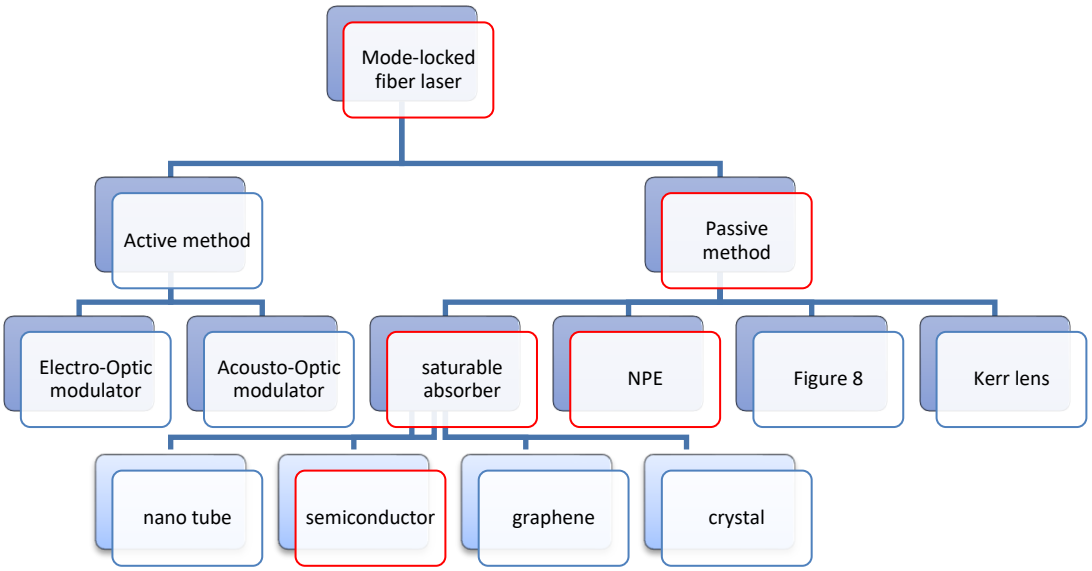

Figure 1-2 common mode-locking mechanisms

1.2.2.1 Saturable absorber and SESAM

A saturable absorber (SA) or a saturable absorber mirror (SAM) is a non-linear component whose transmittance or reflectivity is intensity-dependent: it allows light of higher intensity to pass or be reflected with lower losses for a given range of intensity.

This kind of components was first introduced in the early 1970s and served as the only method to obtain passive mode-locking until the advent of additive-pulse mode-locking [24]. Today saturable absorbers are widely used in many kinds of mode-locking lasers. Among them semiconductor saturable absorber mirrors (SESAM) have attracted intensive research and been put into different applications owing to their compactness, low-cost, polarization-insensitivity, ease of fabrication and viability in full simple and passive mode. The technology used to fabricate a SESAM allows very precise control of its parameters such as the working wavelength, the saturation energy and absorption recovery time. The absorption recovery time is a parameter used to define the time needed for the SESAM or other SA to return to its linear reflectivity after the disappearance of high fluence, and SESAMs with short absorption recovery time are necessary in ultra-short pulse generation. To reduce the recovery time, the growth is carried out at low temperature to facilitate the formation of defects which break the periodicity of the crystal lattice. These defects then introduce real electron traps in the band gap and thus bring the recombination time of the carriers down to the picosecond level, compared with the nanosecond level otherwise. Recovery time shortening can also be obtained by doping, heavily ions implantation or irradiation [25].

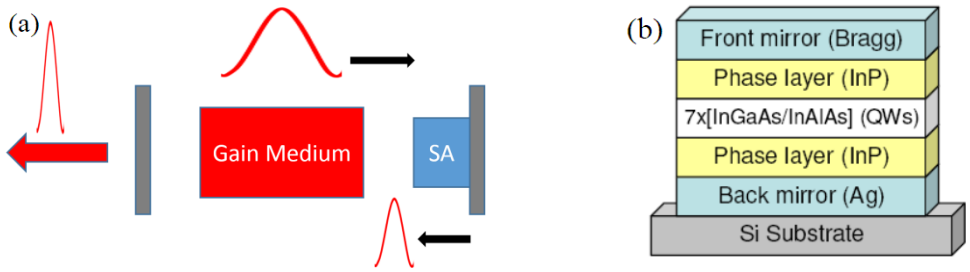

Figure 1-3 Schematic of a mode-locked cavity with saturable absorber (b) Structure of a saturable absorber semiconductor mirror (SESAM). QW: quantum well.

The typical structure of a SESAM is shown in Figure 1-3(b). It consists of a highly reflective back mirror with a reflectivity close to 100%, a front mirror, a saturable absorber material, phase layers, and a substrate. Between the two mirrors are the quantum wells (QWs) sandwiched by phase layers. Two kinds of SESAM are widely used: Resonant-SAM (R-SAM) and AntiResonant-SAM. For a Resonant-SAM, the thickness of the total absorber and phase layers are adjusted so that the micro Fabry-Perot cavity is operated at resonance. The nonlinear phenomenon of saturable absorption can be greatly enhanced by placing the saturable absorber layer at the antinode of the optical field in the vertical cavity. For an Antiresonant-SAM, the thickness of the total absorber and spacer layers are adjusted so that the micro Fabry-Perot cavity is operated at anti-resonance. Operation at anti-resonance makes the intensity on the absorber layer lower than the incident intensity, which increases the saturation energy of the saturable absorber and the damage threshold to the cost of a very small modulation depth. This type of SAM has a broad bandwidth and minimal group velocity dispersion. The top mirror reflectivity of the A-FPSA is an adjustable parameter that determines the pulse fluence entering the semiconductor saturable absorber.

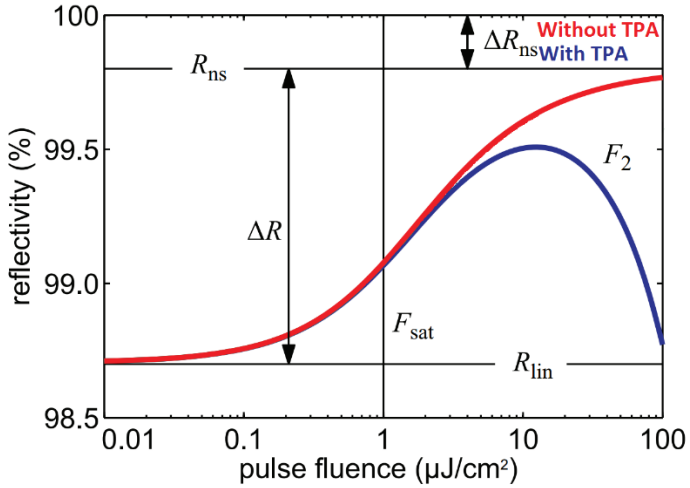

Figure 1-4 Typical reflectivity curve of a SESAM with respect to the pulse fluence. R_{lin}: linear reflectivity; R_{ns}: reflectivity with saturated absorption; Δ R:modulation depth; ΔR_{ns}: nonsaturable losses in reflectivity; F_{sat}: saturation fluence. The red curve shows the fit functions without Two Photon Absorption (TPA) ($Fp \rightarrow \infty$) while the blue curve includes TPA.

Figure 1-4 shows the typical reflectivity diagram of a SESAM. In a system with low light fluence, the reflectivity of the SESAM is R_{lin}. When the incident fluence exceeds a certain level F_{sat}, the reflectivity of the saturable absorber increases until it reaches the value of the saturated reflectivity R_{ns}. The difference in reflectivity between the absorbing state and the saturated state is called differential refectivity $\triangle R$ or modulation depth. It should be noticed that the curve is bell-shaped, which means the reflectivity will reduce if the fluence exceeds a certain value. This is caused by two-photon absorption and often referred to as overdriving. When overdriven, the SESAM may function abnormally and it may result in different artifacts among which multi-pulse regimes are often observed.

Figure 1-5 schematically explains the effect produced by a SA on the input pulse. Notice that a real SA will always introduce some loss and thus will always attenuate the pulse intensity.

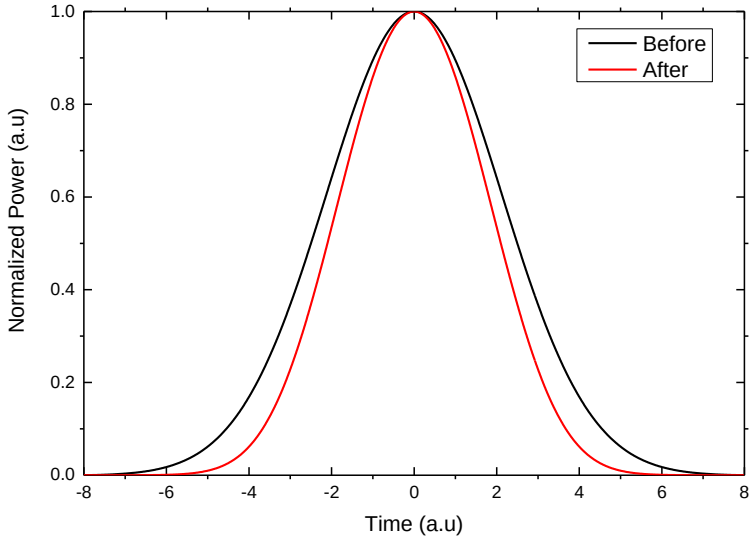

Figure 1-5 Change of pulse shape caused by a saturable absorber for a Gaussian input pulse (FiberDesk simulation). Pulse power is normalized respectively to show only the shortening effect.

In a laser cavity, the SA tailors the pulse's temporal shape by allowing the central peak to pass with few losses while absorbing strongly its low-intensity sides at every round trip. This way, the SA or SAM initiates and stabilizes the mode-locking state of the laser.

Now let's consider a simple laser system which only consists in a mirror, the gain media and a SAM as shown in Figure 1-3(a). The dynamic behavior and the pulse evolution at the beginning stage of the laser are shown in Figure 1-6. A stable pulse is established from quantum noise after about 30 round-trips and continues to shorten as it gradually broadens in the frequency domain until the gain bandwidth limitation is met.

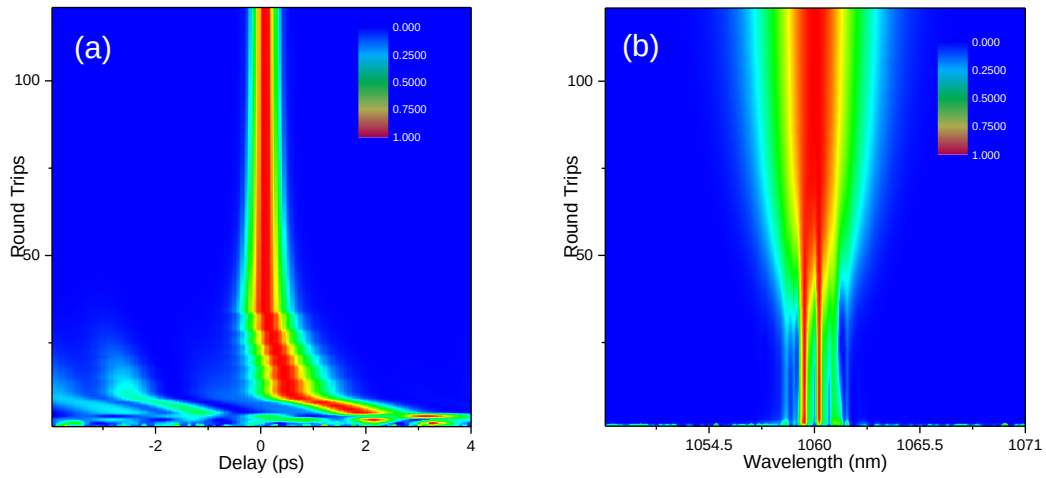

Figure 1-6 (a) simulated temporal evolution of pulse generated from quantum noise and (b) the corresponding spectrum evolution. The intensities are normalized at each round trip to show the evolution clearly.

The function how a SESAM establishes or/and stabilizes the mode-locking in lasers with different operation regimes may differ. For example, in a soliton laser, the SESAM serves only to absorb the optical noise and the so-called "continuum" to stabilize the mode-locking. However, in regimes where SESAM is used together with nonlinear polarization evolution (NPE) to achieve mode-locking, it could function in another manner which would be discussed in the next section.

A laser system mode-locked by SA is generally sustainable. Also, there is a good chance for such a system to be self-starting, which means the laser can get into the mode-locking state from quantum noises in a reasonable time without manual adjustment or other mechanism. But many SAMs, especially the semi-conductor SAMs (SESAMs) which are based on multi-quantum well resonance, are vulnerable to high peak power. In other words, they have low damage thresholds. For example, an adjustment of the cavity can disturb the stable working state of the laser and initiate the generation of energetic pulses that can damage permanently the SA. Although this kind of operation is rare in industry, it's quite common in researches. Also, this vulnerability sets a limit to the highest power a laser system can create.

It is important to select SESAMs with adapted parameters to improve or even establish mode-locking regimes in fiber lasers. For example, SESAMs with shorter absorption recovery time are preferred in cavity configurations where short-pulse generation is expected. In the experiments led during my thesis, SESAMs have been frequently changed to get an optimal mode-locking regime.

1.2.2.2 Nonlinear polarization evolution

From the discussion of the previous mode-locking mechanism, it can be concluded that a method to realize mode-locking is simply to use the nonlinearity of certain components to filter out the low intensity noise so that intensity accumulation is allowed only for some pulses. After the establishment of mode-locking, these components continue to contribute to stabilization of the mode-locking state. The nonlinear polarization evolution (NPE), or nonlinear polarization rotation (NPR), is a method working in a similar way, but that does not require specific nonlinear components as it takes advantage of the nonlinearity from the fiber itself.

The principle of how NPE can realize mode-locking is shown in Figure 1-7. SPM and XPM-induced nonlinear refractive index changes modify the polarization state of the pulse along its propagation in the fiber. As this nonlinear refractive index is intensity-dependent, there is a gradually increasing difference between the polarization states of the high-power peak and the low-power edges of the pulse along propagation. So, if polarization-sensitive components are inserted in the cavity (a polarization controller, wave-plates and a polarizer for example), those unwanted low intensity parts can then be filtered out, which is similar to the function of a saturable absorber.

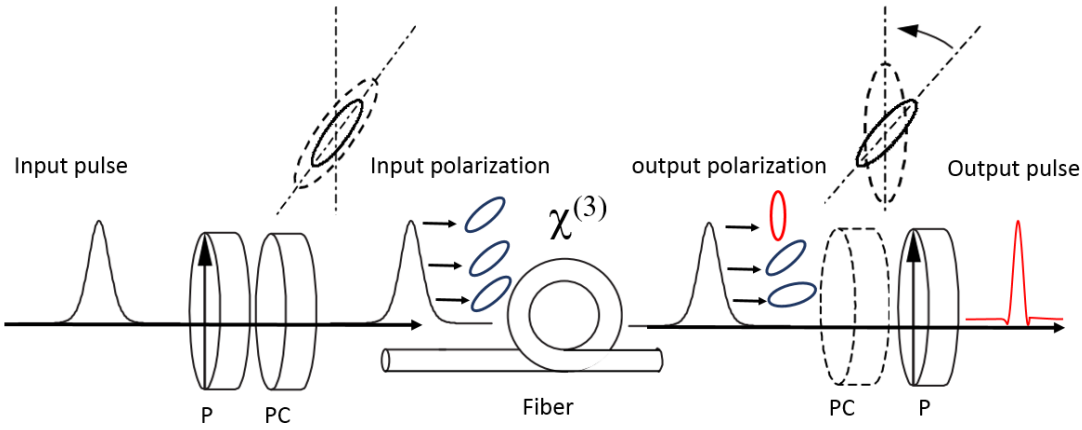

Figure 1-7 schematic explanation of how NPE works as a mode-locking mechanism.

Figure 1-8 is an example of a fiber laser mode-locked using NPE. Notice that not all the polarization sensitive components are dedicated to NPE, the waveplates before the polarization-sensitive beam splitter are to optimize the output signal. The NPE method for mode-locking does not rely on a fragile component such as a SESAM, so the system can be much more resistant to high energy and sporadic giant waves, and is generally used when high energy pulse generation is required from a fiber laser system. But still this method has several disadvantages: it demands high intensity to make the NPE effect significant enough to serve as a mode-locking mechanism, so it cannot be used if the system is incapable of delivering high energy pulses.

Moreover, the mode-locking state under NPE mechanism is normally achieved by a careful adjustment of the light polarization state, the tolerance to misalignments is then very low, and this fact makes it difficult to be operated and inconvenient to be used in industry. Polarization states of the light propagating inside the fiber can be affected by many other factors such as mechanical perturbation or temperature changes. A laser system involving NPE is thereby more vulnerable to environmental disturbances. To overcome some of these disadvantages, the NPE method is often used together with a SA: at the initial stage the SA plays the main role to establish the mode-locking state and as the pulses gain more and more energy after each round trip, NPE effect gradually takes over and finally, when the mode-locking is stable, NPE is the main mode-locking mechanism while the SA weakly contributes or even is transparent in the laser system.

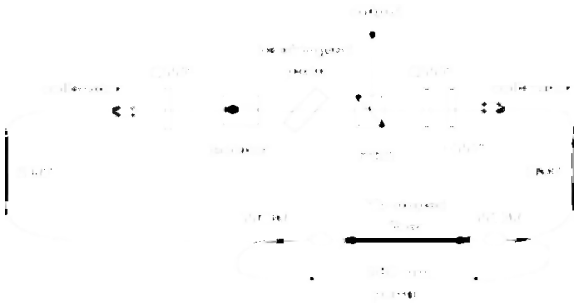

Figure 1-8 (Removed for copyright issues) ANDi laser mode-locked by NPE [16]

NPE has thereby been a frequently used mode-locking mechanism during my thesis, and has been found very effective when high energy operation regimes are needed. Although a SESAM is the main mode-locking mechanism used in the experiments presented in the next chapters, one may always find it accompanied by polarization components for NPE.

1.3 Mode-locked regimes in fiber lasers

As shown in the previous section, mode-locking is a process involving many mechanisms and effects, among which the interplay between dispersion and nonlinear effects plays the key role which governs the laser dynamics regime. Several distinct regimes with specific pulse characteristics have been investigated for years, and for some of them even decades. In this section, we summarize the main regimes along with their specific dynamics, as they will be extensively used in the experimental and numerical studies presented in following chapters.

1.3.1 Soliton regime

Soliton is the general terminology used to describe a certain set of the solutions to the NLSE

(Eq 1.1). The soliton regime features pulses that are either temporally or spatially localized. More generally, it includes Akhmediev breathers (ABs), Kuznetsov-Ma (KM) solitons, the Peregrine soliton (PS), and even the bi-periodic solutions of the NLSE described by Jacobi elliptic functions [26][27][28]. Some of the soliton solutions are related to optical rogue waves and drew the interest of many researchers [29]. But the soliton regimes we are interested in are the so-called fundamental solitons. The fundamental soliton regime is a result of the counterbalance between SPM and dispersion. The pulses in such a regime can be mathematically expressed as

$$A(t,z) = A_0 Sech\left(\frac{t}{t_0}\right)\exp\left(\frac{iz}{2}\right)$$

and have an invariant shape during their propagation. Solitons of higher order have different kinds of complicated periodically recurring evolution behaviors of their pulse shapes are thus not attractive to us.

As the chirp induced by SPM is positive definite for a Gaussian pulse, a prerequisite of a laser being running under the soliton regimes is the cavity to have an anomalous GVD. The first soliton observed in optical fiber was reported in 1980 [30], and four years later, the first fiber laser in soliton regime was developed and reported by the same group [31].

Although appealing to some applications because of its shape-conservation, the solitonic regime has a limitation in the highest energy it can reach. The pulse energy of solitons is governed by the area theorem

$$E_p\tau = 2\frac{|\beta_2|}{\gamma}$$

Where E_p, τ denote the pulse energy and duration respectively. As one can conclude from this formula, the pulse energy in the soliton regime is thus limited by the nature of the fiber material and the structure of the fiber. Commonly the pulse energy is around several nano-joules, prohibiting it from being used in applications involving energy scaling.

As this kind of lasers is easy to develop and their output pulses are well-characterized, they often serve as seed signal producer in research works.

To overcome the limitation of the soliton regime, cavities with different dispersion maps were studied and different mode-locking regimes were found. The pulses from these regimes are no longer invariant during the propagation, but their characteristics including shapes, spectra and chirp evolve within the cavity. A key point to realize such mode-locking regimes is to keep the so-called pulse self-consistency, which means the temporal and spectral profiles of the pulse should remain unchanged at any position inside the cavity after each round-trip. Different configurations to achieve mode-locking have different mechanism to keep the pulse self-consistency, which are briefly introduced in the following sections.

1.3.2 Dispersion-managed regimes

The term “dispersion managed” is used to describe a cavity consisting of media with both normal and anomalous dispersions, and the mode-locking regimes under these cavity configurations are called “dispersion managed regimes”. The normal and anomalous dispersions from different media may and may not counterbalance each other and thus result in the total GVD being anomalous, normal or zero. The dynamic and pulse characteristics can differ greatly depending on the value of total GVD. So, despite being classified under the same category, the situations deserve being discussed respectively according to the different kinds of cavity dispersion maps.

1.3.2.1 Stretched pulse regimes

These regimes are retrievable in the lasers whose total GVD is generally around zero. For a fiber laser, this is normally achieved by building the laser with two sections of fibers with opposite signs of chromatic dispersion. If one look into the pulse evolution when the mode-locking state is established under this configuration, one would find the pulse is temporally broadened in the normal dispersion part while narrowed in the anomalous dispersion part, a phenomenon referred to as “breathing” dynamics, which fulfills the pulse self-consistency in temporal domain. The pulses always have lower peak power which minimizes the nonlinear effect inside the cavity, so the chirp of the pulse is basically linear, if not Fourier-limited. The lowered peak power also results in a higher possible pulse energy compared with that of a soliton regime. It is also generally found that stretched-pulse lasers deliver pulses with broader spectral bandwidth. Another important attribute of this regime is that, although the temporal profile of the pulse is stretched and compressed during the roundtrips, the spectral shape of the pulse is conserved along the cavity, so the pulse self-consistency in spectral domain is always satisfied [15].

1.3.2.2 Self-similar regimes

The pulses from a self-similar regime are also called “similaritons”. Mathematically, the similaritons correspond to asymptotic solutions of the NLSE which conserved parabolic pulse shapes and spectrum during propagation and resists to the detrimental effect from optical wave-breaking.

The first demonstration of the dynamics of the similaritons was reported in 1993 [32] by Anderson et al. In their theoretical study, it is proved that parabolic pulses can propagate without

distortion in normal dispersion passive fibers. Further work also found that pulses with various profiles could converge to parabolic profiles after enough propagation length [33].

The cavity configuration required to generate similaritons is similar to that of a stretched-pulse laser, but with the difference that the total GVD is not completely counterbalanced and has some net normal dispersion uncompensated. In this case, the anomalous dispersion media are mainly used to compress the pulse to keep its temporal shape self-consistency. Similaritons are experimentally observed in many cavities whose dispersion are properly managed [34][35][36]. Unlike the stretched-pulse regime, the spectra of similaritons are not invariant during the intra-cavity propagation but keep broadening due to SPM. So, additional mechanisms such as gain-profile filtering or passive filters is necessary to ensure pulse self-consistency in the spectral domain. Additional dispersion compensating components is also needed to compensate for the accumulated chirp. In 2004, stable mode-locking in an all-normal dispersion fiber laser is obtained [37] and it is found that the pulse self-consistency is satisfied without any intra-cavity dispersion compensation element, and the idea of all normal dispersion lasers is then proposed. Before introducing all-normal dispersion regimes, it is worth mentioning the application of similaritons in fiber laser amplifiers. As we know that compared with Gaussian or hyper-secant shaped pulses of the same energy, the parabolic shape has a lower peak power and thus would suffer less from the nonlinearity, which is appealing for high energy applications. And previous work has already proved that any pulse shape gradually evolves into a parabolic intensity profile with a linear chirp [33]. Because in the NLSE with gain, assuming $A(z,T) = A'(z,T)\exp(i\varphi(z,T))$, we can get an asymptotic self-similar solution in the limit $z \to \infty$, provided that $g \neq 0$ and that $\gamma\beta_2 > 0$. The solution is:

$$A'(z,T) = A'_0 \exp\big(i\varphi(z,T)\big)\left(1 - \frac{T^2}{T_p^2(z)}\right)^{\frac{1}{2}} \qquad |T| < T_p(z)$$

Where $T_p(z)$ is effective pulse width which defined as for any T that satisfies $|T| > T_p(z)$, $A^{'}(z,T) = 0$. This corresponds to a wave packet with a parabolic envelope intensity profile, and a quadratic phase which can be represented by:

$$\varphi(z,T) = \varphi_0 + 3\gamma(2g)^{-1}A_0'^2(z) - g(6\beta_2)^{-1}T^2$$

where φ_0 is an arbitrary constant. The corresponding linear chirp is then given by $\delta\omega(T) = g(3\beta_2)^{-1}T$. In the asymptotic regime, this pulse propagates self-similarly, maintaining its parabolic shape subject to the exponential scaling of its amplitude $A_0^{'}(z) = \left|A^{'}(z,0)\right|$ and effective width parameter $T_0(z)$ by

$$A_0'(z) = \frac{1}{2}(gE_{in})^{\frac{1}{3}}\left(\frac{\gamma\beta_2}{2}\right)^{-\frac{1}{6}}\exp\left(\frac{gz}{3}\right)$$

$$T_p(z) = 3g^{-\frac{2}{3}}\left(\frac{\gamma\beta_2}{2}\right)^{\frac{1}{3}}E_{in}^{\frac{1}{3}}\exp\left(\frac{gz}{3}\right)$$

$$\Omega(z) = \left(\frac{\gamma g E_{in}}{2\beta_2^2}\right)^{\frac{1}{3}}\exp\left(\frac{gz}{3}\right)$$

where E_{in} is the energy of the input pulse to the amplifier. These formulas imply that it is only the energy of the initial pulse (and not its specific shape) which determines the amplitude, duration, and bandwidth of the parabolic pulse. This is the principle of the parabolic amplifier and it finds application in chirped pulse amplification (CPA). For such amplifier taking advantage of similariton propagation, it is obtained analytically [14] the relation between the maximum possible pulse energy and the fiber parameters which is presented as:

$$\mathrm{E}_{max} = 3\frac{\Delta\Omega_g^3\beta_2^2}{g\gamma}$$

From which one can conclude that the increase of the second order dispersion β_2 could greatly boost the maximum achievable pulse energy. So, my thesis is devoted to exploring the energy scaling potential of fiber laser cavities with high β_2, to the study of how to adjust other parameters to get a balance under which stable mode-locking could be generated in such cavities, and finally, to the comprehension of the dynamics of such regimes.

1.3.3 All normal dispersion (ANDi) regimes

A laser operating with only normal dispersion components is said to be in the all-normal dispersion regime. The pulse then keeps broadening in the temporal domain along the cavity because of the absence of dispersion compensation mechanism. It also keeps broadening in the spectral domain due to SPM. These phenomena could perturb the mode-locking regime if not properly balanced, because the pulse self-consistency could never be satisfied. However, stable mode-locking regimes are retrievable via two different methods which thereby result in two distinct operation regimes.

The first method is to minimize the accumulation of GVD and nonlinearities during round-trips. These minimizations could be achieved by reduced cavity length [38], or by operating the laser in a narrow spectral or/and longer pulse duration regime [39][40]. Although these operation regimes with limited performances can reduce the detrimental accumulation of nonlinearities, they are not very interesting because of their limited energy and the long pulse duration.

The second operation regime is called **dissipative soliton** (DS) regimes. The regime get its name from the fact that dissipative mechanisms are essential for stable mode-locking under this

regime. The mechanism can be a saturable absorber with high modulation depth which in this case, serves as both a temporal filter and a spectral filter due to the highly-chirped nature of the pulse; or an intracavity spectral filter which at the same time shapes the pulse in spectral domain. The gain filtering effect can also be the mechanism stabilizing mode-locking regimes [41].

In an ANDi fiber laser, the pulse is chirped when propagating inside the fibers, and thus its peak power is always lowered by this effect, endowing it a higher potential in energy scaling. This process is quite similar to that in the CPA, so this kind of lasers are also referred to as chirped pulse oscillators (CPOs). However, as the energy increases, the spectral filtering needs to be enhanced to maintain the pulse self-consistency.

In [16], femtosecond pulses of more than 20 nJ are generated in an Yb-doped fiber laser featuring step-index SMF, and many fiber lasers based on this architecture with high pulse energy have been reported. The combination of this laser concept with large mode area (LMA) Yb-doped fibers has yielded the generation of ultrashort pulses with pulse energy approaching the microjoule level [42] [43] [44] [45]. Femtosecond oscillators based on erbium-doped fibers and operating in the normal dispersion regime have also been reported with energy levels of several nanojoules [46] [47].

One may also generalize the concepts of CPO and dissipative solitons outside the frame of ANDi regimes. For example, in a dispersion managed cavity whose net GVD is highly-normal, the pulse evolution inside the fibers with normal dispersion can resemble that in the ANDi regimes. So, ultra-short regimes with high pulse energy may also be similarly achieved in dispersion managed lasers, as illustrated in Chapter 3.

1.3.4 Dissipative soliton resonance

Before moving to the next section dealing with high normal dispersion fibers, it is worth mentioning a particular operation regime of fiber lasers and called dissipative soliton resonance (DSR) regime. This regime was first predicted by a theoretical study in 2008 [48] based on a solution of the complex cubic-quintic Ginzburg–Landau equation. It is stated that in this regime, the pulse energy of the super-Gaussian like predicted solutions can increase indefinitely for a specific set of normalized parameters. Square pulses generation are then experimentally demonstrated in both anomalous dispersion regime [49] and normal dispersion regime [50][51]. Although these square pulses could extend very long in temporal domain (up to hundreds of nanoseconds), the coherence is well-kept within its square profile packet, a characteristic which is different from those from noise-like regime [52]. A recent study also reported harmonic DSR generation [53].

The powerful energy scaling ability of DSR regime may find its application to biomedical imaging, molecular finger printing fabrication nanostructures in transparent dielectrics etc. It is

however difficult so far to get ultra-short pulses at the same time. Compression with linear components would cause a sophisticated evolution of the pulse which is very different from those of the pulses generated in the regimes introduced above, and result in a pulse shape far from satisfying [54].

1.4 High normal dispersion fibers

In this section, we present the different fiber structures studied during this thesis to build high normal dispersion fiber lasers. The first fiber type features a W-type index profile which have been largely explored last decade for dispersion compensation in optical telecommunication. The second category concerns bandgap fibers that have attracted much interest because of its mode area scaling, but what we exploit for here are their specific dispersion properties.

1.4.1 W-type fiber

Figure 1-9 shows schematically the typical "W-shaped" refractive index profile of a W-fiber. It is the same as that of a step-index fiber if one ignores the ring part (the part from radius b-c in Figure 1-9).

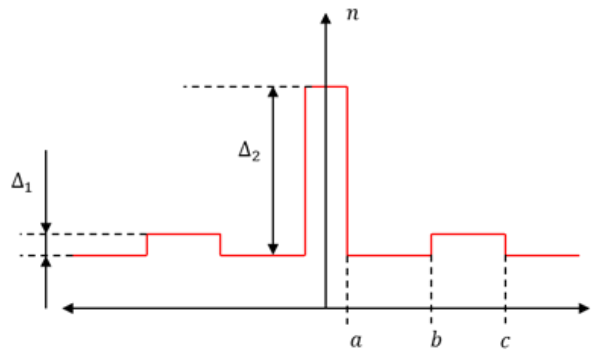

Figure 1-9 typical refractive index profile of the W-fiber

This design is widely used in fiber-based dispersion compensation. The dispersion shift principle can be intuitively understood by the supermode approach [55]. The fiber structure can be decomposed into two parts: the step-index fiber part with the ring part removed, and the ring fiber with the core removed. The effective index of the combined modes can be described as [55]:

$$n_e = \frac{n_{e(core)} + n_{e(ring)}}{2} \pm \sqrt{\kappa^2 + \left(\frac{(n_{e(core)} - n_{e(ring)})^2}{4}\right)} \qquad \text{Eq 1.2}$$

Where $n_{e(core)}$ is the effective index of the core mode under solely step-index structure, and $n_{e(ring)}$ is that of the ring mode under solely ring-index structure. the parameter κ is the

coupling coefficient between the core mode and the ring mode of the specific W-type fiber [56]. Figure 1-10 shows the effective index of the core mode and the ring mode, together with those of the LP_{01} and LP_{02} modes from mode coupling under different coupling conditions. Both LP_{01} and LP_{02} components of the compound mode have abrupt changes in their effective indices because of the crossover of the two fundamental modes of the structure. As the chromatic dispersion of a certain mode is the second derivative of its effective index, those abrupt changes would result in high chromatic dispersion of the compound mode in a certain window of wavelengths (see Figure 1-10(b)), which is referred to as the resonance window in the following sections.

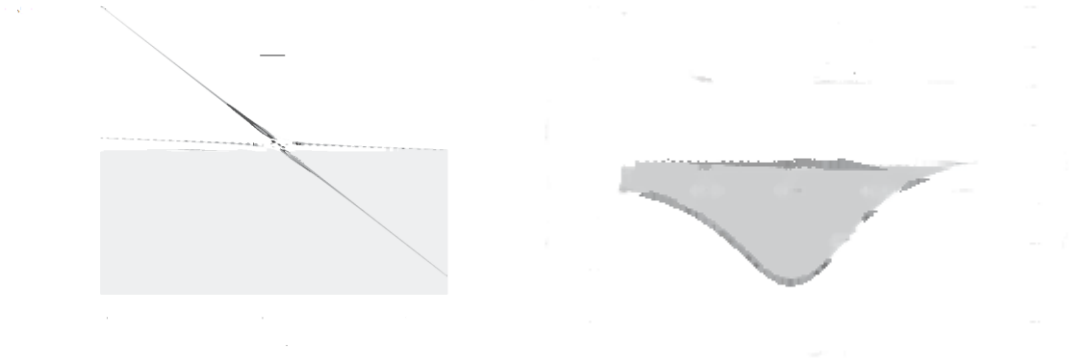

Figure 1-10 (Removed for copyright issues) (a) Effective index difference for LP_{01} and LP_{02} modes, showing the mode-coupling effect, and (b) The effective index difference of the ring, core and LP_{01} mode along with the resulting dispersion. [55]

One may also conclude from Eq 1.2 and Figure 1-10 that the bandwidth of resonance window and the magnitude of dispersion are closely related to the coupling strength. Under strong coupling, the indices curves of the compound modes change gently in a rather larger wavelength range, resulting in a broader resonance window but a lower dispersion, while under weak coupling, the indices curves would change sharply in a narrower spectral window and thus cause a higher dispersion.

1.4.2 Photonic bandgap Bragg fiber

The terminology “Bragg fiber” is used to refer to a category of fibers whose low-index cores are surrounded by claddings of alternating high and low indices. Figure 1-11 shows a diagram of the section of a Bragg fiber and its corresponding index distribution along the radius. From the diagram, light is expected to be confined and propagated inside the low-index core, which is in contrary to the situation of the common step-index fibers. To realize beam confinement in such geometric structure, cladding layers must be designed to satisfy the quarter-wave stack condition which makes the light in the vicinity of certain wavelength be strongly reflected

because of multi-layer interference and thus confined inside the core region.

The modal behavior of this kind of fiber was first theoretically analyzed and explain by P Yeh et al [57]. In their work, matrix methods were used to derive the mathematical description of the electro-magnetic distribution of the possible modes, and it was predicted that by properly designing the fiber structure, the attenuation of certain mode can be minimized while the undesired modes can suffer from high losses.

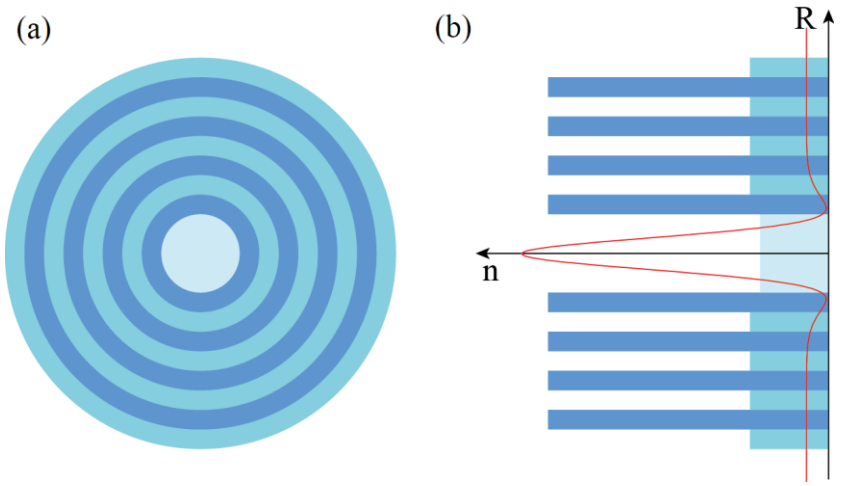

Figure 1-11 (a) the intersection of the Bragg fiber and (b) its corresponding index distributions. Red solid line: schematic intensity profile of the fundamental mode.

As we are looking for fibers with high normal dispersion, besides the fact that the Bragg fiber can be designed to propagate only fundamental a mode in its core part, we are more interested by whether or not it can exhibit a dispersion similar to that of the W-fiber introduced previously, as the high index ring part can also support ring modes. It turns out that similar result can be retrieved by the same supermode approach [55] with little difference. A previous study on a specific Bragg fiber was reported in [58], of which some characteristics are shown n Figure 1-12.

Figure 1-12 (Removed for copyright issues) From [58] (a) Actual refractive index profile of the passive Bragg fiber and the electric field distribution of two associated modes. (b) variation of normalized propagation constant with respect to the normalized frequency for even modes (open circles) and odd modes (solid lines) of the annular waveguide shown in the inset (composed of only the first step-

index ring core).

From Figure 1-12(b) one can conclude that the Bragg fiber is highly multi-mode in the annular waveguide part, so mode-coupling may occur between the fundamental core mode and different ring modes in different wavelength windows. In this study, the wavelength window concerned is around 1470 nm, and the simulation reveals that in the vicinity of 1470 nm, the dispersion up to $\pm 20000\ \mathrm{ps/(nm \cdot km)}$ can be produced due to the mode-coupling between the core mode and the LP_{81} ring mode. The simulated curves are shown below in Figure 1-13.

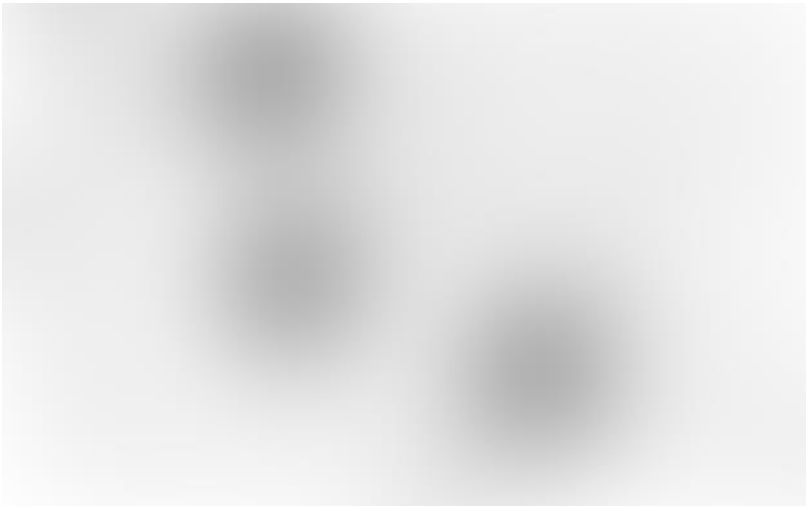

Figure 1-13 (Removed for copyright issues) (From [58]) Effective index versus the wavelength for the two modes related to coupling. Beam profiles show the evolution of the intensity distribution between the core mode and the ring mode. The refractive index of pure silica is plotted by gray line. Inset: computed chromatic dispersion.

From the simulation, one can see an intensity distribution shift from the core mode to the ring mode as the wavelength shifts to the blue side of the spectrum. At the resonance wavelength about 1470 nm, the two modes coexist and the dispersion sharply resonates between $\pm 20000\ \mathrm{ps/(nm \cdot km)}$.

Figure 1-14 (Removed for copyright issues) (From [58]) Evolution of the attenuation and the chromatic dispersion versus the wavelength for L=130m and curvature of 10 cm (bandgap fiber connected to two single-mode fibers). Also reported are the observed near-field intensity patterns at λ=1471 nm and λ=1550 nm. Inset: whole spectrum exhibiting four couplings.

Figure 1-14 shows the experimental results of dispersion characteristics of the designed Bragg fiber. The beam from a tunable laser was injected carefully into the core of the 130-meter-long fiber. The dispersion and attenuation of the input light is measured as the wavelength changes. The actual phase matching wavelength is 1470 nm as predicted by the simulation. And the beam profile, which is a combination of central Gaussian-like beam and a LP_{81} ring mode, is also in good agreement with the simulation. The peak values of the dispersion are $900\ \mathrm{ps/(nm \cdot km)}$ and $-1480\ \mathrm{ps/(nm \cdot km)}$ which, however, are lower than the predicted values by one order of magnitude. Furthermore, it's not in a small window of wavelength does the dispersion change rapidly but in a rather larger window of about 34 nm. These deviations can be explained by the defect of the uniformity of the Bragg fiber. A slight variation of the outer diameter of the fiber is inevitable during the drawing process when the fiber is produced. This deviation results in the fluctuation of the radii of the fiber along its length, which makes the phase-matching wavelength at one position of the fiber different from that at another. The results shown in Figure 1-14 is the spectral overlap of numerous resonance. The overall effect of this overlap is that the dispersion peaks are lowered and the spectral bandwidth is broadened. This analysis was validated by experiments in which the fiber length was shortened. With a fiber length of 24 m instead of 130 m, the dispersion value was doubled and the bandwidth was reduced to 24 nm. When the fiber length was further decreased to 1 m, the bandwidth was reduced to about 7 nm.

1.4.3 Ytterbium-doped Bragg fiber

Xlim Laboratory has already explored the power scaling potential of fiber lasers based on Yb-

doped Bragg fiber in CW; and in collaboration with our group (CORIA), the dynamics of a laser based on such fiber are studied under mode-locking regimes, which are reported in [59] and [60] respectively. But in these works, we mainly take advantage from the fiber's LMA nature. The index profile of the fiber studied in this work is depicted in Figure 1-15(a). This fiber consists of an Yb-doped core of 20 µm diameter surrounded by a periodic cladding composed of alternating low-n and high-n layers. The three high-n layers are GeO_2-doped. Adjusting lattice constant Λ, thickness d, and index contrast Δn of high-n layers, confinement losses of fundamental mode is made low (>1 dB/m) whereas high-order-modes' losses are made higher than 10 dB/m. Effective area of the fundamental mode is close to 200 μm^2. The Bragg preform was drawn into a fiber with an outer diameter of 120 µm. To form the double-clad structure, the fiber was coated with a low refractive index polymer, the NA of the pump inner cladding being 0.3. As indicated above, the main feature of Bragg fibers is that mode coupling between the fundamental core mode and some odd ring modes could lead to ultra-large chromatic dispersion. In these experiments, we intend to exploit this effect in mode-locked oscillators. Due to the difficulty to measure the dispersion of an active fiber, the dispersion measurement on a passive fiber with very similar structure to the doped fiber was conducted showing that the resonance-dispersion wavelength lies within the gain of Yb-ions as depicted in Figure 1-15(b). As we will see in Chapter 4, the high-dispersion region is shifted to shorter wavelengths in the Yb-doped Bragg fiber. We note that the high-normal dispersion region presents a narrow width of about 3 nm full-width at half-maximum (FWHM).

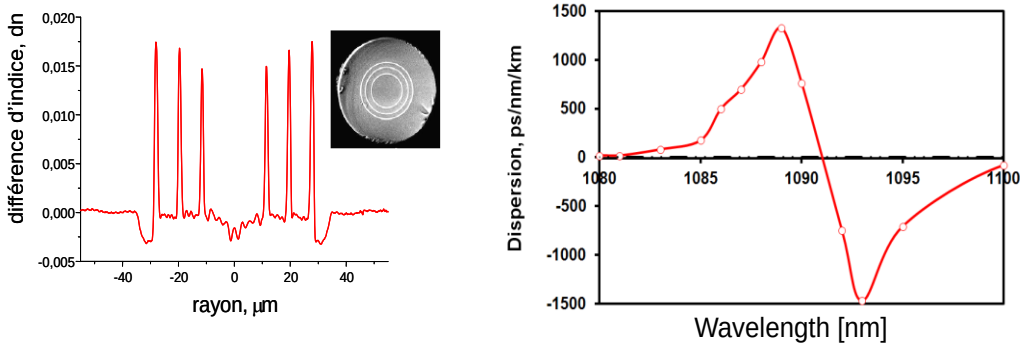

(a) (b)

Figure 1-15 Index profile and SEM image of (a) the Yb-doped Bragg fiber end and (b) dispersion evolution around the resonance wavelength measured on another passive fiber sample.

Now to compare these two kinds of fibers, they both are capable of producing ultra-high dispersion in a certain window of wavelengths from mode-coupling. The W-fiber belongs with step-index fibers and light is confined in a traditional way, while the Bragg fiber confines light through quarter wave stack reflection. The wavelength range for high dispersion in W-fibers

tends to be broader and the maximum dispersion tends to be lower, while the Bragg fiber tends to exhibit a rapid change of dispersion in smaller wavelength window with higher maximum dispersion. And last but not least, W-fiber usually has a small core diameter, while Bragg fiber can be designed to be large mode area (LMA) fiber.

There are however some common drawbacks for both kinds of fibers. First there will always be compromising trade-off to find between the range of wavelengths for high dispersion and the highest dispersion achievable. Second, an abrupt change of dispersion with respect to the wavelength means the higher order dispersion effects may not be negligible and detrimental effects from them should be expected in high energy applications.

1.5 Conclusion

In this chapter, we summarized the principles and fundamentals of pulse propagation in fiber optics, and introduced some techniques for the mode-locking of fiber lasers, which all together set the base for the work during my thesis.

The NLSE is the mathematical foundation based on which computational simulation are made possible with methods such as split-step algorithms. Details of simulations will be introduced and discussed in Chapter 2 together with the results of some simulations which guides and validates our experimental works.

To comprehend the physical idea of different linear and nonlinear effects existing in fibers and their influences on the pulse evolution is important to establish qualitative models, and thus necessary for fiber laser design and improvement. In Chapter 3 we will present a dissipative soliton laser conceived and studied during my thesis, and see how the above-mentioned nonlinear and dispersive effects are balanced to achieve high-energy short pulse regimes.

We have also seen that, using specific fiber designs such as W-fibers and Bragg fibers, we are able to get access to active fibers with high dispersions. Chapter 4 will then focus on the experimental results obtained with a mode-locked laser based on such fibers, which are very promising and pave the way for further exploitation.

Chapter 2. High normal dispersion fiber lasers: numerical simulations

In this chapter, we discuss the physics of mode-locked fiber lasers operating in high-normal dispersion regimes. We will start by the presentation of the different laser configurations treated and the corresponding models. The first part will deal with the case where dispersion management is realized by a passive dispersion compensation fiber. Pulse stabilization using high contrast amplitude modulation with or without spectral filtering will be discussed. The second part will discuss the case of mode-locked fiber laser based on specialty active fibers exhibiting high normal dispersion fiber. The pulse dynamics and laser performances reached in this laser platform are studied and compared to those achieved using a large mode area fiber with moderate dispersion. The impact of high-order dispersion terms is also discussed.

2.1 The numerical laser model

The calculation tool used in this work is based on the numerical resolution of the modified nonlinear Schrödinger equation (NLSE) using a split-step Fourier code. This tool has been developed by Thomas Schreiber from the Fraunhöfer Institute (IOF) of Jena [61] and is commercially available under the name Fiberdesk. As explained in the previous chapters, the pulse envelope evolution with respect to its propagation along an optical fiber is governed by the non-linear Schrödinger equation which includes the effects of dispersion, Kerr nonlinearity and saturated gain with a finite bandwidth:

$$\frac{\partial A}{\partial z} = g(\mathrm{E})A + \frac{ig}{\Delta\Omega_g^2}\frac{\partial^2 A}{\partial t^2} + \sum\nolimits_{m\geq 2} \frac{i^{m+1}}{m!}\beta_m \frac{\partial^m A}{\partial t^m} + i\gamma|A|^2 A$$

Where β_m is the m-th order dispersion coefficient. The effect of gain saturation is indicated by g which stands for the saturated gain who is related to low signal gain g_0 by:

$$g(E) = g_0 / \left(1 + \frac{E}{E_{sat}}\right)$$

Where E_{sat} is the saturation energy transferable from the pump. The $ig/\Delta\Omega$ term denotes spectral filtering due to the limited gain bandwidth.

To describe the effect of the saturable absorber (SA), we use the well-known transmission equation in the instantaneous response approximation:

$$T = 1 - \Delta R \left(1 + \frac{|A(t)|^2}{P_{sat}} \right)^{-1}$$

where ΔR corresponds to the saturable loss coefficient (modulation depth) and P_{sat} the saturation power. For all calculations, the saturation power of the SA is adjusted in order to maintain the saturation parameter (ratio between the instantaneous power and the saturation power of the SA) between 5 and 10. In the following section, we first investigate an erbium doped fiber laser based on a passive dispersion compensation fibre.

2.2 Dispersion-managed dissipative soliton erbium-doped fiber laser

The numerical model of the laser studied in this section is depicted in Figure 2-1. It consists in a linear cavity including an erbium-doped fiber (EDF) with normal dispersion, a passive fiber (SMF) and a dispersion compensating fiber (DCF). A fiber output coupler (OC) with 90% output coupling is considered in these simulations. The cavity contains a saturable absorber mirror (SAM) at one end and narrow band spectral filter (SF) at the other end. Pulse initialization and stabilization is ensured by the combined actions of these two important components. For reasons of clarity, we preferred to show the unfolded version of the cavity where the forward and backward paths are separated. The parameters of the different fiber segments are given in **Table 2.1**. The passive fiber included in these simulations correspond to the wavelength division multiplexer (WDM) and fiber output coupler needed to inject the pump power into the gain fiber and to extract the laser signal from the cavity, respectively. The DCF constitutes the main component allowing to adjust the total cavity dispersion to high values.

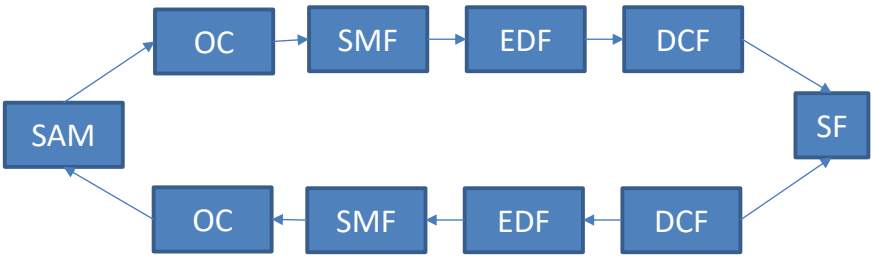

Figure 2-1 Schematic representation of the unfolded laser.

Table 2.1 Fiber parameters used in the simulation.

Parameter	units	Er-fiber	SMF	DCF
Length	m	1.2	0.6	variable
Mode field diameter	μm	4.9	10	6
GVD (β_2@1550 nm)	ps^2/m	+0.06	-0.023	+0.116
Effective area (A_{eff})	μm^2	18.8	78.5	28.26
Nonlinear coefficient (γ)	$W^{-1}\ m^{-1}$	$6.4\ 10^{-3}$	$1.5\ 10^{-3}$	$4.2\ 10^{-3}$
Peak small signal gain (g_0)	m^{-1}	4.6	0	0
Gain bandwidth ($\Delta\lambda_g$)	nm	10	-	-

The simulations are conducted using a high-modulation depth effective saturable absorber with 90 % modulation depth. Such high contrast could not be achieved using only a real saturable absorber but it can be reached by combination with an effective saturable absorber such as mechanism of nonlinear polarization evolution. The output coupler is fixed to a high value of 97% (3.5 m^{-1} in software setting) to account for the eventual additional losses due to light coupling between the fiber section and the SAM. The numerical resolution starts from noise or from a given pulse profile and calculation stops when the initial pulse or noise converges toward a stable solution after a certain number of round trips. For the whole study reported hereafter, the convergence criterion is defined such that the relative variation of the electric field intensity from one round trip to the next is less than 10^{-6} on at least 100 consecutive roundtrips. Once this criterion is satisfied, the parameters of the solution are calculated over a cavity round trip. For each parameter setting, we check for the limits of stability of the single pulse regime. This limit is reached when the system fails to converge towards a stable solution over more than 1000 roundtrips or when the system destabilizes into a multi-pulse regime.

The operation of such fiber lasers at moderate normal dispersion values, lower than +0.15 ps^2, has been already investigated in the work of H. Wang [62] and A. Cabasse [63]. It has been demonstrated that the use of high-contrast saturable absorber mirrors is enough for pulse initiation and stabilization in such laser cavities. Here, we investigate on a mode-locked laser featuring high normal dispersion with more than +1 ps^2 averaged value. In this case, pulse stabilization needs for strong pulse shaping mechanisms in the time and spectral domains. This is provided by the combined actions of a highly contrasted saturable absorber and a spectral filter. The results obtained using 10 m length of DCF which corresponds to a total cavity dispersion of 1.2 ps^2 are discussed in the following section.

2.3 High normal dispersion erbium-doped fiber laser with amplitude modulation

First, we simulate the laser operation without passive spectral filtering. Our findings show that pulsed solutions with long durations and relatively narrow spectral widths could be reached at low pump levels. To check the strength of the predicted solutions and study the starting dynamics of the laser, several initial conditions have been used and the transition to their stationary regime is analysed. The results obtained for a gain saturation energy of 2 nJ when starting from quantum noise or a Gaussian pulse are depicted in Figure 2-2. This figure shows the evolution of the temporal and spectral intensity distributions over several cavity roundtrips. Simulations show that for a fixed set of laser parameters, there is only one accessible attractor corresponding to a fixed solution. Its temporal and spectral full width at half maximum (FWHM) are 50 ps and 2.36 nm, respectively. It is important to note that this solution remains stable for several thousands of roundtrips indicating a stable attractor. All simulations have been checked to converge to the same attractor when repeated with higher temporal or spectral resolutions.

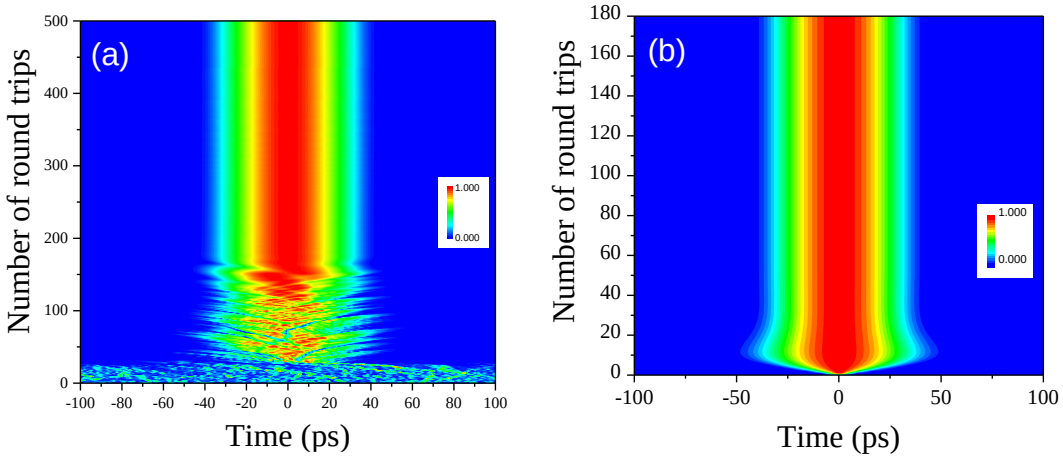

Figure 2-2 Stabilization of the pulsed regime for Esat = 2nJ when (a) starting from a quantum noise or (b) from a Gaussian short pulse.

The spectral and temporal shapes of the corresponding solution are shown in Figure 2-3. The output pulses exhibit parabolic temporal and spectral shapes indicating that this laser configuration is propitious for self-similar pulse propagation. This instantaneous frequency evolves linearly along the pulse indicating that the predicted solutions are almost linearly chirped, as expected for self-similar pulse propagation. Using a second-order dispersion delay line, the calculated pulses could be dechirped to ~2.58 ps duration which is very close to the theoretical limit calculated by Fourier transformation of the optical spectrum assuming a zero-phase relation (see Figure 2-3(b)).

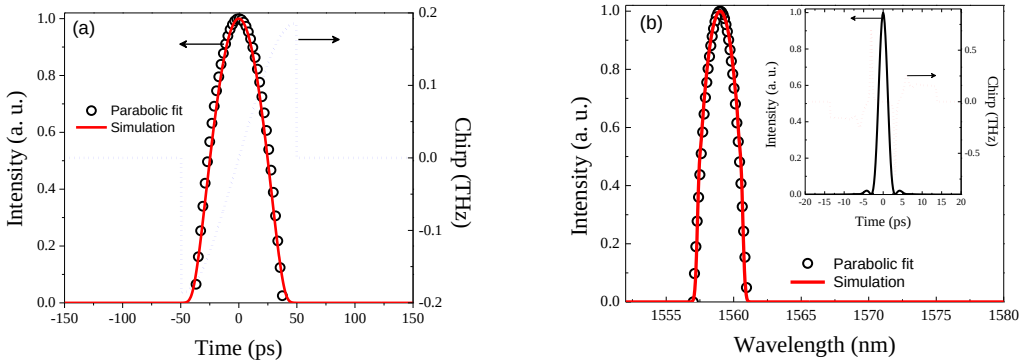

Figure 2-3 Results of simulations calculated at the end of the SMF just before the output coupler for Esat= 2 nJ: (a) temporal pulse shape; (b) spectral intensity distribution and dechirped pulse profile. The dashed curves correspond to the instantaneous frequency

By increasing the saturation energy, the energy and spectral bandwidth of the predicted solutions increase monotonically, see Figure 2-4. For low pump levels, pulse duration increases monotonically to reach a maximum value of 124 ps for a pulse energy of 100 nJ. For higher energy levels, the duration of the predicted solutions decreases when increasing the pump parameter. As discussed below, this marks a transition to fixed solutions featuring large spectral widths which are highly affected by the gain dispersion. The predicted solutions could be dechirped down to 1 ps width, see Figure 2-4(b). These results show that pulse energies higher than 190 nJ could be reached in this laser configuration but their experimental initiation seems compromised. Indeed, when starting from noise the pulsed solution cannot be reached for intra-cavity pulse energies higher than 20 nJ. The results localised in the gray regions of Figure 2-4 have been obtained using a low energy Gaussian pulse as an initial condition.

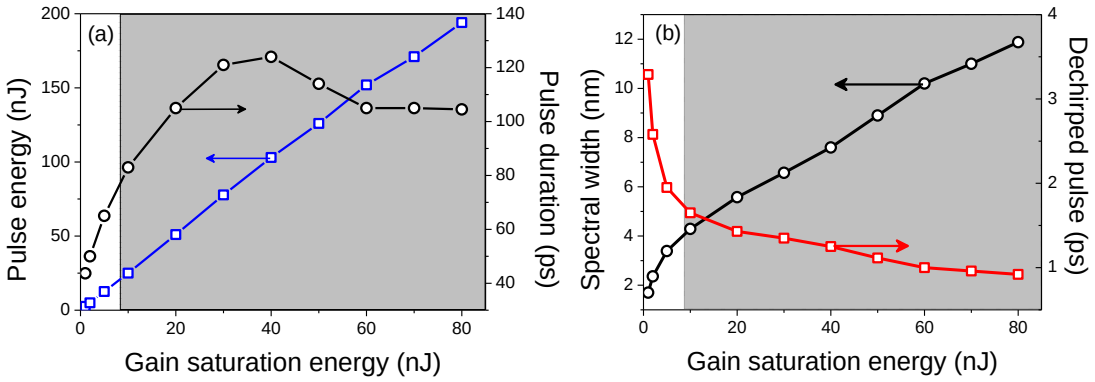

Figure 2-4 Evolution of laser performances versus pump power: (a) pulsed solution energy and temporal width; (b) spectral width and dechirped pulse width. Gray region: results achieved with initial Gaussian pulse.

For low pump levels, pulse evolution along the cavity shows that pulse stabilization is governed by the amplitude modulation provided by the SAM, see Figure 2-5(a). The high-stretching ratio

undergone by the pulse when propagating along the DCF is compensated by the amplitude discrimination induced by the saturable absorber which cuts the low power pulse wings. As this amplitude modulation is applied to strongly stretched pulses, it is converted to spectral filtering effect thus ensuring pulse self-consistency in the spectral and time domains. This situation changes at high pump levels where gain dispersion provides a significant contribution to intra-cavity pulse shaping as shown in Figure 2-5(b). We note that the asymptotic evolution of pulse duration and spectral width along the DCF is verified in both situations.

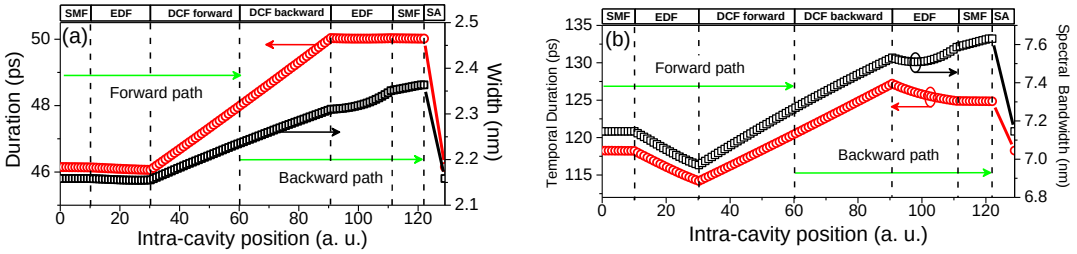

Figure 2-5 Intra-cavity pulse dynamics for a gain saturation levels of (a) 2nJ and (b) 60 nJ.

To investigate pulse shaping in more detail, the kurtosis parameter "κ" has been used to analyze the pulse temporal and spectral shapes [35][61]. The kurtosis is related to the presence of long tails (or "peakedness") and is defined as $\kappa = \mu_4/\sigma^4 - 3$ where μ_4 is the fourth centered moment and σ^4 the square of the variance. For instance, κ =-0.86 for a parabolic pulse shape and κ =0 for a Gaussian shape. For low pump levels, our analysis of the pulse characteristics using the kurtosis parameter then shows that the pulse spectral shape is parabolic all along the cavity with a kurtosis parameter close to -0.86 (Figure 2-6(a)). The temporal kurtosis evolves in the interval between -0.7 and -0.68 along the cavity indicating a very little change in the pulse shape which also approaches a parabola. By increasing the pump power, we observe a very small deviation from the parabolic shape probably due to the strong contribution from gain filtering (Figure 2-6(b)). The resulted fixed solutions exhibit a parabolic top spectrum with steep edges which are typical for high normal dispersion fiber lasers [15].

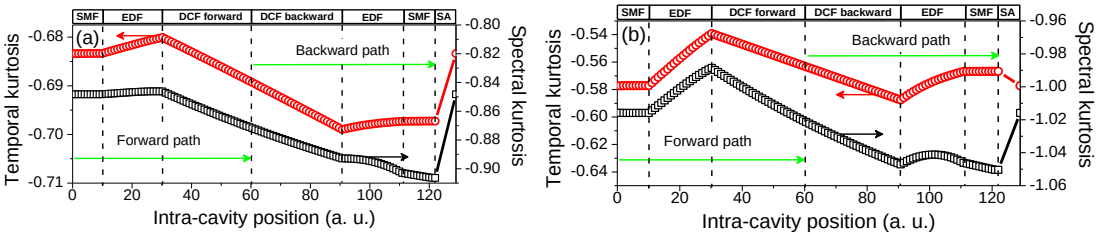

Figure 2-6 Pulse shape evolution along the cavity at (a) low pump level of Esat = 2 nJ and (b) high pump level of Esat = 60 nJ (b).

These numerical simulations confirm that using a long segment of dispersion compensating fiber to increase the normal dispersion of a mode-locked laser is interesting for high-energy parabolic pulse generation. However, the initiation of these regime seems difficult to achieve

as the solutions are not accessible from noise. One solution to enhance the intra-cavity pulse shaping mechanism consist to use a passive spectral filter in combination with the amplitude modulator. Next sections discuss precisely the numerical results obtained with intra-cavity spectral filtering.

2.4 High normal dispersion erbium-doped fiber laser with passive spectral filtering

Let us first discuss the numerical results obtained for a 10 m DCF along with a 4.5 nm bandwidth spectral filter. For gain saturation energies lower than 8 nJ, only single pulse solutions are obtained whatever are the initial conditions indicating that the system admits a fixed solution. This correspond to intra-cavity pulse energies lower than 11 nJ. However, for higher energy levels the system converges to multiple pulse solutions when being started from noise. Two examples of steady state solutions achieved from noise are shown in Figure 2-7(a) and Figure 2-7(b). While a single pulse solution with 10.7 ps duration is achieved at a pump energy of E_{sat} = 8 nJ, the situation is different at E_{sat} = 10 nJ where a bound state of two pulses is achieved. Fortunately, calculations show that when starting from a short pulse the system converges to a single pulse solution revealing the coexistence of several stable attractors at high energy levels (see Figure 2-7(c)). As we will see in the next chapter, the exploitation of a reconfigurable saturable absorber such as nonlinear polarization evolution is crucial to access high energy single pulse solutions in such laser configurations.

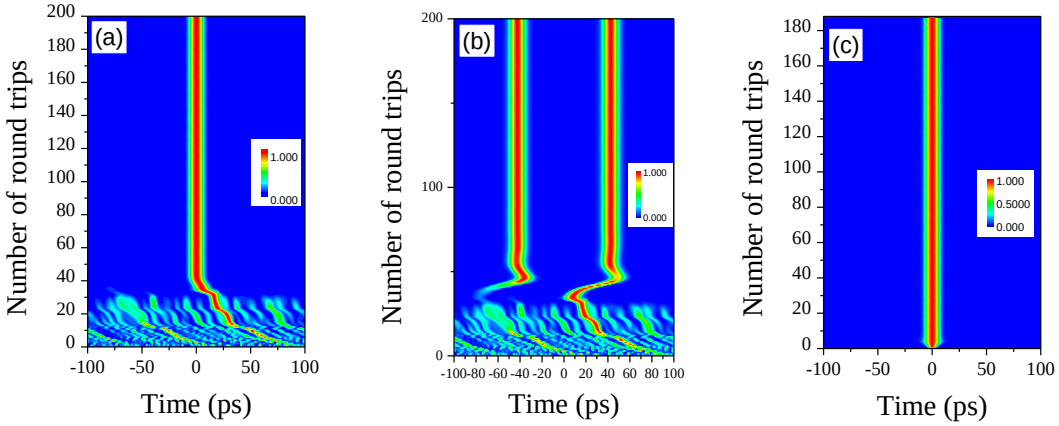

Figure 2-7 Stabilization of the pulsed regime when starting from quantum noise for gain saturation energies of (a) 8 nJ and (b) 10 nJ. (c) Stabilization from a short Gaussian pulse for Esat=10 nJ.

The evolution of the fixed solution characteristics versus pump power when starting from a Gaussian pulse are summarized in Figure 2-8. The gray region of this figure corresponds to the

multi-stable region where single pulse solutions coexist with multiple pulse solutions. As expected, pulse energy increases with pump power to reach 70 nJ at Esat=160 nJ. For higher pump levels, only multiple pulse solutions are predicted. We note that the pulsed solution is relatively long in duration at low energy levels because the spectral filter has less effect for narrow spectra. By increasing the pump power, pulse width decreases and stabilises around 12.4 ps. Spectral width increases monotonically from 2 to 16 nm indicating that dechirped pulses with less than 400 fs duration can be obtained. It is important to note that the maximum spectral width calculated inside the cavity is about 24 nm.

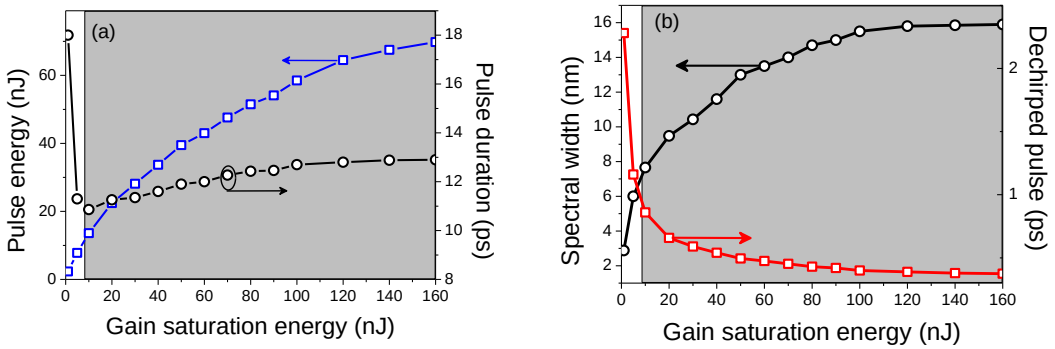

Figure 2-8 The evolution of performances versus pump power. Gray regions: single and multi-pulses solutions coexist.

Let us now give more details on the single pulse solutions predicted for this laser configuration. The results obtained for E_{sat} = 15 nJ are depicted on Figure 2-9. Pulse evolution along the cavity shows that pulse stabilization is particularly governed by the spectral filter (Figure 2-9(a)). The high-stretching ratio undergone by the pulse when propagating along the DCF is converted into amplitude modulation by the narrow spectral filter thus ensuring pulse self-consistency in the spectral and time domains. The saturable absorber plays a minor role in the stationary regime but the use of a high-contrasted SAM is crucial to initiate the pulsed solution from noise. We note the asymptotic evolution of the pulse duration and spectral width along the DCF, suggesting as previously a self-similar pulse propagation. This is confirmed by the characteristics of the calculated solution which presents a quasi-parabolic temporal profile with 10.8 ps width and a linear chirp as shown on Figure 2-9(b). Pulse compression considering a pair of diffraction gratings predicts the generation of transform-limited pulses of 862 fs duration.

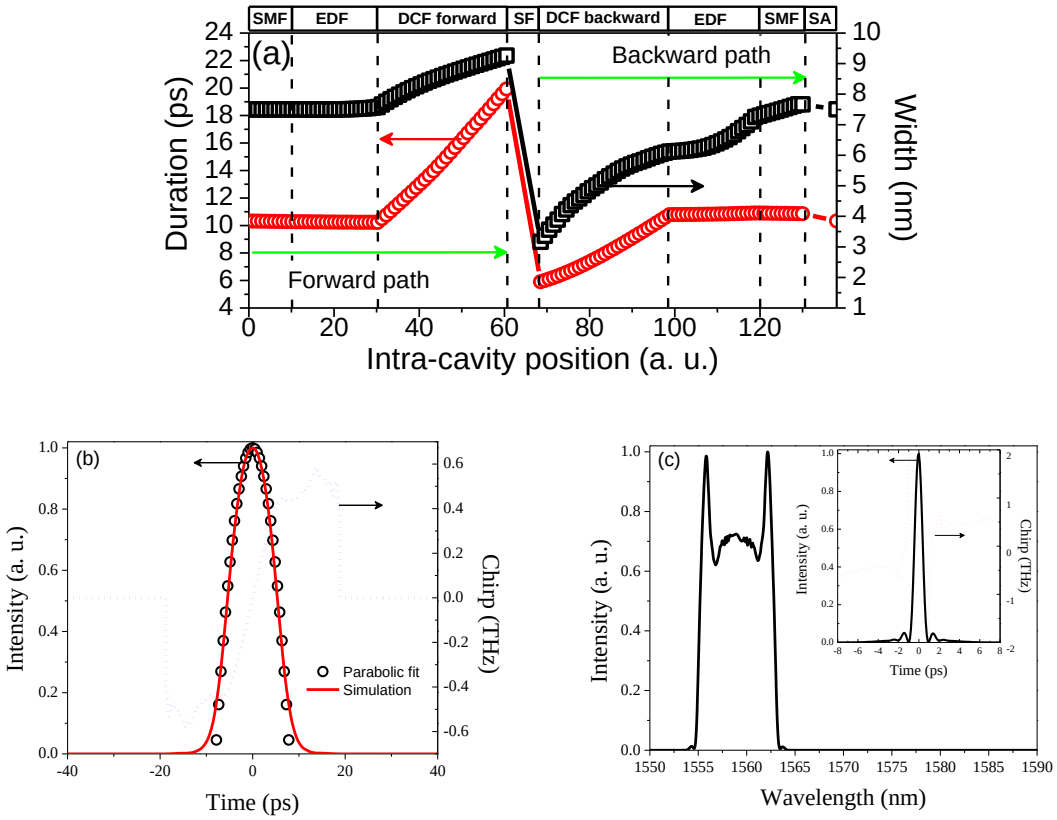

Figure 2-9 Numerical simulations for 10 m DCF and 4.5 nm spectral filter at an intra-cavity pulse energy of 20 nJ: (a) pulse evolution along the unfolded cavity; (b) output pulse calculated before the SA; (c) corresponding optical spectrum and dechirped pulse. The dashed curves correspond to the instantaneous frequency.

The pulse solution exhibits a typical M-shaped spectrum which is characteristic for normal dispersion fiber laser with spectral filtering. However, the analysis of the pulse characteristics using the kurtosis parameter shows that the pulse shape evolves from a Gaussian to a parabola when propagating along the cavity (Figure 2-10). Compared to the laser configuration without passive spectral filtering, pulse temporal shape endures stronger variations passing from a quasi-Gaussian profile to a parabola. The parabolic shape is reached at the end of the DCF in the forward direction, just before the spectral filter (SF). In addition, the spectrum is broader at this specific position (see Figure 2-9(a)) suggesting that shorter pulses can be obtained by optimizing the position of the output coupler. We observe that pulse shape is less affected when propagating along the gain fiber and the anomalous dispersion segments.

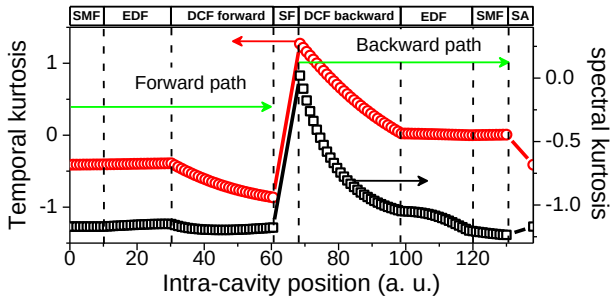

Figure 2-10 Evolution of the temporal and spectral pulse kurtosis when propagating within the different segments of the cavity.

As spectral filtering is necessary to stabilize mode-locking in the high normal dispersion regime, a straight forward idea is that a higher pulse energy should require a narrower filter to compensate the spectrum broadening from SPM. So, for a certain cavity configuration, there should exists an optimal value for the filtering bandwidth that would maximize the output pulse energy. Our simulations show that increasing the SF bandwidth prevents access to stable solutions at high energy levels. Moreover, the consideration of very narrow SF bandwidths promotes the formation of multiple pulse regimes against the single pulse regime. Guided by the experimental results reported in chapter 2, we limited our study to spectral bandwidths in the range 3-5 nm. By increasing the length of the DCF, we observe that pulse stabilization became more and more difficult to achieve.

2.5 Fiber lasers featuring high-dispersion active fibers

In this section, we study another mode-locked laser configuration which is based on the use of high normal dispersion active fibers. With this aim in view, we consider the simplified numerical laser model depicted in Figure 2-11, which is a ring cavity consisting of a normal dispersion gain fiber, an output coupler and a saturable absorber for mode-locking initiation and stabilization. It is worth noticing that there is no additional component for dispersion management except the active fiber. As in previous sections, we consider an instantaneous saturable absorber model with a high modulation depth of 90 % and 10% linear reflectivity.

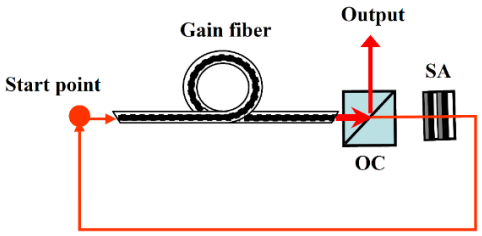

Figure 2-11 Schematic representation of the numerical laser model. OC: output coupler; SA:

saturable absorber.

We first consider a large mode area active fiber with a core diameter of 20 μm (mode-field diameter of 16 μm) and a dispersion of +0.025 ps^2/m which corresponds to the dispersion of silica around 1040 nm. The other parameters of the active fiber are summarized in **Table 2.2**.

Table 2.2 Large mode area Bragg fiber parameters

Parameter	Unit	Value
Length	m	2
Mode field diameter	μm	16
Mode field area	μm^2	200
Kerr coefficient	$W^{-1}m^{-1}$	6×10^{-4}
Small signal gain	m^{-1}	3.5
Gain bandwidth	nm	40

Figure 2-12 shows the typical solutions predicted in such laser configuration for a gain saturation energy of E_{sat}=10 nJ. The corresponding pulse energy is calculated to be 31 nJ at the end of the active fiber. The pulse solution presents a Gaussian temporal profile with 6.2 ps width. The corresponding spectrum exhibits a parabolic central part with steep edges which are typical of all-normal-dispersion fiber lasers. The spectral width is 13.5 nm. This highly chirped pulses could be dechirped to 249 fs duration using a second order dispersion element indicating that their chirp is mostly linear. Indeed, the dechirped pulse is very close to the theoretical limit of 230 fs obtained by Fourier transformation of the spectrum assuming a zero phase relation.

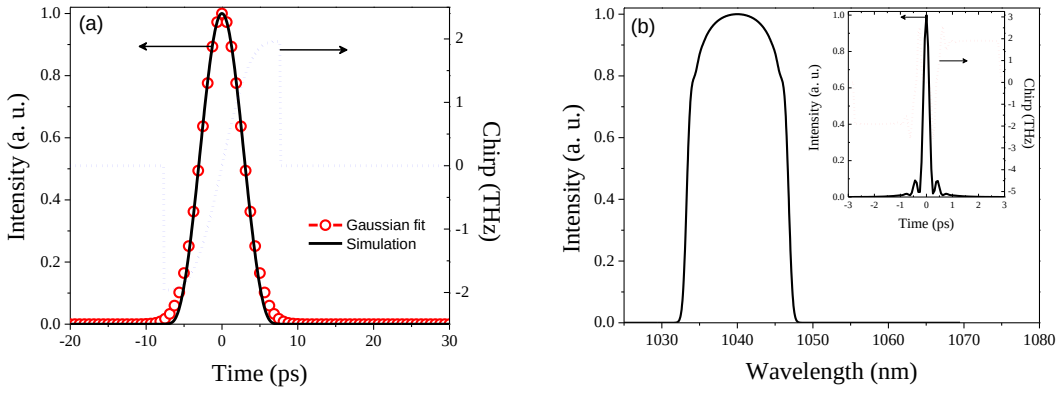

Figure 2-12 Laser outputs predicted for a pump level of E_{sat}=10 nJ: (a) Temporal and (b) spectral pulse shapes. Inset: dechirped pulse shape. The dotted curves correspond to the instantaneous frequency.

Simulations are conducted by varying the pump parameter along with the adjustment of the

saturation power of the saturable absorber. The corresponding results are summarized in Figure 2-13. It appears that pulsed solutions with pulse energies as high as 200 nJ can be achieved in this laser. However, it is worth noting that these results have been obtained using a Gaussian pulse as an initial condition. When starting from noise, we noticed that the fixed solution cannot be reached for pulse energy levels higher than 40nJ. In the region corresponding to self-starting solutions, the temporal and spectral widths increase with pump power. This is different in the gray region where pulsed solutions are not self-starting from noise. Indeed, in this case pulse duration decreases with pump power indicating that pulse dynamics is highly impacted by the gain filtering as already shown in reference [64]. The performances predicted in the self-starting region are compatible with the results achieved in a mode-locked fiber laser based on an Yb-doped Bragg fiber operating far from resonance [60].

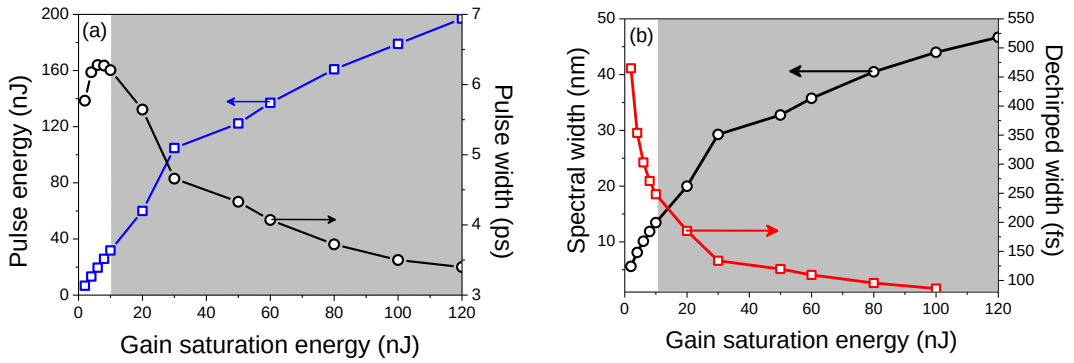

Figure 2-13 Laser performances versus pump power: (a) pulse energy and duration; (b) spectral width and dechirped pulse duration.

To simulate the operation of a mode-locked laser based on a high-dispersion fiber, we used the laser scheme of Figure 2-11 and implemented an active fiber characterized by the dispersion curve shown in Figure 2-14. This corresponds to a maximum second order dispersion of D= -1500 ps/km.nm at 1040 nm with a narrow spectral width as expected for a Bragg fiber operating near resonance. The high dispersion region considered here presents a full width at half maximum of about 10 nm. The dispersion terms corresponding to this curve are as follow: $\beta_2 = +0.86\, ps^2/m$; $\beta_3 = +28 \times 10^{-5}\, ps^3/m$; $\beta_4 = -84 \times 10^{-4} ps^{-4}/m$. The rest of parameters are similar to those given in **Table 2.2**.

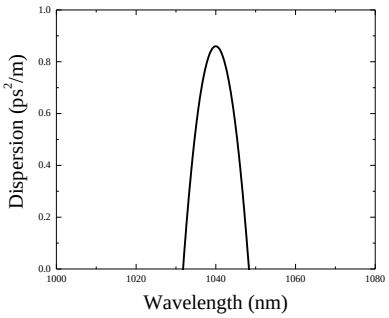

Figure 2-14 Typical dispersion curve used to simulate the high-dispersion fiber according to the

parameters listed in Table 2.2

The typical results obtained at moderate pulse energies are shown in Figure 2-15. These results are obtained at E_{sat}=10 nJ leading to a pulse energy of 32 nJ. The predicted solution exhibits a parabolic profile with a linear chirp suggesting a self-similar pulse propagation inside the cavity. The pulsed solution presents temporal and spectral width of 35 ps and 0.8 nm, respectively. Using a second-order dispersion element, these solutions are dechirped to their Fourier limited duration of 3 ps (Figure 2-15 (b)).

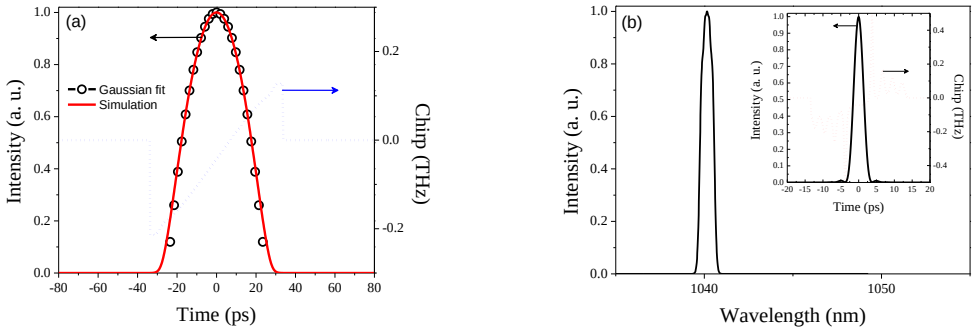

Figure 2-15 Pulsed solution predicted in the case of high-dispersion active fiber for a pump power of E_{sat}=10 nJ: (a) temporal profile and instantaneous frequency; (b) spectral profile and (inset) dechirped pulse.

Numerical simulations allow also to study the intra-cavity pulse dynamics and thus bring out the most important mechanisms governing pulse stabilization. Figure 2-16 shows the evolution of the pulse temporal and spectral widths along the cavity for a gain saturation energy of 10 nJ in both laser configurations. In the case of a standard dispersion fiber, the spectral filtering arising from the limited gain bandwidth plays a key role in pulse shaping. The central frequency components are more amplified than the wings leading to spectral narrowing in the first part of the gain fiber. As it acts on highly chirped pulses, this spectral filtering induces some pulse shortening which opposes the dispersion effect and thus reducing the pulse lengthening rate in the first portion of the gain fiber. Towards the middle of the gain fiber the pulse peak power level is enough to onsets spectral broadening through Kerr effect. Pulse stabilization inside the cavity results from the combined actions of the saturable absorber and gain filtering.

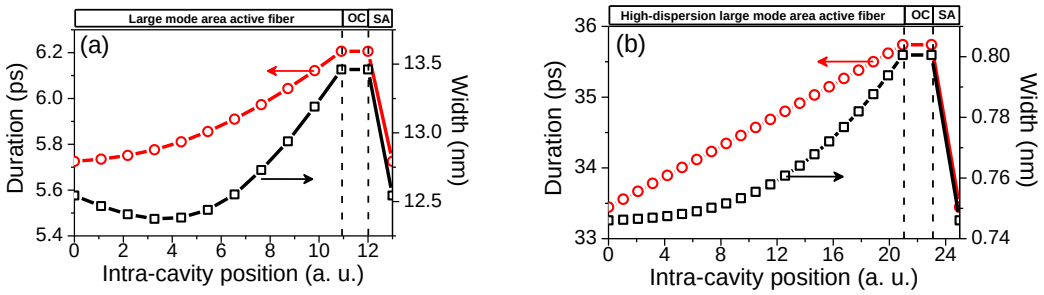

Figure 2-16 Pulsed solution dynamics along the cavity for a gain saturation energy of 10 nJ for a

large mode area fiber with (a) standard dispersion value and (b) resonant dispersion curve.

But the situation is very different when the fiber is operating near its dispersion resonance wavelength. In this case, pulse duration increases monotonically along the high-dispersion gain fiber indicating no gain filtering effect. The high-dispersion dominates pulse propagation leading to the formation of long pulses with a narrow spectrum which is less affected by the limited gain bandwidth. Mode-locking stabilization in this case solely relies on the saturable absorber, which acts not only as an amplitude modulator to compensate pulse lengthening but also as a spectral filter to compensate spectral broadening.

To study the energy scaling potential of the high-dispersion fiber laser, we studied the evolution of the pulsed solution performances when varying the gain saturation energy. The results obtained using the fiber parameters given in **Table 2.2** along with the dispersion curve of Figure 2-14 are summarized in Figure 2-17. Stable single-pulse solutions are obtained for pump levels as high as 300 nJ suggesting that pulse energies higher than 1 μJ could be achieved from this laser configuration. We note that pulse duration and spectral width increase monotonically with pumping to reach 106 ps and 2.68 nm, respectively. As expected the dechirped pulse duration decreases with pumping but remains in the picosecond range.

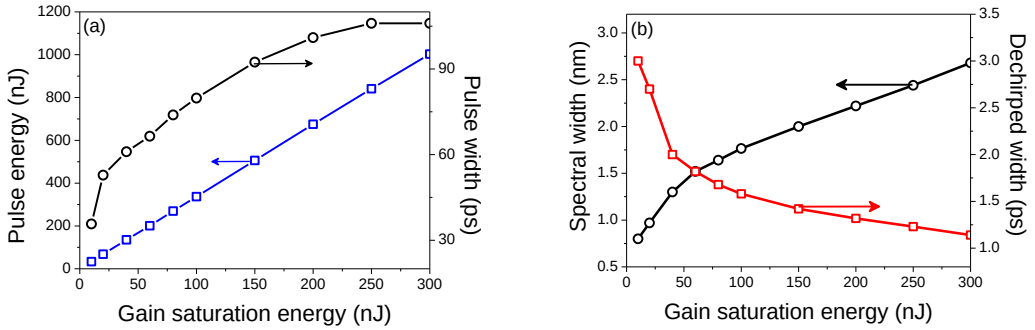

Figure 2-17 The evolution versus pumping of (a) Pulse energy and duration and (b) spectral width and dechirped duration.

To approach closer the dispersion characteristics of the Bragg fiber near resonance, we increased the value of the fourth order dispersion term (β_4) by an order of magnitude to -0.084 ps^4/m. The bandwidth of the high-dispersion region is thus reduced to 3.5 nm. In these conditions, no stable solution is achieved for gain saturation energies higher than 60 nJ which corresponds to a pulse energy of 200 nJ. The results obtained for lower energies are closely similar to those presented above. It seems that stability limit of the single pulse solution is reached when its spectral width approaches half of the high-dispersion bandwidth window. It is worth noticing that the simulation is based on an unchanged mode field area, while when the resonance occurs part of the energy would be coupled into the ring mode and would lead to an increase of the mode area. It is expected that the mode area increase will soothe the spectral broadening induced by SPM and partially compensate for the limitation due to the steep dispersion curve, and thus opening the possibility to approach the performances predicted in

Figure 2-17.

2.6 Conclusion

In this chapter, we numerically studied the dynamics of mode-locked fiber lasers featuring high intra-cavity dispersion pursuing two different approaches. In the first section, we developed an approach based on the use of high-normal dispersion passive fiber inside the cavity. Our results show that high energy ultra-short pulses can be produced but their initiation needs for strong mode-locking mechanisms both in the time and spectral domains. The combination of a high-modulation depth saturable absorber with a narrow bandpass spectral filter seems to be very adapted to initiate and stabilize ultrashort pulses with several tens of nanojoules energy. In the second section, we studied another approach based on the use of high-dispersion active fibers such as Bragg or W-type fibers. Our results show that the high dispersion regime could come with more favorable pulse energy, but narrower spectral width, which would prevent the pulse from being dechirped to sub-picosecond duration. Nevertheless, the predicted performances in terms of pulse energy are very appealing for ultrafast fiber laser technology and merit to be explored experimentally.

Chapter 3. Dispersion managed erbium-doped fiber laser

In this chapter, it will be first introduced the current state-of-art technologies and concepts used to obtain significant energy scaling in mode-locked fiber lasers operating in the telecommunication window around 1.5 μm. The key ideas of those state-of-art technologies will be briefed and both their advantages and drawbacks will be analyzed. It will then be presented our contribution around the concept of dissipative soliton laser. The design and structure of the laser will be explained in detail, and so will be the experimental procedures. Several selected results obtained during this thesis will be presented to show the current performances of this laser and the great potential of such dispersion managed laser featuring high normal total GVD for energy scaling. We then compare these results with those from numerical simulations of chapter 2. The amplitude noise features of the developed laser will be evaluated using radiofrequency analysis. The timing jitter will be also discussed qualitatively. Finally, we will introduce a FOPO employing this laser source to demonstrate a way to extend the laser's spectral range utilizing parametric frequency conversion. This FOPO system features being an almost all-fiber system with satisfying performances for bio-photonics and metrology applications.

3.1 Introduction

The development of high-energy ultrafast fiber lasers has attracted much interest in recent years due to their inherent advantages such as compactness, stability, high-power, and turnkey operation. Driven by several industrial and scientific applications such as material processing, nonlinear microscopy and high-field physics, the output power of ultrafast pulsed fiber lasers has undergone an impressive growth during the past decade [2]. In particular, the advances made in mode-locking mechanisms in combination with the emergence of novel fiber technologies have led to the development of high-power ultrafast fiber oscillators emitting multi-watt-level power with sub-100 fs pulses [17][65][66]. This constitutes an alternative to the complex and expensive femtosecond amplification systems. However, these developments have mainly concerned 1 μm laser sources due to the high efficiency of ytterbium and the normal material dispersion at this wavelength which is favorable for energy scaling through nonlinearity management. The extension of these developments to the eye-safe spectral region above 1.5 μm can benefit for many applications such as free-space telecommunications, range

finding, remote sensing and medical procedures.

Significant energy scaling in mode-locked fiber oscillators is obtained by exploiting the concept of dissipative soliton lasers [67]. These lasers, also known as chirped-pulse-oscillators (CPO), operate at high-normal dispersion and generate highly chirped pulses that can be compressed close to the theoretical limit fixed by their spectral width [16][68]. The development of high-nonlinearity semiconductor saturable absorbers mirrors (SESAM) helped to implement practical dissipative soliton sources routinely delivering energies of several nano-joules at 1.55 μm [46]. The best performances have been obtained using an all-normal dispersion Erbium-fiber laser mode-locked by nonlinear polarization evolution (NPE) leading to the generation of 750 fs pulses with 20 nJ energy [69]. However, the generated pulses suffer from a large pedestal which contains more than 50% of the total energy [9]. More recently, it has been shown that combination of normal dispersion gain fibers with narrow spectral filtering in mode-locked fiber lasers promotes the formation of optical similaritons thus paving the way for high-energy sub-100 fs pulse generation [70][71]. A self-similar Er-fiber laser drawn on this concept has been demonstrated recently [72]. It produces high-energy chirped pulses which can be de-chirped down to 70 fs.

3.2 Motivation and design principles

The first demonstration of dissipative soliton regime in all normal dispersion fiber laser intrigued many efforts to boost the energy scaling ability of fiber lasers. As 1550 nm is an interesting wavelength window and has found applications in fields like telecommunication, it is a nature ideal to build high energy fiber lasers working at this wavelength employing the same techniques. A difficulty for development of this kind of lasers is the availability of normal dispersion fiber-based components at this wavelength. Commercial single mode fibers (SMFs) such as SMF28 or OFS980 exhibit anomalous dispersion around 1550 nm, and these fibers are integrated in nearly all the fiber-based components commercially available including isolators, WDMs and couplers. Although ANDi fiber laser with stable mode-locking and good energy performances are reported [69], it requires the usage of homemade fiber-based components with fiber of normal dispersion, a fact which makes such design cost-unfriendly and hard to be put into wide use.

To overcome this limitation, we put our eyes on the dispersion managed regimes, because there are commercially available dispersion compensated fibers (DCF) which have normal dispersion at 1550 nm. As shown in the previous chapter, the introduction of high net normal dispersion into the cavity could lead to the emergence of self-similar parabolic pulses with high energy levels from a mode-locked fiber laser.

Guided by the simulations of Chapter 2, we designed a Fabry-Perot laser including a long piece

of DCF to tailor the total GVD of the cavity and combining several mode-locking mechanisms to ensure single-pulse and self-starting operation. Indeed, a high-modulation depth semiconductor saturable absorber in combination with NPE are used to ensure self-starting mode-locking. Moreover, for large normal dispersion amounts, the addition of spectral dissipative mechanism has proven necessary to stabilize the dissipative soliton-like regimes observed in such laser configurations. A diffraction-grating-based filter could be a good choice as it offers the possibility to manage the filtering bandwidth. Having all these elements in mind, it is designed the dispersion managed laser cavity in which some interesting mode-locking regimes were observed and would be discussed in the following parts of this chapter.

3.3 Experimental configuration

The experimental setup of the large normal dispersion oscillator is shown in Figure 3-1. Some of the polarization control components are not depicted in Figure 3-1. There is a half-waveplate between the output of DCF and the grating used to optimize the grating efficiency, and a half-waveplate between the polarizer and the intracavity output of the coupler to serve as the NPE mechanism. The cavity consists in a Fabry-Perot cavity comprising 1.2 m heavily erbium-doped single mode fiber (EDF) with a core mode field diameter of 4.3 μm and a NA of 0.29 at 1550 nm. The EDF presents an unpumped peak absorption of 80 dB/m at 1530 nm and its group velocity dispersion (GVD) has been estimated around +61 ps^2/km at 1550 nm. The EDF is pumped through a 980/1550 wavelength division multiplexer (WDM) using a single-mode Yb-doped fiber laser system (Azur light systems Inc.) emitting more than 5 Watts at 977 nm. A segment of dispersion-compensating fiber (DCF) is added and optimized-in-length in order to build a highly normal dispersion cavity. The GVD of the DCF used has been measured around +116 ps^2/km. The rest of the cavity comprises a minimized-in-length 90/10 coupler (SMF28 β_2=-22 ps^2/km), coupling lenses and a resonant semiconductor saturable absorber mirror (R-SAM). The 90% port of the coupler is used as the laser output. The saturable absorber has a modulation depth of 38%, a saturation fluence of 3.8 μJ / cm^2 and a relaxation time of 2.3 ps. A 600 lines/mm reflection grating is inserted in one end of the cavity. Its combination with the aperture-limited lens (L_1) provides a narrowband-pass filtering of Gaussian shape which plays a key role in mode-locking stabilization. The grating-lens filter has the advantage of being highly adjustable: the pass-band center wavelength can be adjusted by changing the incidental angle, which would also lead to a change in the filter bandwidth, and the bandwidth can also be adjusted by changing the distance between the grating and the lens.

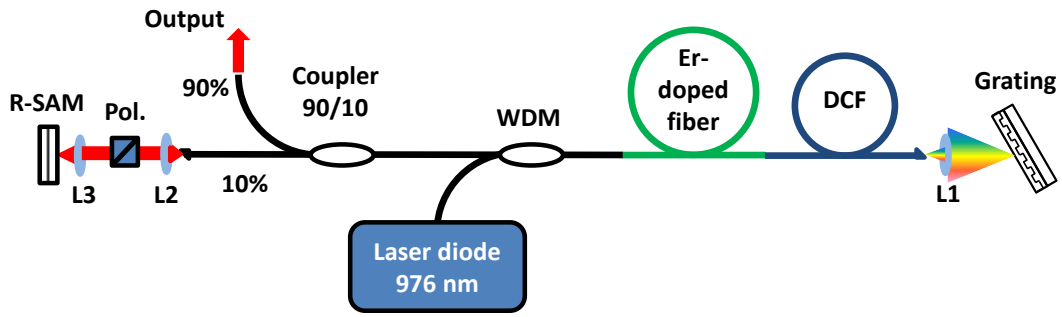

Figure 3-1 Experimental setup of the fiber CPO. WDM: 980/1550 nm multiplexer; L1, L2, L3: AR-coated coupling lenses; 90/10: output coupler; R-SAM: resonant saturable absorber mirror; DCF: dispersion-compensating fiber; Pol: polarizer.

During the experiments, the single pulse operation is monitored with a fast photodiode and a 5 GHz sampling oscilloscope which corresponds to 180 ps time resolution, and further confirmed with a long span autocorrelator (200 ps). The amplitude stability of the mode-locked pulse train was evaluated by radio frequency (RF) measurements using the power spectra obtained with a microwave spectrum analyzer via a high-speed photo detector (8-GHz bandwidth).

As our laser is designed to work mainly in the high normal dispersion regime, the output pulses should be highly chirped. To dechirp the pulses outside the cavity, a pair of transmission gratings with 1000 lines/mm and 92% diffraction efficiency were used.

3.4 Experimental results and discussion

In our experiments, we started from an oscillator without any DCF, under which configuration the only component which exhibits a normal dispersion is the erbium doped active fiber itself. The total dispersion of this system is close to zero and it was then expected to support a stretched pulse regime. The purpose of building this cavity is to have certain baseline to compare with the results from the later experiments. We then add a piece of DCF into the cavity and increase its length progressively to make the oscillator operation regimes evolving from a moderate- to a strong-normal dispersion regime. The aim of this procedure is to study the influence of the total cavity dispersion on the performances of the oscillator in terms of energy scaling and pulse duration. From the numerical simulation, we expect that a high total dispersion would monotonically add to the laser's performance so that it could produce high energy pulses which are compressible to very short durations. It can also be found the limit of this method during the procedure.

We experimentally proceed as follows. With each length of DCF included inside the cavity, different regimes were searched for by careful-alignment of the cavity and adjustment of the grating and the polarization controlling components. Each regime of stable mode-locking is well characterized, and its spectrum and AC traces are recorded. Then the DCF was removed

and a new piece of DCF with different length would be spliced back to the cavity. By repeating these procedures, it is studied the dynamics of the laser under different total GVD while other conditions are almost unchanged. The repetitive splicing between the EDF and the DCF was however inevitable. So, the length of the EDF was gradually reduced as our experiments progressed. The total loss in length is estimated around several centimeters, a loss that should have no impact on the system operation. The splicing procedures were carried out under good inspection so that any chances of quality imperfection such as MFD mismatch could be avoided.

3.4.1 Dispersion managed soliton laser

As the erbium doped fiber and other fibered components possess dispersion of opposite signs, the oscillator should run in a dispersion managed regime even without the presence of DCF. The AC traces and the spectrum measured at the output of the laser are depicted in Figure 3-2, where the traces are well fitted assuming a soliton regime with a hyperbolic secant square intensity profiles both in temporal and spectral domains. This indicates that the GVD of the fiber laser is close to zero in this configuration. Indeed, the cavity length is estimated to be 2.5 meters and the total GVD is about +0.04 ps^2. Under the pump power of 160 mW, the pulse duration derived from the autocorrelation trace is estimated to be 870 fs. The optical spectrum exhibits a width (FWHM) of 3 nm leading to a time-bandwidth product of 0.326 indicating that output pulses are very close to their Fourier limit. The laser generates an average power of 32 mW at the repetition rate of 34 MHz, corresponding to an energy per pulse of 0.94 nJ.

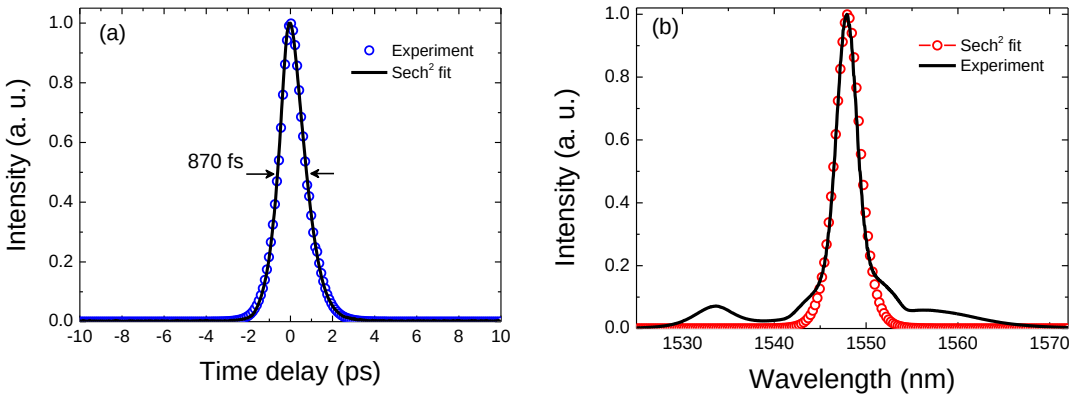

Figure 3-2 Dispersion-managed soliton laser outputs for 0.94 nJ energy: (a) AC trace and (b) optical spectrum (b).

Several stable regimes were found with this experimental configuration and all of them had similar soliton-like shapes in time and spectral domains. The regime shown in Figure 3-2 exhibits the highest pulse energy and further increase of the pump power only resulted in the loss of the mode-locking regime or the transition to random multiple pulse operation regimes.

According to the simulation results of Chapter 2, one solution to increase the pulse energy consist to add more normal dispersion to the cavity.

3.4.2 Dissipative soliton laser

The insertion of 1 meter of DCF is not enough to shift the total GVD to high normal regime but enough to bring the laser operation to self-similar regimes with non-negligible net GVD. It is a good practice to test if the laser can still be mode-locked with the DCF imbedded. With 1 meter of DCF fiber inside the cavity, the cavity length is increased to 3.5 meters and the total GVD is about 0.18 ps^2. The laser is thus considered dispersion managed cavity in normal dispersion regime, and this would result in a similariton pulse evolution with M-shape spectrum with sharp edges as discussed in the previous chapters. The pulse duration should then be greatly increased, and its peak power should be lowered, which should push to limits due to optical wave-breaking effect to higher pulse energy levels. Several stable mode-locking regimes were found during this stage, and an example of output pulse characteristics is depicted in Figure 3-3.

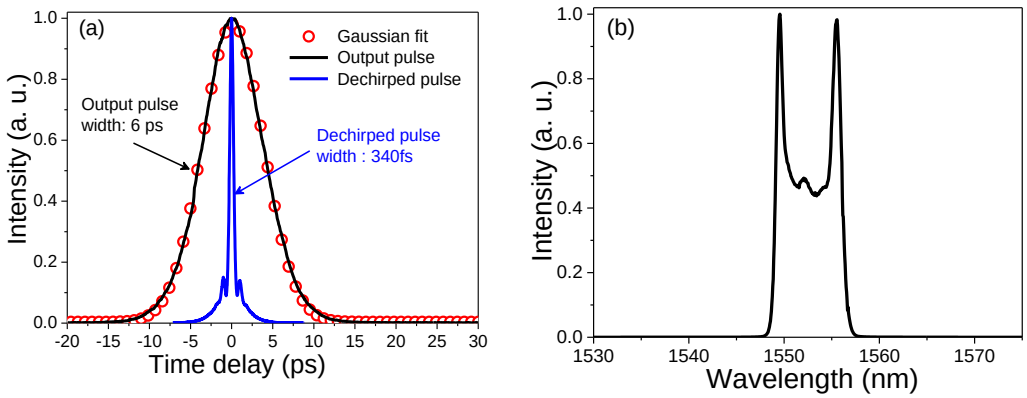

Figure 3-3 (a) AC traces and (b) spectra measured at the output of the laser with an 1-meter-long DCF.

The laser delivers 90 mW average power at a repetition rate of 25.5 MHz which corresponds to a pulse energy of 3.53 nJ. These performances are reached at a pump power of about 285mW. This represents a performance increase of 275% in terms of pulse energy compared to the previous case where no DCF is inserted in the laser. The optical spectrum exhibits an “M”-like shape with two steep edges as expected from a cavity with normal total GVD.

The output pulse duration calculated from the AC trace assuming a Gaussian pulse profile is 6 ps. In Figure 3-3(a) we can see that the Gaussian intensity profile constitutes the best fitting assumption. However, this assumption doesn’t hold true for the dechirped pulses. Because for these pulses with a “M”-like spectrum, the ideally dechirped pulse shape, which is deductible by Fourier transformation of its spectrum, is by far different from what one shall expect from pulses of Gaussian shape. So, the pulse duration after compression is deduced by the following

method: we calculate the chirp-free pulse profile by Fourier transforming the spectrum assuming a zero phase relation, and divide its AC FWHM by pulse FWHM to get the deconvolution factor. This factor would be used to calculate the experimental pulse duration from the FWHM of its AC trace. By these processes, the pulse duration estimated should not differ qualitatively from its real value. For the regime concerned by Figure 3-3, the factor is 1.64 and the pulse duration is about 340 fs. We note that this duration is shorter than the Fourier limit estimated to 370 fs. This is probably due to some nonlinear compression occurring in the standard fiber used for beam coupling to the autocorrelator.

To conclude, by adding 1 meter of DCF into the cavity, we successfully raised the pulse energy, and the pulse is compressible to the sub-picosecond level. This simple method was then proved to be efficient and deserving further investigation. It is worth mentioning that during this stage, the mode-locking can be achieved by using a mirror instead of the grating (refer to Figure 3-1). When the DCF length is increased to 5 meters or longer, the use of the grating-based filter is required to initiate stable mode-locking regimes at high-energy levels. This is in accordance with the simulation results of Chapter 2 which show that for moderate normal dispersion the pulsed solutions are accessible from noise.

In the following sections, we aim at pushing this methods to its limits by increasing the length of the DCF inserted inside the cavity. This will shift the laser to higher normal dispersion regime where the laser could have better energy scaling capability. This method is expected to be viable until the energy is increased to a level at which mode-locking initiation will become more challenging as already demonstrated numerically in Chapter 2.

3.4.3 High-normal dispersion dissipative soliton laser

With 10 meters of DCF inside the cavity, the cavity length is about 12.5 meters and the total GVD of the laser is estimated to be around 1.22 ps^2, a dispersion at which the laser should be mode-locked in a strong normal dispersion regime. At this level, mode-locking is not so easy to obtain and a careful adjustment of the focusing conditions on the SESAM and optimization of the passive filtering width are necessary. After many attempts, we succeeded in establishing a stable mode-locking regime. But when trying to increase the pump power to over 300 mW, a state transition from single pulse to multi pulse mode-locking was observed. We found afterwards that this transition is reversible by adjusting the angle of the intra-cavity polarizer and waveplates. Also, transitions between annihilation and production of mode-locking states, and transitions between regimes with different pulse characteristics were observed by turning these polarization-only modulation components. All these observations, which are in agreement with numerical simulations, led to the conclusion that NPE mechanisms combined with the SESAM action, which together provided a high modulation depth and reconfigurable

parameters, are necessary to stabilize the single-pulse mode-locking operation.

A typical regime under this configuration is well studied and reported in the previous publication of our group [73]. The laser outputs recorded in this regime are depicted in Figure 3-4.

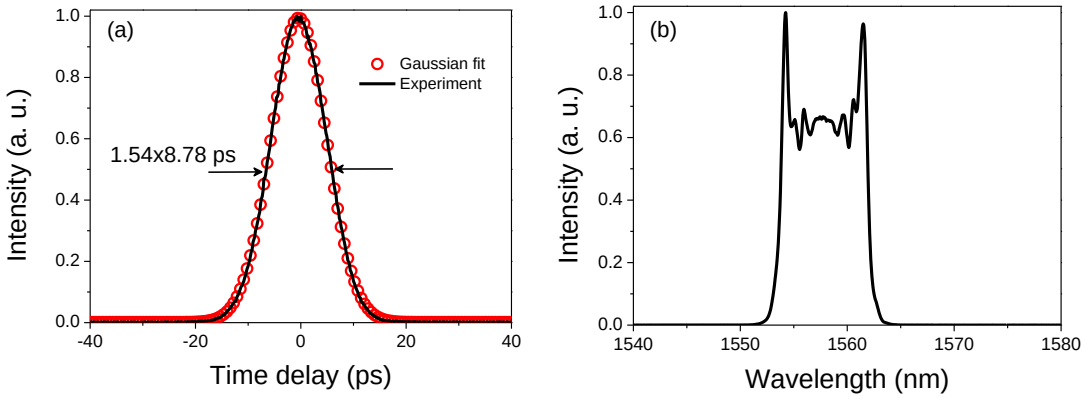

Figure 3-4 : Laser outputs for a pulse energy of 22 nJ: (a) AC trace and (b) optical spectrum

Under the pump power of 515 mW, the pulse duration of this regime is 8.8 ps, and the output spectrum exhibits a typical M-shape with 8.1 nm bandwidth. The extracted average power is 176 mW at the repetition rate of about 7.9 MHz, corresponding to a pulse energy of 22 nJ. The pulses are compressed outside the cavity using a pair of transmission gratings in double pass set-up. The compressed pulses exhibit a pulse duration of 624 fs, which is very close to the theoretical limit obtained by Fourier transformation of the optical spectrum assuming a zero-phase relation (see Figure 3-5). The dispersion needed to dechirp the output pulse is about -0.416 ps^2. Compared to the previous 1-meter-DCF configuration, the performance of the laser is improved by more than 520% in terms of pulse energy.

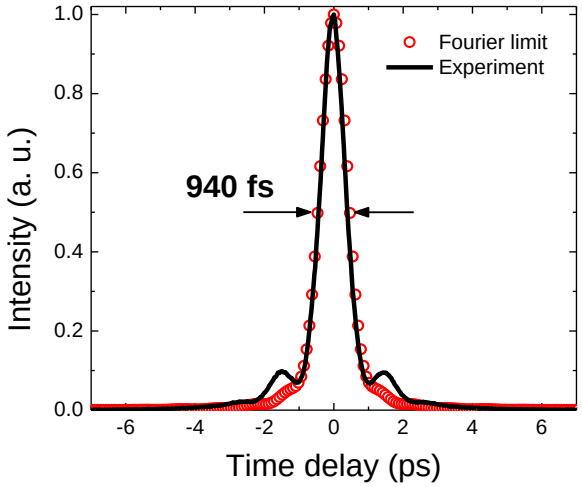

Figure 3-5 Autocorrelation trace of the extra-cavity dechirped pulses for 22 nJ output energy. The dashed curve corresponds to the AC trace of pulse resulting from Fourier transformation of the spectrum assuming a zero-phase relation.

So far, we successfully realized stable mode-locking with high pulse energy and very short pulse duration. But before moving to longer DCF, we wanted to investigate the pulse evolution inside the cavity and study its dynamics. As it is impossible to directly measure the pulse shape and its spectrum at arbitrary position inside the cavity, this study takes reference from numerical simulations detailed in Chapter 2. These simulations were fed by extracting the pulses at specific key positions in the cavity.

In order to have some experimental data to compare with and verify the simulation results, we then spliced a 2x2 10/90 coupler to the free space coupling port at the grating side (see Figure 3-1). The two 10% ports of the coupler allowed us to measure the spectra after the forward roundtrip of the Fabry-Perot cavity, and after passing through the grating-based filter. With these spectra, we are therefore able to evaluate and improve our simulations.

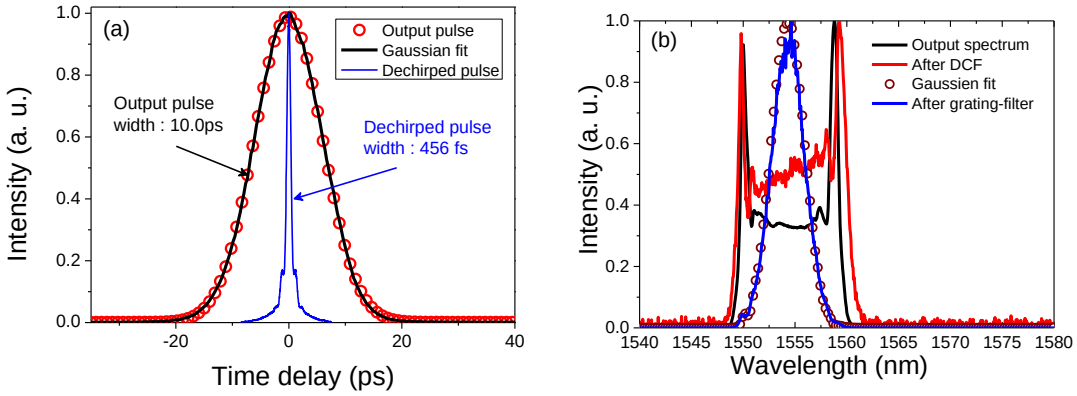

Figure 3-6 Laser outputs for 3.8 nm filter width and 30 nJ pulse energy: AC traces before and after extra-cavity compression (a) and optical spectra recorded at different position in the cavity.

Figure 3-6 shows the laser outputs after the intra-cavity coupler was deployed. Under the pump power of 740 mW, the pulse duration of this regime is 10 ps, and the output spectrum width is about 10 nm. We measured an average power of 223 mW at a repetition rate of about 7.3 MHz, which corresponds to 30 nJ of pulse energy. The pulse is dechirped down to 456 fs outside the cavity. The spectrum of the output pulse before and after compression were measured respectively, and no prominent evidence of nonlinear compression was observed. This regime exhibits a better performance compared to the previous regime in a very similar laser configuration. It is superior in both pulse energy and average power, and it produces shorter pulses. This regime observed is a proof that even in the same configuration, numerous regimes can be found and to some extents their performances may differ. It is worth noting that these results are achieved for a filter bandwidth of 3.8 nm, see Figure 3-6.

This self-starting regime was stable for hours and the pulse characteristics are highly repeatable after each restart. So, at this stage, we had achieved a laser performance which is comparable in terms of pulse energy and compressed duration to that reported in [69], which was the best performance reported at that time. Furthermore, our laser produced pulses of higher quality,

which can be compressed with lower pedestals.

3.4.3.1 Results from cavity with 15m DCF

Based on these remarkable results, the DCF length was again increased to 15 meters resulting in a total length of the cavity of about 17.5 m, including the free-space sections. This results in a repetition rate of 5.33 MHz to be expected from a mode-locking state, and the associated total GVD is estimated to be +1.83 ps^2. Following the same alignment procedure as mentioned above, a stable mode-locking regime is achieved under the pump power of 675 mW. The output average power is measured to be 204 mW, which corresponds to 38 nJ pulse energy. The laser outputs recorded in this regime are shown in Figure 3-7. The optical spectrum presents the typical M-shape with 8.4 nm width and the pulse duration 12.7 ps. Using a pair of transmission gratings, the output pulses are compressed down to 650 fs, which is about 1.4 times the Fourier limit.

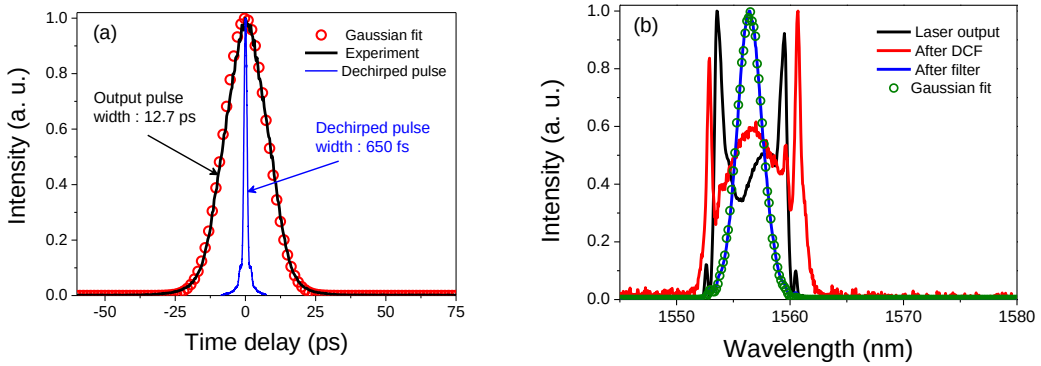

Figure 3-7 Laser output for 3 nm filter bandwidth and a pulse energye of 38 nJ: (a) AC traces before and after extra-cavity dechirping and (b) optical spectra measurement at different positions in the cavity.

At this power level, however, the capability of self-starting was lost, although the regime was retrievable by applying external perturbation such as rotating the wave-plate or realigning the SESAM. This regime is reached for a filter bandwidth of 3 nm as shown in Figure 3-7.

By increasing the filter bandwidth to 3.5 nm while keeping constant the dispersion map, we obtain a second regime corresponding to the characteristics presented in Figure 3-8. This regime exhibits a pulse duration of 15 ps and could be linearly dechirped to 726 fs, which is about 1.08 times its Fourier limit. The corresponding spectrum presented a nearly square shape with width of about 7.5nm. Under the pump power of 470 mW, the laser delivers an average power of 152 mW, which corresponds to a pulse energy of 29 nJ.

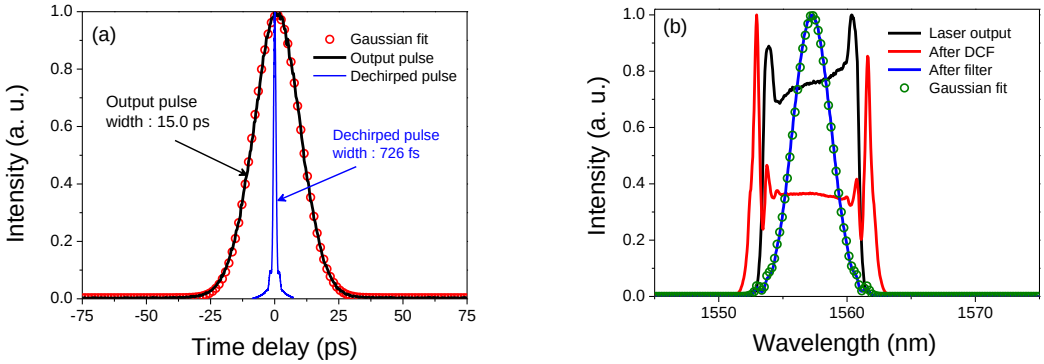

Figure 3-8 Laser outputs for 3.5 nm spectral width and a pulse energy of 29 nJ: (a) AC traces before and after compression and (b) optical spectra at different position in the cavity.

Comparing these two regimes, it could be concluded that when very high energy regimes are concerned, the pulses suffer from excessive nonlinear phase which hinders their compression to the theoretical limit.

3.4.3.2 Result from cavity with 30m DCF

This was a failed yet inspiring attempt to boost the laser performance in terms of energy scaling. The cavity length in this configuration is 32.5 m corresponding to the total GVD of about +3.57 ps^2. Stabilization of pure mode-locking became difficult and Q-switch mode-locking modes dominate laser operation. The only regime which was stable long enough to allow the collection of data is shown in Figure 3-9. The bad smoothness of the AC indicated an unstable pulse to pulse intensity. The spectra measured at different positions in the cavity also indicate that our method might be at its limit with this length of the DCF fiber. From Figure 3-9(b), it is clear that the spectrum of the pulse which is after the DCF in the forward roundtrip is distorted compared with its counterparts in the previous regimes. So, even without the existence of pump depletion, the pulse shaping mechanisms seems inefficient to ensure temporal and spectral pulse self-consistency under such high-dispersion values.

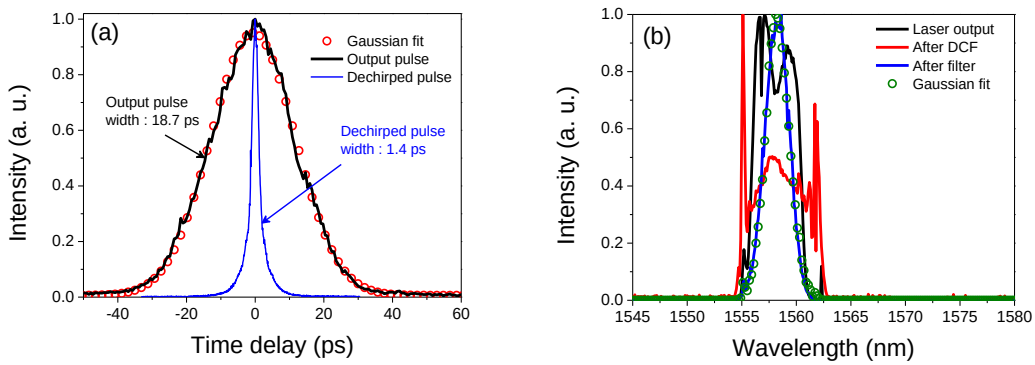

Figure 3-9 (a) AC traces and (b) spectra of laser with a 30 m DCF inside the cavity.

This regime is obtained at a pump power of 490 mW and produces an average power of 142 mW at a repetition rate of 2.94 MHz, corresponding to the pulse energy of 48 nJ. The output pulse duration is 18.7 ps, assuming a Gaussian shape, and it can be linearly dechirped to 1.4 ps, which is about 2 times its Fourier limit. Moreover, about 40% of the total energy is contained in the pulse pedestal indicating that output pulses suffer from a strong amount of nonlinear chirp.

Compared with the previous results, it can be concluded that the limit of the current cavity configuration is reached, and marginal improvement of performance may be possible by optimizing the length of the DCF.

3.4.4 Conclusion and discussion:

In this section, the performance of our erbium-doped fiber laser under different dispersion configurations are summarized and respectively discussed. Key attributes are shown in **Table 3.1** for some typical regimes.

Table 3.1 output pulse characteristics under different dispersion configuration. (FL: Fourier limit)

total GVD (ps2)/DCF length (m)	Pulse Energy (nJ)	Pulse duration (ps)	Compressed Duration (fs)	Spectral Bandwidth (nm)	Self-starting
~0/0	0.94	870	870 (~1 FL)	3	Yes
0.18/1	3.53	6.06	340 (~1 FL)	7	Yes
1.22/10	22	8.8	624 (~1 FL)	8.1	Yes
1.83/15	38	12.7	650 (~1.4 FL)	8.4	No/Resumable
3.57/30	48	18.7	1400 (~2 FL)	4.5	No

From the **Table 3.1**, it is prominent that enhanced total GVD is beneficial for energy scaling and such lasers can produce sub-picosecond pulses. However, when the DCF length is increased to certain value, though allowing larger pulse energy, mode-locking becomes more and more difficult to start from noise and the produced pulses suffer from excessive nonlinear phase thus hindering their compression to sub-picosecond durations. Some nonlinearity mitigation is still possible using another cavity arrangement to place the long DCF segment after the output coupler. The implementation of such a solution in the linear cavity configuration has not been successful probably due to the high cavity losses which hinders mode-locking initiation. The

exploration of a unidirectional ring cavity could be a solution to better tailor the nonlinear phase accumulated along the cavity and thus enable higher performance.

3.5 Amplitude Noise measurements

Intensity and phase noises measurements are an essential field of laser science. For a laser working in pulsing regime, the intensity noise describes the instability in the pulse power level. The phase noise, on the other hand, is the frequency domain representation of rapid, short-term, random fluctuations in the phase of the laser output's waveform, caused by time domain instabilities known as "jitter". The later represents the deviation from true periodicity of the laser's presumed repetition period. In this section, we will focus on the measurement of the amplitude noise of our laser system.

Many noise sources can contribute to the measured results and each of them should be identified properly before any characterization. Some of these sources originate in the interaction of instruments in the measurement system itself, which makes care and attention in system design a necessity.

The techniques employed to evaluate the intensity noise in our laser system are guided by many previous efforts in this field which has been well-documented. For those interested in this technique, it will be profitable to be familiar with reference [74], in which the authors introduced systematically the method of noise measurement starting from the basic principle of signal nature, to the detailed description of the measurement system design, and ending with examples of different lasers they characterized. Many subtle issues one needs to take care of in the noise measurement are highlighted.

The main parameter dedicated to describing the amplitude noise is the "RIN" (Relative Intensity Noise) which is defined as:

$$RIN = \frac{< P_n^2 >}{P_0^2}$$

Where $< P_n^2 >$ denotes the mean-squared optical noise power and P_0 denotes the average optical power. From its definition one may conclude that RIN is dimensionless, and it is always presented in "dBc" ("c" stands for "carrier") for convenience. As noise is frequency-dependent, RIN is commonly measured in "dBc/Hz" with respect to its frequency deviation from the carrier's.

Our noise measurement system is schematically depicted in Figure 3-10. The output signal is received by a photodiode detector and then amplified to be fed into the RF spectrum analyzer. Under this configuration, for the electrical carrier power P_c and the electrical noise power P_e, we have: $P_e \propto P_n^2$, and $P_c \propto P_0^2$. So, the measurement of optical RIN is equivalent to derive the electrical amplitude noise from an RF spectrum analyzer.

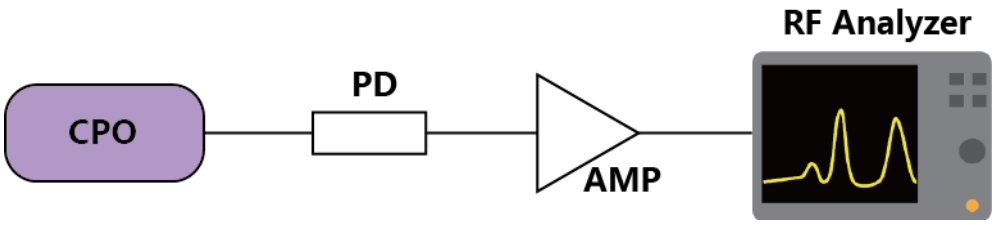

Figure 3-10 Schematic diagram of laser noise measurement setup. CPO: the laser discussed above as shown in Figure 3-1. PD: photodetector. Amp: electrical signal amplifier.

The noise measurements of the laser running in a regime with characteristics and dispersion configuration similar to those of Figure 3-4 are shown in Figure 3-11. As the RF spectrum analyzer has a noise floor about 20 dB above the thermal noise (-155 dBm/Hz vs. k_BT=-174 dBm/Hz), an amplifier with gain of 30 dB and noise figure of 5 dB is used to push the detection limit to -169 dBm. As the carrier power is measured to be -9 dBm, the theoretical detection limit is thus -160 dBc. The system noise floor is measured with all the electrical components connected and turned on, including the photodetector and the amplifier, but without any optical input. It is clear from Figure 3-11 that the actual noise floor level is in good accordance with the theoretical value. An important frequency-independent noise source, the so-called “shot noise”, which is a result of the discrete nature of electric currents, is also plotted in Figure 14. The shot noise in this system comes mainly from the photo-current of the detector, and is calculated to be around 1 mA, which corresponds to a noise level of -155 dBc.

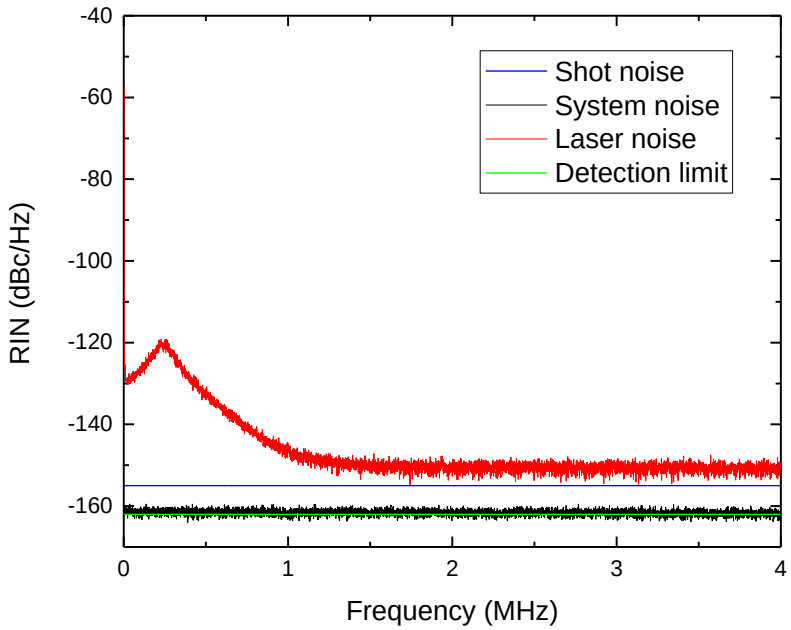

Figure 3-11 Measured optical noise and system noise floor shown alongside the calculated shot noise level and the system detection limit.

It can be confirmed from Figure 3-11 that the laser signal is shot noise limited at high-frequencies (from 1 to 4 MHz). Indeed, there is only a 5-dB gap between the laser optical noise level and the shot noise limit, which is an acceptable distinction level for a valid noise measurement.

The low frequency sideband is attributed to the spontaneous emission at 1530 nm and environmental fluctuations. Nevertheless, this sideband peak power is 120-dB below the carrier level indicating that amplitude stability of our laser is very good. The good performances of our oscillator in terms of output pulse energy and amplitude stability are very attractive for applications in Biophotonics. In this scope, we studied the potentiality of this source for fiber optics parametric oscillator pumping (FOPO) to produce ultrashort light pulses in the 1.7 μm wavelength range.

3.6 Application to parametric oscillators pumping

Fiber optical parametric amplifiers and oscillators based on degenerate FWM have attracted much interest for use in coherent Raman scattering (CRS) microscopy as they offer the possibility to generate two synchronized pulses with a tunable wavelength difference to enable selective excitation of specific molecular vibrations [75][76]. Recent advances in fiber technology in combination with the availability of high performances ultrafast ytterbium-doped fiber laser systems has permitted the achievement of record pulse energies from parametric amplifiers and oscillators operating around 1 μm [77][78]. Their application to SRS microscopy show that parametric oscillators offers better SRS-signal contrast due to their higher noise figure provided by the optical feedback [79][80]. Moreover, it is now well established that ultrafast laser sources emitting in the spectral range 1600-1800 nm are very attractive for many biomedical applications such as multi-photon microscopy [81]. Indeed, taking into account tissue scattering and absorption, it has been shown that the optimum wavelength window in terms of penetration lies around 1700 nm [81]. So, in this section we show our preliminary results on the use of a dissipative soliton laser to directly drive a fiber parametric oscillator operating in the vicinity of 1700nm.

The experimental setup is depicted in Figure 3-12. With the intra-cavity grating, the output wavelength is adjustable from 1546 nm to 1568 nm. To prevent the saturation of the gain medium, the output pulse energy is limited to ~9 nJ, with a pulse duration of 13±2 ps and a corresponding spectral bandwidth of ~4 nm. A fiberized isolator is used to avoid any optical feedback that could disturb the mode-locking stability. The FOPO is then pumped through the 90% output port of a coupler whose 10% port is dedicated to pulse monitoring. In the FOPO cavity, an 8.8 m custom DSF is used as the parametric gain medium. After the DSF, 90% of the power is coupled out to an autocorrelator (Femtochrome FR-103XL), and to an OSA (Anritsu

MS9710B / Yokogawa AQ6375 switchable depending on the wavelength range) through the second coupler whose 10% port launches the remaining power into the FOPO feedback branch. An optical delay line (ODL) comprising 3.45 meters of SMF (Corning MetroCor) and free-space elements is then used for synchronizing the round-trip time of the resonating pulses with the time delay between pump pulses. The free space section of the ODL - a lens for beam collimation/focusing and a metallic mirror - allows fine adjustments of the round-trip time. A polarization controller was also included to adjust the polarization of the fed back pulses to match that of the incoming pump pulse. The overall feedback of the FOPO cavity, including splicing losses, was measured to be about 0.11% at the input coupler. The operation of the system is stable for days.

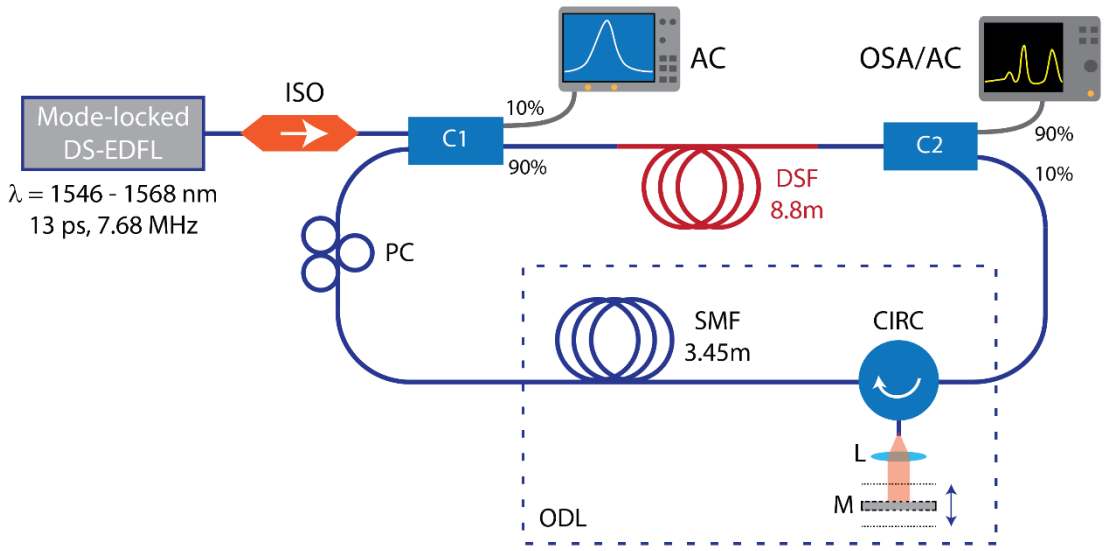

Figure 3-12 Experimental setup. DS-EDFL: dissipative soliton erbium-doped fiber laser, ISO: isolator, C1: input coupler, C2: output coupler, DSF: dispersion-shifted fiber, ODL: optical delay line, CIRC: circulator, L: lens, M: mirror, PC: polarization controller, AC: autocorrelator, OSA: optical spectrum analyzer.

Spectra of the generated parametric components and depleted pump were measured at the 90% port of the output coupler and selected spectra are shown in Figure 3-13. Tuning of the FOPO output wavelength was realized in two ways: (i) by changing the pump wavelength through adjustment of the EDFL intracavity spectral filter while maintaining the same level of output energy; (ii) via the time-dispersion-tuning technique by adjusting the FOPO cavity length, i.e. the delay in the ODL. Time-stretching by the group velocity dispersion (GVD) in the DSF and SMF together with the large initial chirp inherited from the pump laser indeed allows to dispersion-tune the oscillating wavelength by translating the mirror of the ODL. As a result, the output wavelength of the oscillator can be continuously tuned in a range as wide as 330 nm (up to 458 nm, but with much lower efficiency) around 1.55 μm. Figure 3-13 shows FOPO output

spectra corresponding to different ODL length under a pump at wavelength of 1565 nm, and the total output power extracted from the FOPO is 18 mW.

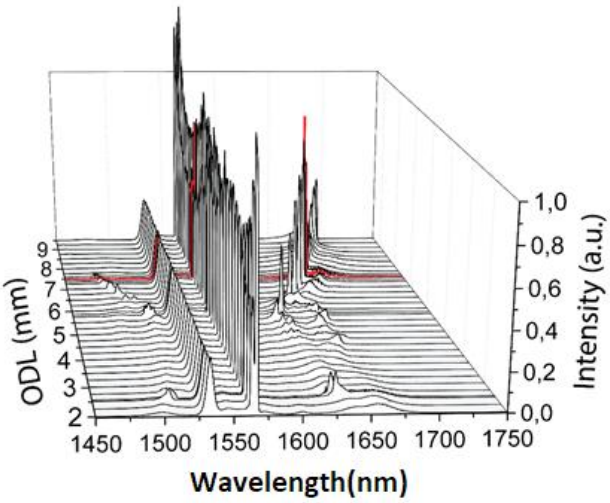

Figure 3-13 FOPO tuning by varying the ODL mirror position for a fixed pump wavelength lp=1565 nm. The highlighted red curve corresponds to the best conversion efficiency from the pump to the Stokes band (idler).

The highest idler pulse energy (and average power) achieved was ~2.5 nJ (19.1 mW) at λ_i = 1664 nm for a pump wavelength of 1566 nm, as shown in Figure 3-14, which corresponds to a 42% internal conversion efficiency on a 6-nm bandwidth. In this configuration, autocorrelation measurements prove a 4 ps pulse duration for the filtered idler as shown in Figure 3-14(b), which is a third of the temporal duration of the pump pulses. The high conversion efficiency obtained in this case can be explained by the energy transfer from the up-shifted parametric component (i.e. signal) to the down-shifted component (i.e. idler) due to a Raman assisted parametric process [82]. The modulation on the idler and signal spectra seen in the insets in Figure 3-14(a) is attributed to cross phase modulation (XPM) between strong pump pulses and parametric pulses [83].

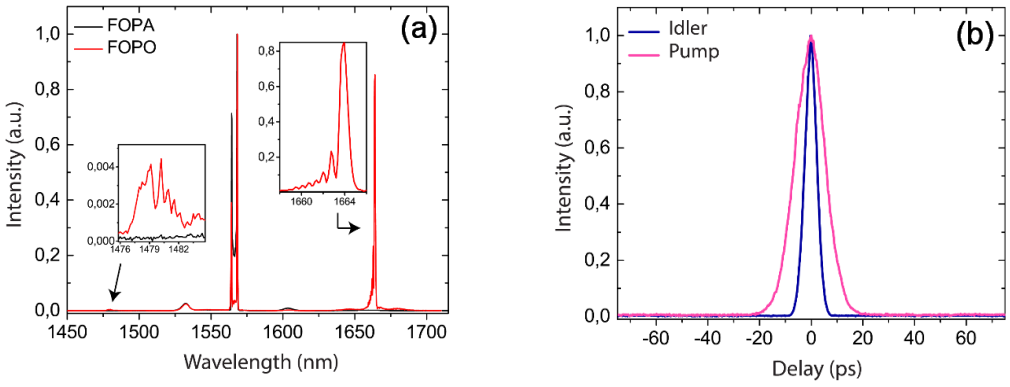

Figure 3-14 Laser system outputs: (a) optical spectra measure with (red curves) and without (black

curves) the feedback branch; (b) corresponding AC traces of pump at 1566 (violet curves) and idler at 1664 nm. Insets: signal and idler sidebands exhibiting XPM features.

3.7 Conclusion

In this chapter, we have demonstrated the generation of high-energy ultra-short pulses from a dissipative soliton mode-locked fiber laser operating at 1560 nm. Considering only the stable regimes with good pulse quality, highly chirped pulses with durations spanning from 8.8 to 10.5 ps with up to 38-nJ energy are generated in the large normal dispersion fiber laser configuration. These pulses can be dechirped down to 700-fs duration. To the best of our knowledge, this is the highest pulse energy level generated directly from a dissipative soliton Er-fiber oscillator operating at this wavelength. Numerical simulations show good agreement with experimental results and reveal that self-similar pulse propagation occurs in the normal dispersion passive fiber. Moreover, further energy scaling should be possible by using larger cavity dispersion in combination with tailored filtering bandwidths. Preliminary results obtained using a 30-m-length DCF show that picosecond pulses with more than 50-nJ energy can be achieved from this laser. More work (such as configuration optimization to avoid the high energy in DCF) is now needed to identify the optimal cavity configuration supporting high-energy sub-200-fs pulses.

The amplitude noise measurements conducted using radiofrequency analysis show that the developed oscillator is highly stable with a RIN level of -150 dBc/Hz in the range 1 to 4 MHz which is within 5 dB above the shot-noise limit of −155 dBc/Hz. As an example of application, our dissipative soliton laser has been used as a pump for a FOPO system. Using this original architecture, picosecond parametric pulses with energies exceeding 2.5 nJ were achieved around 1.7 μm. Although considerable potential is still left for improving the performances of our system, this study paves the way for the use of such a source in nonlinear imaging experiments in the so-called second near-infrared biological window, e.g. for three-photon microscopy, coherent Raman microscopy or optical coherence tomography [84].

As already discussed above, the concept based on the use of an extra DCF inside the cavity seems not scalable to very long fiber lengths due to the excessive nonlinearity induced along the DCF and the difficulty to initiate the mode-locking regime from noise. In next Chapter, we introduce another laser concept based on the exploitation of high normal dispersion active fibers.

Chapter 4. Mode-locked oscillators featuring high-dispersion active fiber

In the last chapter, we introduced the CPO concept to achieve high energy ultrashort pulses. The key mechanism of this design is to stretch the pulse in a certain stage of the cavity by including a passive dispersion compensating fiber to lower the peak power of the pulse and thus push the limits due to excessive nonlinearity at high-energy levels. In this chapter, we present and discuss another innovative solution based on the use of high-dispersion active fibers to combine both functions of pulse amplification and stretching. To achieve this goal, we have first explored this concept using an Yb-doped Bragg fiber which has the advantage of exhibiting high-dispersion in a large mode area but with a very narrow high-dispersion bandwidth. The spatiotemporal features of the laser outputs are analyzed in detail for operation near and far from dispersion resonance. The second approach discussed in this chapter consisted to use a W-type fiber which presents high-dispersion values on a broad bandwidth.

4.1 Mode-locked Bragg-fiber laser

The experimental setup of the oscillator based on the Bragg fiber is schematically depicted in Figure 4-1. It consists in a σ-cavity configuration build around a free space Faraday isolator. The input of the isolator was also used as the output coupler, with the half-wave and quarter-wave plates serving to adjust the coupling ratio along with optimizing the NPE mechanism. Two dichroic mirrors were used to inject the pump laser beam into the Bragg fiber and to get rid of the residual pump. The injection part from lens L3 was carefully aligned to optimize the excitation of the fundamental core mode. Different mode-locking regimes could be achieved and stabilized by adjusting the wave plates and the spot size of the beam incident on the SESAM. The Bragg fiber is the same as the Yb-doped one we introduced in Section 1.4.3.

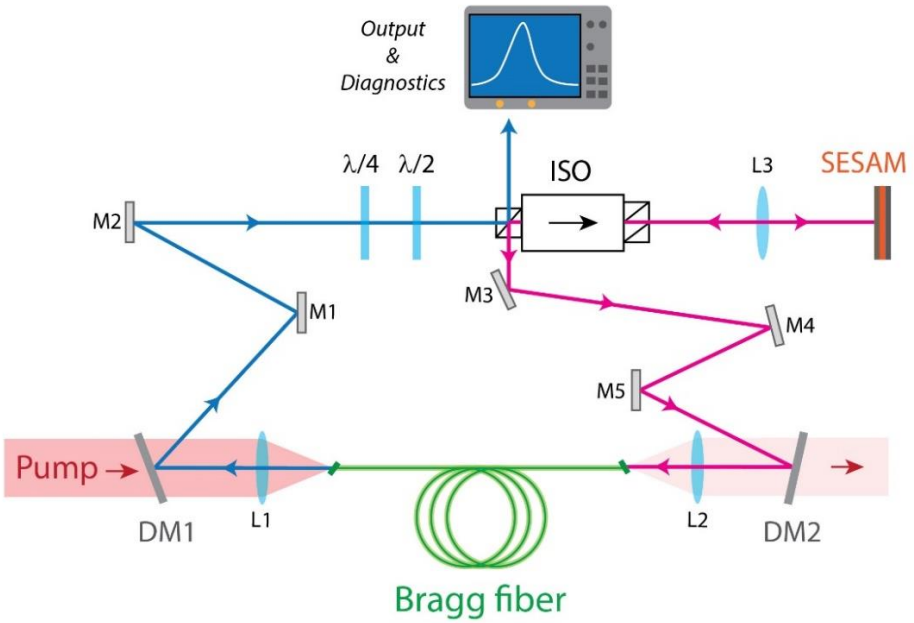

Figure 4-1 Experimental setup of the Bragg fiber laser. M1~M6: mirrors; DM1&2: dichroic mirrors; L1-L3: lenses; ISO: polarization dependent isolator.

It is worth noting that the segment of Bragg fiber we used in these experiments is located at the edge section of the fabricated fiber spool, so the uniformity is not good and this complicates the reproducibility of our results. Here we then discuss the typical results that have been retrieved several times using different sections of the Bragg fiber. Our results can be classified in two categories as predicted by the simulations discussed in Chapter 2.

The first category consists in the emission of short pulses with relatively broad spectra attributed to operation far from resonance of the Bragg fiber. We note that such regimes have already been studied in [60][85] where pulse energies as high as 30 nJ have been demonstrated. Similar results are retrieved in the early stage of this work before exploring the high dispersion operation regimes due to mode coupling. Figure 4-2 shows the laser outputs corresponding to a typical operation regime obtained in the early stage. Average powers as high as 830 mW at 27 MHz can be delivered by this laser corresponding to more than 30 nJ energy. The AC trace is well fitted assuming a hyperbolic secant square pulse intensity profile with 6 ps duration. We note that the AC trace presents two side-peaks delayed by 30ps from the center of the AC. This could be attributed to a residual high-order mode guided in the fiber core. From Figure 4-2 (b) we can recognize the typical steep-edged optical spectrum observed in all-normal dispersion lasers. The spectrum is centred at the wavelength of 1033 nm and has a Full Width at Half Maximum (FWHM) of 4 nm. Compression is achieved in a set of bulk gratings-based compressor. The dechirped pulse duration deduced from the AC trace using a deconvolution factor of 1.72 is 500 fs. This factor has been calculated using the pulse retrieved by Fourier transformation of the spectrum assuming a zero phase. By adjusting the wave-plates orientation

angles, we could jump to a distinct mode-locking regime.

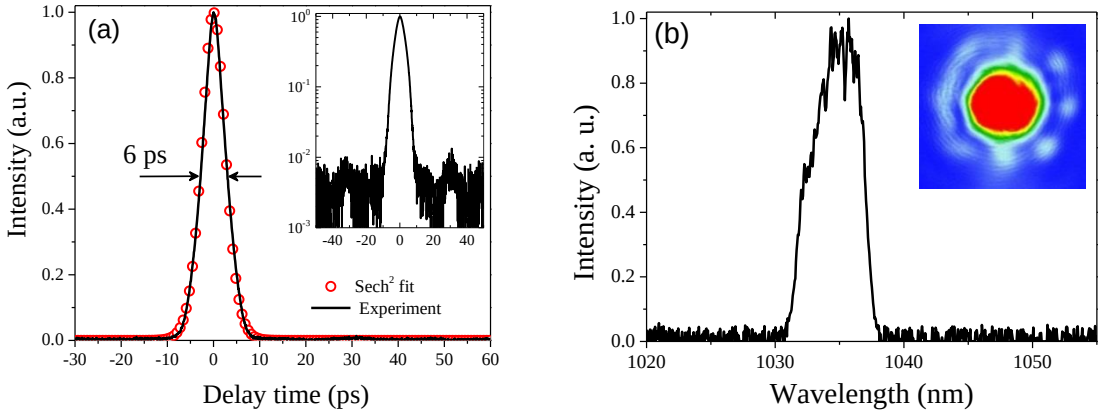

Figure 4-2 Laser outputs for fiber operation far from dispersion resonance at 30 nJ : (a) AC trace in linear and logarithmic (inset) scales; (b) optical spectrum and output beam profile (inset).

When the operation wavelength is close to the dispersion resonance of the Bragg fiber, the laser delivers long pulses with narrow spectra. Figure 4-3 depicts an example of output pulse characteristics obtained for operation near the resonance wavelength. Indeed, the autocorrelation pulse duration is now 51 ps. Assuming a deconvolution factor of 1.41, corresponding to a Gaussian pulse shape, the pulse duration is then 28.4 ps. The optical spectrum is centred at 1042.6 nm with a spectral width of 160 pm. The near field image of the output beam exhibits a specific distribution with a star-like central part surrounded by eight petals lying in the first ring. This corresponds to the typical distribution of the supermode resulting from coupling between the fundamental mode (LP_{01}) of the core and the LP_{81} mode of the first ring indicating that this mode-locking regime arises around the resonance wavelength.

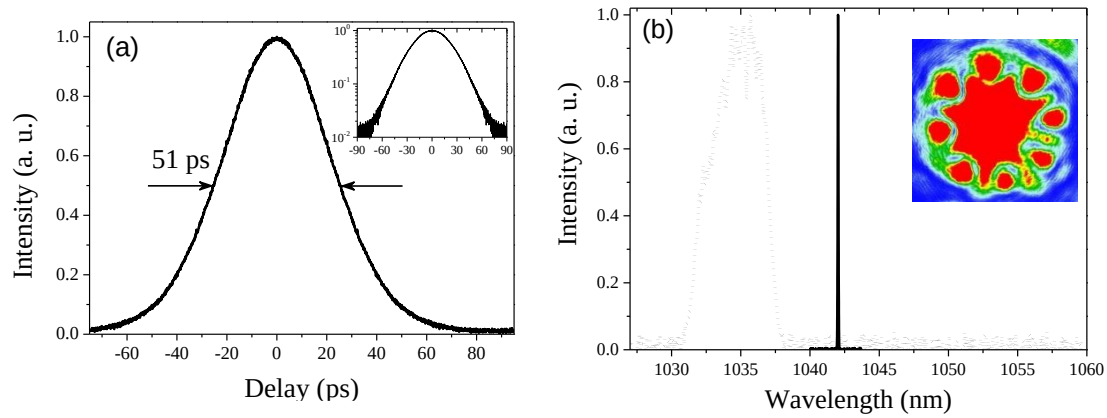

Figure 4-3 Laser outputs for fiber operation near dispersion resonance: (a) AC trace in linear and logarithmic (inset) scales; (b) optical spectrum and near field image of the output beam profile (inset). The dotted curve corresponds to the spectrum obtained far from resonance.

We note that pulse duration and spectral width are in agreement with the simulations of Section

2.5 when assuming a high normal dispersion active fiber.

The output power delivered in this regime increases monotonically with pump power to reach 520 mW (see Figure 4-4). At a repetition rate of 25 MHz, this corresponds to an energy per pulse of more t。han 20 nJ. We note that the highest energy level measured in the long pulse regime is 30nJ with pulses of about 50 ps duration. As predicted numerically in Chapter 2, pulse duration increases monotonically with pump power.

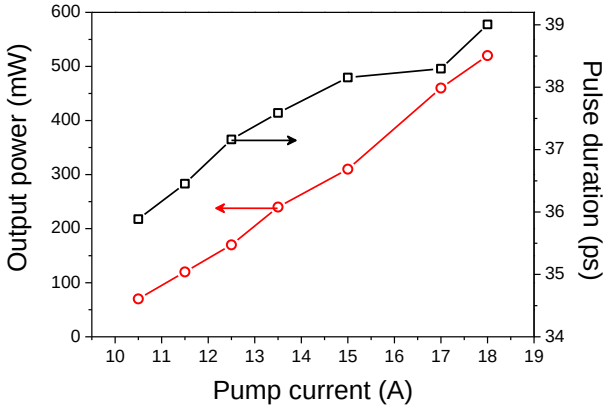

Figure 4-4 Output power and pulse duration evolution versus pump power in the long pulse regime.

We also analysed the evolution of the properties of the long pulse regime when tuning the wavelength near resonance. When starting from the longest pulse regime, wavelength shifting induce pulse shortening and a small spectral broadening. This is accompanied by an increase of the contrast of the central part of the beam compared to the petal-like part lying in the ring. The results depicted in Figure 4-5 illustrate quite well this behavior. The regime shown in Figure 4-5 (a) and (c) corresponds to the longest pulse duration measured in this laser configuration. We note that these experiments have been conducted using another segment of the Bragg fiber spool thus leading to a different resonance wavelength than previously. When the operation wavelength is centered at 1047.6 nm, the laser delivers a train of pulses with 51 ps duration and 92 pm spectral width. Using a pinhole to select only the central part of the beam, we measured its power content to be 70 mW for a total power of 330 mW. This measurement is in agreement with the beam profile image which confirms that the petal-like part content is comparable to that of the central region.

By adjusting the polarization elements, we can shift the emission wavelength to a longer wavelength around 1048.1 nm. We then observe a strong pulse shortening to 22.6 ps duration along with non-negligible spectral broadening (see Figure 4-5(c) and (d)). The near-field image of the output beam shows that the ring mode content is much lower than in the first case. This is confirmed by power measurements using the same pinhole to select the central part of the beam. Indeed, the measured power after spatial filtering is 170 mW for a total output power of 275 mW. We can conclude that when the wavelength approaches 1047.6 nm, the mode-coupling

between the core and the ring is at maximum and so is the the corresponding dispersion value, a condition which leads to long pulse operation. When we moved away from the resonance wavelength, the coupling decreases as well as the corresponding dispersion, and the mode-locked operation is under shorter pulses regime with broader spectra.

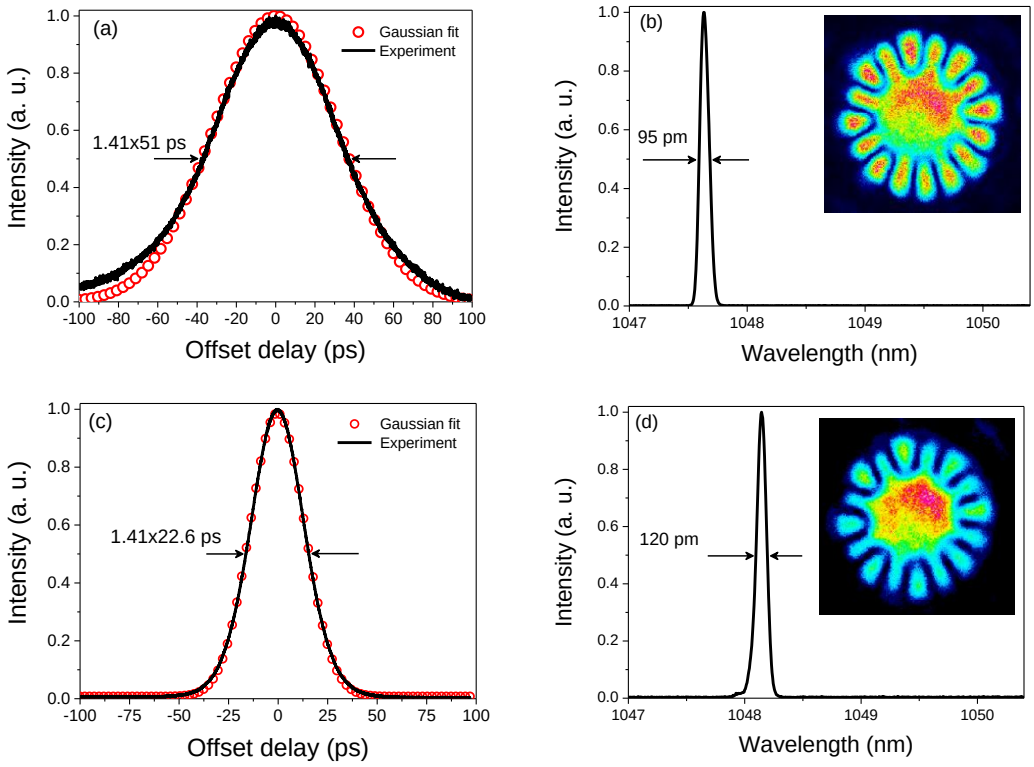

Figure 4-5 : Autocorrelation traces and optical spectra recorded for laser operation at the resonance wavelength (a-b) and for a small detuning from resonance (c-d).

In this section, we have demonstrated that the Bragg fiber laser can operate in two mode-locking regimes. The first type features short pulses with relatively broad spectra of several nanometers width and the second operation mode corresponds to the emission of long pulses with very narrow spectra of much less than 1 nm widths. The analysis of their spatial distribution confirms that the long pulse regimes arise at specific wavelengths where mode coupling between the core and the ring is strong. They are thus associated to high dispersion operation of the gain fiber as expected from simulations. To characterize more deeply the output beam profile generated near resonance, we developed an interferometric set-up to characterize the coherence between the different parts of the beam. This study is described in next section.

4.2 Spatial beam characterization

To experimentally verify that the spatial distribution measured near resonance corresponds to a

single super-mode structure resulting from mode coupling between the core and the ring, we build the Michelson interferometer setup shown in Figure 4-6. Such technique has been already used to characterize the spatio-temporal distortions of a high-energy solid-state laser [86]. The collimated beam generated by the laser is separated in two arms by the 50/50 beam splitter. The two beams are reflected back toward the beamsplitter which then combines their amplitudes. A curved mirror was used to magnify the beam from one arm of the interferometer thus leading to an interference pattern between the whole super-mode structure and its central component. The wave-fronts collected by the beam profiler were transferred to the computer for further process and recording. Clear interference patterns could be observed by fine adjustment of the mirrors positions to equalize the length paths of the two arms.

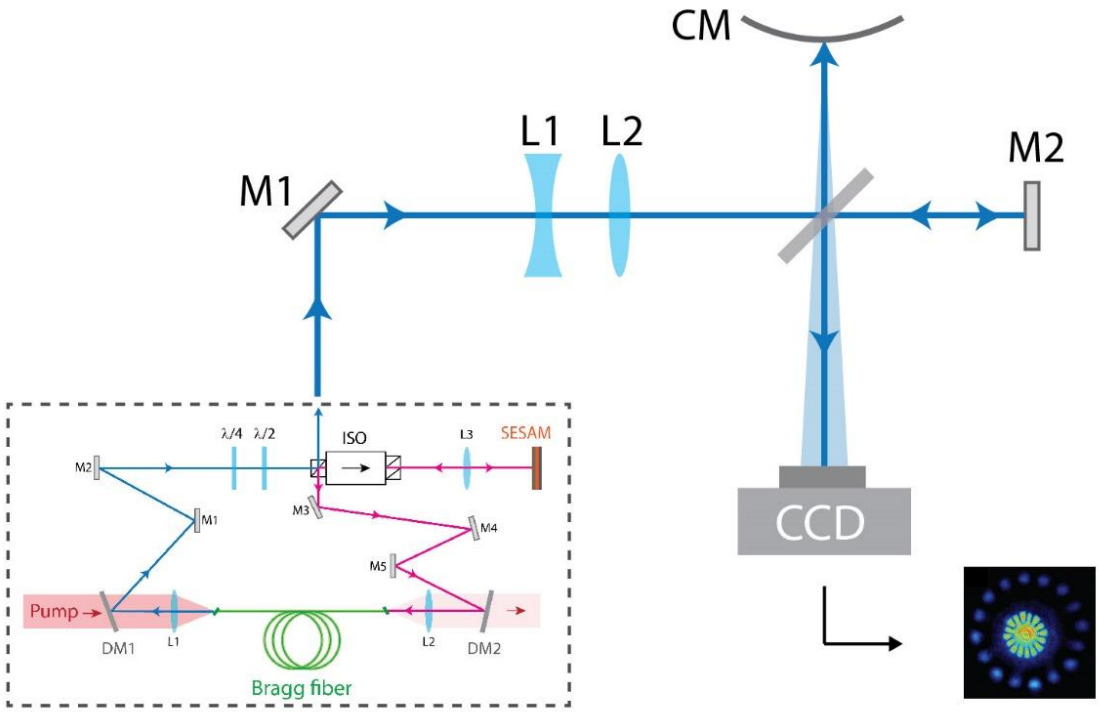

Figure 4-6 : Schematic diagram of the interferometric measurement system.

The laser beam profiles observed in the long pulse regime from each individual arm and the interferogram are shown in Figure 4-7. From the left to the right are the profiles of the beams reflected by the flat mirror, the curved mirror and that of their interferogram. The beam from the curved mirror had an enlarged wave front which interferes both the ring and core part of the beam reflected by the flat mirror with only its core part. From the interferogram of Figure 4-7(c), it appears that the laser beam shares the same radial phase all along its spatial distribution and presents a constant interference contrast.

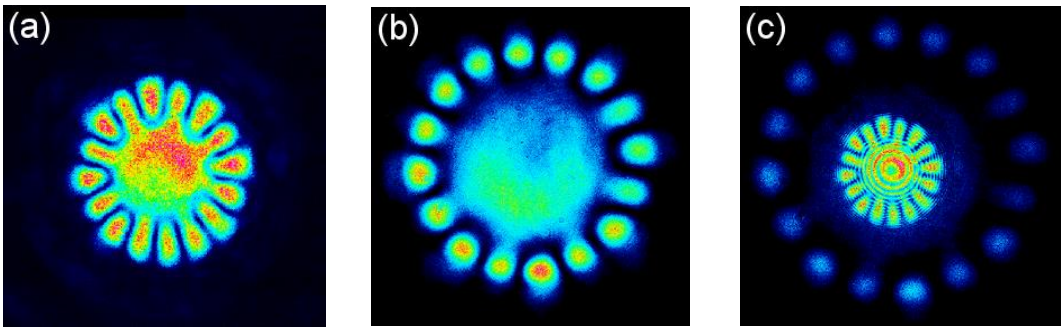

Figure 4-7 : Beam profile recorded from (a) the flat mirror arm, (b) the curved mirror arm and (c) the interference pattern resulting from both arms.

One may conclude from the results above that the spatial distribution of our laser corresponds to a single compound entity resulting from the strong coupling between the core mode and one ring mode. The phase shift between the successive petals of the ring mode revealed by our measurements suggests that this mode is indeed a combination of two component modes. To confirm our assumption, we studied the different spatial distributions able to reproduce the measured inteferogram.

From the axial symmetry nature of the fiber and the actual beam profile, it is straightforward to assume that the super mode is a combination of a core mode of Gaussian beam and a ring mode consisting of two Laguerre-Gaussian modes.

The Laguerre-Gaussian beam mode is proposed to modal decompose the beam profile because of the circularly symmetric boundary conditions of which the Bragg fiber is one example. The mathematical modeling of such beams is well studied in the work reported in [87]. The simulated intensity profile of LG_{08} is shown in Figure 4-8(a). It is the same for the $LG_{0(-8)}$ mode because they are indistinguishable under intensity profiling. The difference of the two modes is that their angular phases increase from 0 to 16π clockwise or anticlockwise respectively. So, the superposition of these two modes causes interferences between them and the simulated intensity profile is shown in Figure 4-8(b).

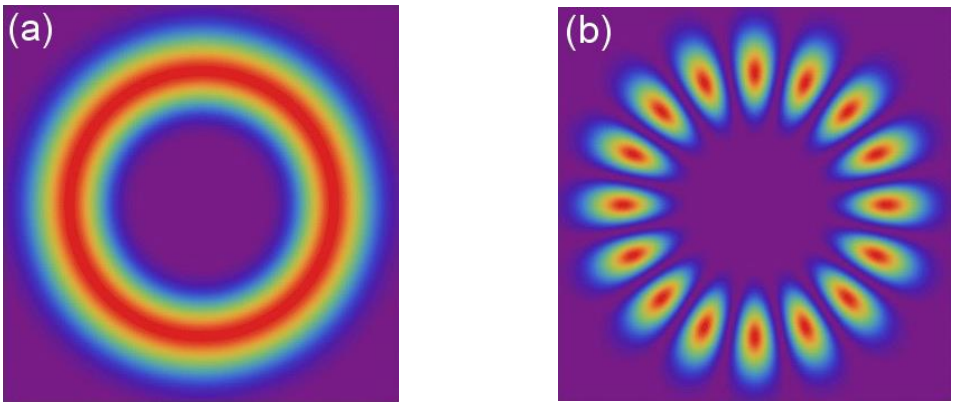

Figure 4-8: Simulated intensity profiles of an LG_{08} mode (a) and a superposition of a LG_{08} and $LG_{0(-8)}$ modes.

If we consider the combination of 3 mutually phase-matched components consisting in two LG modes and a Gaussian beam for the core mode, we can reconstruct very accurately the spatial beam profile. Figure 4-9 shows the simulated intensity profile of the beam along with the experimental one collected by the beam profiler. The dots of the petal-like structure have alternating connection to and isolation with the central part, phenomenon which is caused by the interference between these three modes. As explained previously the LG mode has an angular phase distribution while the phase of Gaussian mode is angular-invariant. Compared with the simulated profile, the experimental one has a larger core with flatter energy distribution. This is a result of the bending to the Bragg fiber and the fact that the fundamental mode profile which is more flat-topped than an ideal Gaussian profile, as already discussed in [59].

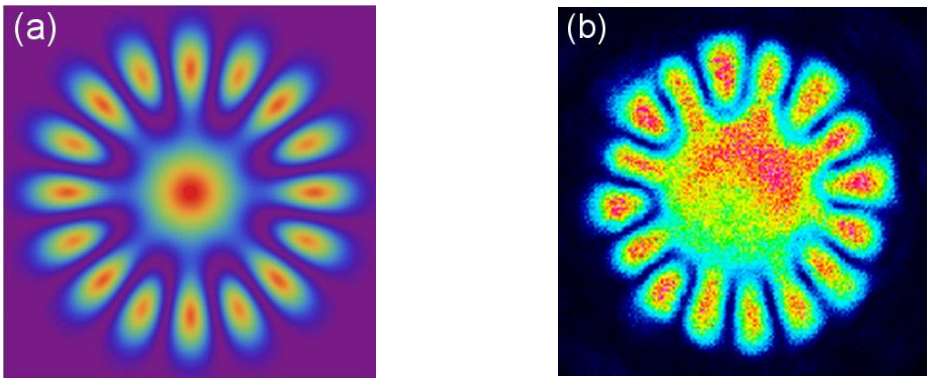

Figure 4-9 (a) beam profile from simulation and (b) actual beam profile

Now that we are able to reproduce the beam structure let us turn back to the interferogram to see if the same modal distribution can still reproduce a result comparable to experiments.
Figure 4-10 shows the zoomed-in interferogram previously shown in Figure 4-7(c) along with the simulated intensity profile. One can see that the simulated interferogram coincides in detail with the experimental one. In particular, the phase shift alternation expected for the consecutive petals is indeed verified experimentally, see indicated by dotted red lines in Figure 4-10.

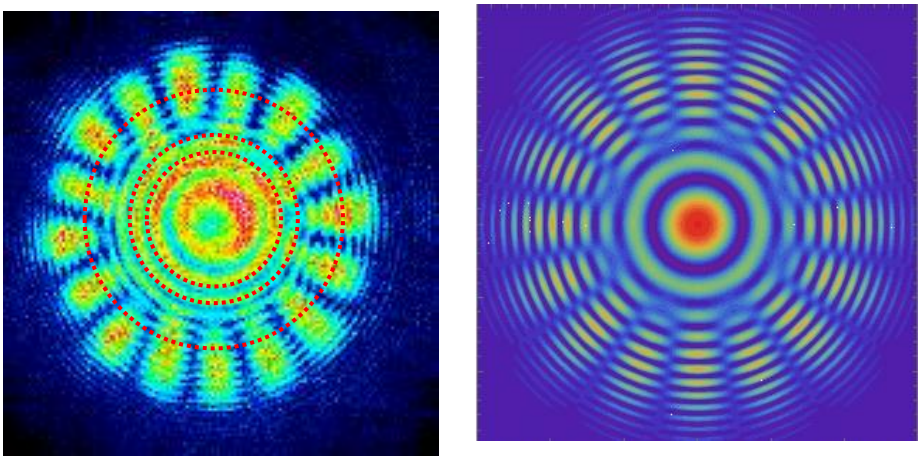

(a) (b)

Figure 4-10 (a) Measured and (b) reconstructed interference pattern resulting from the combination

of the output beam with its central part.

Our simple modal decomposition method is a good approximation for the observed beam structure. It suggests that the generated beam results from a combination of LG-type beams with angular momentum and a quasi-Gaussian beam. More investigations are needed to characterize all the features of our laser. In particular, if our expectations are verified using a phase modulator such as SLMs it would be possible to separate the two LG modes and verify their order by converting them back to Gaussian beams. Such experiments are undergoing in our laboratory and should provide further insights into the potential of the Bragg fiber.
However, our results confirm the numerical predictions concerning the difficulty to generate short pulses using Bragg-fiber lasers operating near resonance because of the mode-coupling between the core and the ring region which limits the high-dispersion bandwidth. One solution consists to use W-type fibers which exhibit broader bandwidth at the expense of lower dispersion. The next section then discusses the results obtained with a specifically designed fiber.

4.3 Mode-locked W-type fiber laser

In this section, we discuss the experimental results obtained using an active fiber exhibiting a W-type index profile and sharing the same principle of dispersion enhancement than Bragg-fibers but requiring simpler manufacturing processes and featuring broader operation bandwidth as discussed in Chapter 2.

4.3.1 Fiber design and dispersion properties:

The fibre used in this work has been designed at XLIM Laboratory and fabricated at the Fiber Optics Research Center (FORC) of Moscow. The index profile of the fabricated fibre is shown in Figure 4-11. It consists in a high-index erbium-doped core with about 6 µm diameter surrounded by a 5 µm thick high-index ring layer located 15 µm from the fibre axis. The index contrasts of the core and ring regions relatively to the silica cladding are 0.011 and 0.003, respectively. The fibre preform has been drawn at different outer diameters ranging from 105 to 130 µm with 5 µm step to match the dispersion curve with the emission bandwidth of erbium ions. First, the dispersion curve of the fibre has been measured using a segment of the 105 µm outer diameter fibre. The results are shown on Figure 4-11(b).

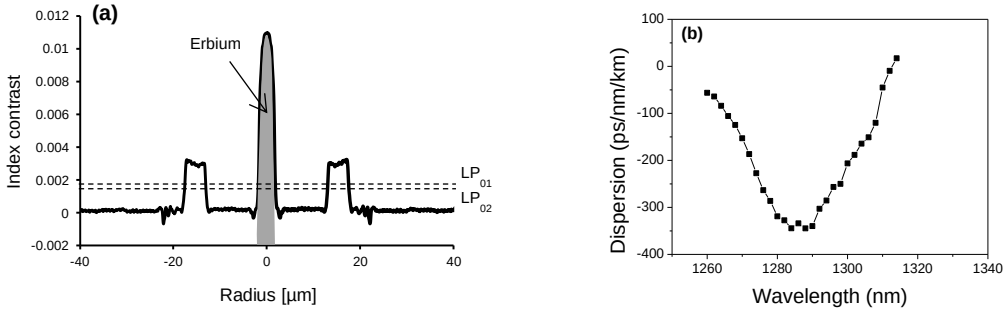

Figure 4-11 (a) Index profile and (b) dispersion curve of the erbium-doped W-type fibre.

Starting from the experimental index profile and the measured dispersion curve, it has been shown that an outer diameter of 125 µm should allow to match the emission band of Erbium ions. Figure 4-12 shows the calculated dispersion curve of the two guided modes (LP_{01} and LP_{02}) for an outer diameter of 125 µm. This has been confirmed experimentally by optical low-coherence interferometry (OLCI) measurements done at Telecom-Paristech [88]. The measured dispersion value of the LP_{01} mode is -80 ps/nm/km at 1550 nm. Unfortunately, this value is much lower than the maximum dispersion expected with this fibre design. Moreover, the mode area of the fundamental mode is only 30 μm^2. Nevertheless, this fibre constitutes a good sample for concept validation.

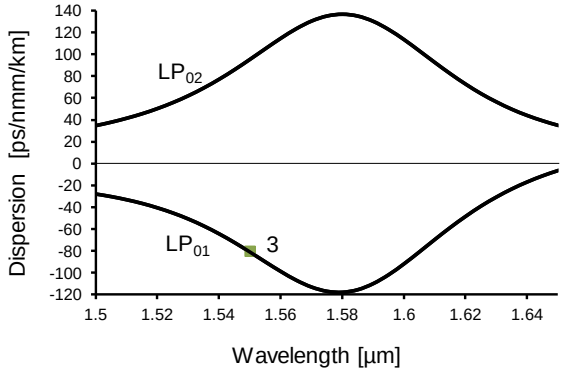

Figure 4-12 Calculated dispersion curves of the two guided modes and measured value for the LP01.

4.3.2 Experimental setup and results:

The laser system studied in this section is schematically depicted in Figure 4-13. As in the first section, the oscillator is built in a σ-cavity configuration using a polarization sensitive isolator as a circulator to include the saturable absorber mirror (SAM) in the linear part of the cavity. A set of quarter- and half-wave plates are employed to adjust the beam polarization to tailor the cavity losses and to take advantage of the NPE effect because the small core area introduces high non-linearity which enables NPE to reinforce the mode-locking mechanism. The cavity

includes 9 meters of high-dispersion erbium-doped W-fiber with a dispersion of -80 ps/km/nm at 1550 nm and 23 dB/m pump absorption at 980 nm. The gain fiber is core-pumped by a fiber-coupled diode emitting at 980 nm, through a single mode wavelength division multiplexer. The 1 m long WDM fiber presents a dispersion of +8.6 ps/nm/km. A fiber output coupler is used to extract 90% of the energy out of the cavity. It consists in a 2 m long single mode fiber with +14 ps/nm/km dispersion at 1550nm. The laser output is connected to a polarization insensitive isolator to avoid any parasitic feedback which can disturb its operation. A fraction (30%) of the laser output is used to monitor the output signal and confirm the mode-locking operation. The other 70% output is sent to the final stage consisting of an erbium-doped fiber amplifier (EDFA), a piece of 20 m of dispersion compensated fiber (DCF) and a gratings-based compressor. The EDFA amplifies the output pulses prior to their nonlinear compression by the combined actions of the DCF and the bulk-compressor.

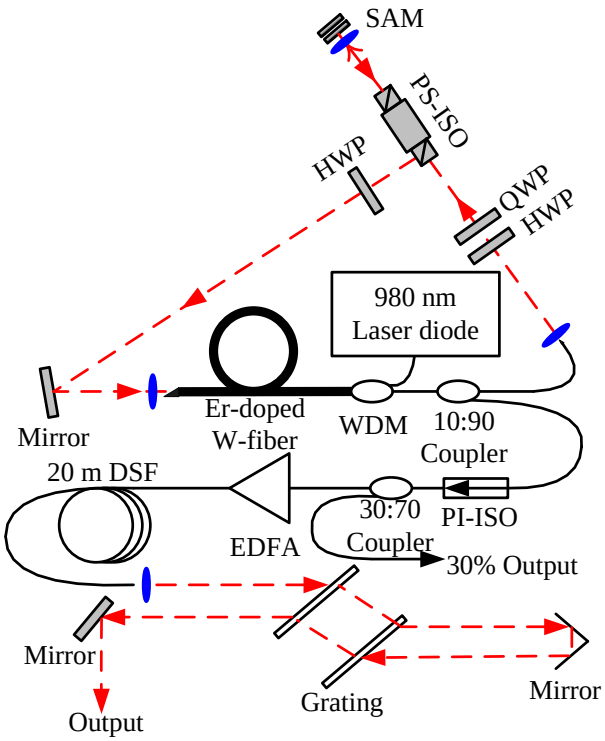

Figure 4-13 Schematic of the passively mode-locked fiber laser: HWP, half-wave plate; QWP, quarter-wave plate; SAM, saturable absorber mirror; WDM, wavelength division multiplexer, PI-ISO polarization independent isolator; EDFA, Er-doped fiber amplifier; DSF, dispersion shifted fiber.

With the saturation criteria of the SAM met and the waveplates properly adjusted, stable passive mode-locking can be achieved. The pulse characteristics of a typical mode-locked regime are shown in Figure 4-14. The single pulse operation is confirmed by a fast oscilloscope together with large span auto-correlation measurements. The AC trace is best fitted assuming a Gaussian pulse shape with 29 ps duration. The optical spectrum is centered at 1532.4 nm with 0.17 nm

width which corresponds to a Fourier limited pulse duration of about 20 ps. This suggests that the output pulse suffers from a relatively low chirp.

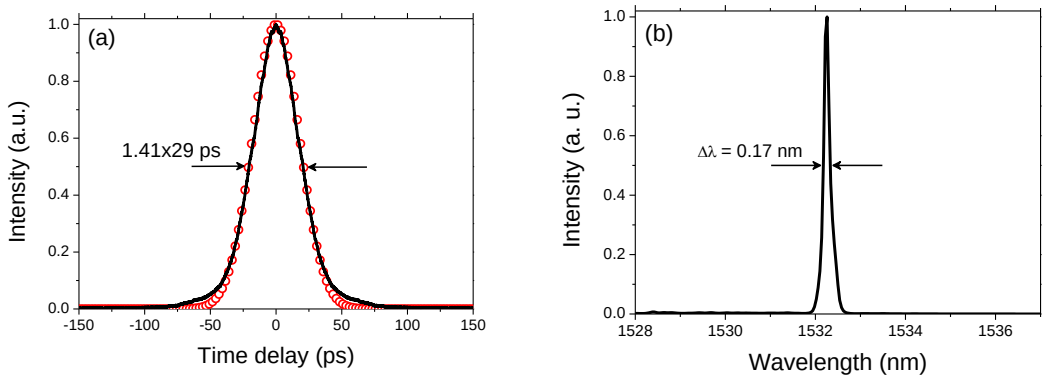

Figure 4-14 Characteristics of the typical mode-locking regime delivered by the erbium-doped W-fiber laser : (a) auto correlation trace and (b) optical spectrum.

Similar regimes have been obtained at different central wavelengths in the range 1527 to 1535 nm by changing the focalisation conditions on the SAM or by adjusting the polarisation settings. The oscillator delivers an average power of about 125 mW at 12 MHz repetition rate corresponding to more than 10 nJ energy. To check the temporal coherence of the generated pulses, the output signal is amplified and then injected inside a non-zero dispersion fibre featuring a low normal dispersion at 1550 nm. Using a 20-m long segment of this fibre, the spectrum is broadened through self-phase modulation. Using a pair of transmission gratings with 1000 lines/mm, the spectrally broadened pulses are dechirped close to their theoretical limit.

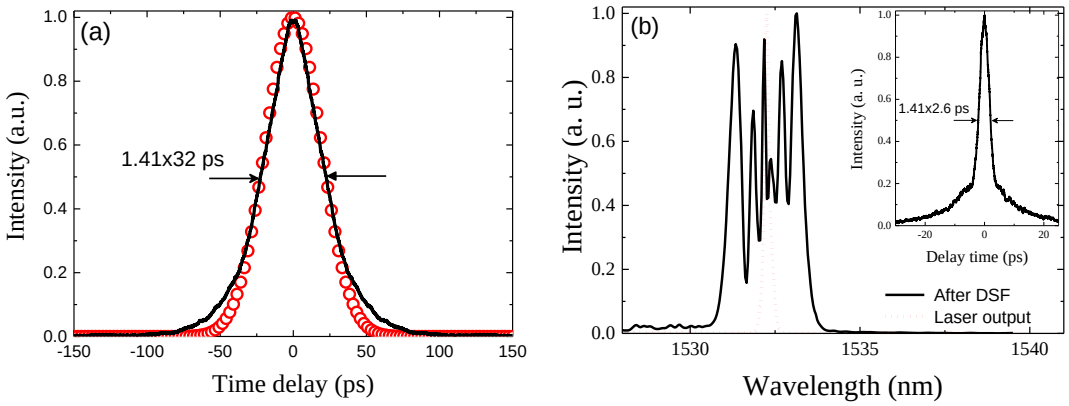

Figure 4-15 (a) AC trace and (b) spectrum of the pulse directly measured from the output port of DCF. Inset of (b): AC trace measured after compression by the gratings pair.

Figure 4-15 shows the AC trace and the spectrum measured after propagation inside the DSF fiber. The output pulse is stretched to 32 ps after propagation in the DSF and its shape starts to deviate from a Gaussian profile. Comparing the output from the DSF with that from the output coupler, it can be confirmed that the output pulses are highly coherent instead of being noise-like. The spectrum is broadened from 0.17 nm to about 3 nm mainly due to self-phase

modulation. By optimizing the gratings distance the output pulses are compressed to 2.6 ps duration which is close to the Fourier limit when assuming a squared spectral shape.
It is demonstrated so far that the fiber could be used to build a mode-locked oscillator which produces highly chirped pulse with ultra-narrow spectrum. The coherence of its output is confirmed by nonlinear compression outside the cavity.

4.4 Conclusion

In this Chapter, we presented and discussed the experimental implementation of mode-locked lasers operating at high normal dispersions and based on two kinds of specific active fibers, namely an Yb-doped Bragg fiber and an Er-doped W-type fiber.
First, concerning the Bragg fiber laser, two distinct operation regimes have been identified, as predicted by the simulations in Chapter 2. These regimes indeed strongly differ in terms of pulse duration and spectral bandwidth but also in their modal content. Far from resonance, short pulses and typical broad spectra are observed, with most of the energy located in the central core, as previously reported in the literature. Close to the resonance, however, the mode-locked laser produces long pulses corresponding to a specific spatial distribution, thereby proving operation at high normal dispersion despite a relatively narrow high-dispersion bandwidth. Detailed spatial characterization of this mode confirmed our expectations and moreover suggested that it results from the superposition of two Laguerre-Gaussian-type modes. More work is now needed to experimentally separate these modes carrying orbital angular momentum, with a wide range of potential applications in communications and metrology.
Secondly, we expected the possibility to use W-type fibers which can lead to broader high-dispersion bandwidths and thus higher performances. Even if the manufactured fiber did not reach its maximum available dispersion, this study has permitted to validate the general concept. Using this configuration, we indeed managed to produce highly-chirped coherent pulses with narrow spectra, which means that much better performances can now be reached with adequate design and manufacturing of this specific fiber. We thus believe that these two studies open up new ways of future research using such high-dispersion architectures.

Conclusion and discussion

This dissertation is devoted to the study and development of mode-locked fiber lasers operating at high normal dispersion, especially for their energy scaling capability. We mainly exploited two methods to achieve high normal dispersion inside the cavity: the first one relied on adding segments of passive dispersion compensating fiber to build CPO lasers with high pulse energy, and the second one was based on specialty active fibers which have wavelength-dependent ultra-high normal dispersion due to mode coupling and resonance phenomena. The former study led to the development of a dissipative soliton laser delivering the highest pulse energy under similar configurations to our best knowledge, which now serves as a reliable platform for other studies of our group. The later study yielded a lot of attractive, although preliminary results and urges for more works into this direction.

The dissipative soliton laser based on the CPO method with conventional passive component (DCF) is introduced and discussed in Chapter 3. The corresponding numerical simulations indicate that a strong intra-cavity pulse shaping mechanisms are required to reach higher energy levels in such high-dispersion oscillators. It is worth mentioning that the simulation predicted that pulses with very high energy (up to 190 nJ) could be generated with very high normal dispersion i.e., very long DCF added inside the cavity through quasi-parabolic pulse evolution. The possibility for such mode-locking regimes to start from quantum noise is however compromised since the stable solutions are reached only when calculations are started from a "seed pulse", which is hardly the case in our passively mode-locked laser configuration. The combination of a high-contrast amplitude modulator with a narrow bandwidth spectral filter constitute a good solution to ensure self-starting operation even if such configurations can support also multiple-pulse solutions.

Most of the numerical predictions have been experimentally verified. Indeed, for moderate dispersion values our study show that an amplitude modulator is enough to start and stabilize mode-locking. By increasing the intra-cavity dispersion to more than +0.5 ps^2, the addition of a narrow spectral filter is necessary to stabilize the pulsed regimes. For 1.22 ps^2 averaged cavity dispersion obtained by insertion of 10-m of DCF inside the cavity, the developed laser delivers highly stable train of pulses with 22 nJ energy and 8.8 ps duration which can be linearly dechirped close to their Fourier limit. The output pulses exhibit a typical M-shaped spectrum as predicted by simulations. Further increasing the length of DCF resulted in higher pulse energy levels which reached 38 nJ for 15 m of DCF, which is to our best knowledge the highest level under similar laser configuration. Finally, it became difficult to get stable mode-locking when longer DCF were used, as the dissipative and pulse shaping mechanisms could not

compensate the large nonlinear phase cumulated along the cavity. Noise measurements based on radiofrequency analysis confirmed that the developed oscillator features an excellent amplitude stability with a RIN level of -150 dBc/Hz, which make it suitable to serve as a platform for various applications. We then exploited it to pump a fiber optical parametric oscillator where its tunable highly-chirped output pulses allowed efficient frequency conversion to the spectral region around 1700 nm, which is attractive for biomedical imaging.

The second approach studied in this thesis consisted in building mode-locked lasers featuring high-dispersion active fiber such as Bragg or W-type fibers. In this case, the active fiber itself provides high normal dispersion via mode-coupling effects. It is then demonstrated that using Bragg fibers allows a rapidly-changing dispersion with extremely high peak value in a narrow wavelength bandwidth, which however indicates that pulses with large spectral bandwidths could be difficult to achieve and that strong effects from higher order dispersion should be expected. The numerical simulations predicted a bifurcating behavior of pulse dynamics: far from the mode-coupling resonance wavelength, the laser produces pulses in the fundamental core mode, and exhibits limited energy scaling capability mainly due to its LMA nature. Nevertheless, in the vicinity of the resonance wavelength, due to the high dispersion introduced by mode-coupling, the pulse is stretched fast enough to avoid being destabilized by wave-breaking effects and thus raise the energy scaling limit. Gain bandwidth filtering, together with the SESAM serves as the main intracavity pulse shaping mechanisms which guarantees the pulse self-consistency. The mode-coupling effect also causes more energy to be coupled into the ring mode and thus increases the MFD. Both regimes have then been successfully observed experimentally in Chapter 4, with particular beam profiles proving the shifting between both regimes. On the one hand, the energy scaling capability of the resonance operation regimes are however not as high as expected by the simulation mainly due to two reasons: the degraded quality of the Bragg fiber from its manufacturing process and a resonance bandwidth which is narrower than in the simulations, which prevents a pulse with broader spectrum to be produced and thus prohibits higher pulse energy.

On the other hand, spatial beam characterization based on self-interference of the Bragg fiber laser output yielded very interesting outcomes. First, the interferogram of the actual beam coincides well with the simulation where it is assumed that the ring mode is the superposition of two LG modes. It now requires more work to characterize and even separate these modes. Once proved, it would be the first report of beams with orbital angular momentum (OAM) directly generated in a mode-locked fiber laser, and may find many applications [89] in communications [90] and optical manipulations [91][92] etc.

In order to reach a better energy scaling potential, we then replaced the Bragg active fiber with a W-type active fiber, which could provide high dispersions through the same process as

previously, but with a broadened high dispersion bandwidth at the expense of lower peak value. The experimental results were not completely satisfying but nevertheless confirmed the potential of producing highly chirped pulsed with comparatively broader spectrum. The main problem of this approach to high energy is the small-core nature of this fiber which is against its energy scaling potential because it leads to stronger nonlinear effects from which high energy pulses could suffer. The manufacture and design of such W-fiber for energy scaling in mode-locked lasers still have room for improvement, and more experimental works are needed to make it a competitive technique.

The aim of the work presented in this PhD thesis was to demonstrate that mode-locked ultrafast fiber lasers based on cavities with very high normal dispersions present a strong potential for energy scaling. The numerical and experimental results obtained for oscillators either based on passive components with high dispersions (DCF) or custom-designed specialty active fiber featuring giant dispersion through mode-coupling processes indeed validated this concept while highlighting its potentialities and limitations. In the frame of the development of high energy fiber lasers, we believe that this study now paves the way for thorough investigations in the use of active fibers with specific geometries favoring high normal dispersion.

This page is intentionally left blank

References

[1] F. Stutzki, F. Jansen, H-J. Otto, C. Jauregui, J. Limpert, and A. Tünnermann, "Designing advanced very-large-mode-area fibers for power scaling of fiber-laser systems," *Optica* 1, 233-242 (2014)
[2] C. Jauregui, J. Limpert, A. tünnermann, High power fiber lasers, *Nature Photonics* 7, 861–867 (2013)
[3] T. Eidam, S. Hanf, E. Seise, T. V. Andersen, T. Gabler, C. Wirth, T. Schreiber, J. Limpert, A. Tünnermann, "Femtosecond fiber CPA system emitting 830 W average output power," *Opt. Lett.* 35, 94 (2010)
[4] F. Röser, T. Eidam, J. Rothhardt, O. Schmidt, D. N. Schimpf, J. Limpert, and A. Tünnermann, "Millijoule pulse energy high repetition rate femtosecond fiber chirped-pulse amplification system," *Opt. Lett.* 32, 3495-3497 (2007)
[5] M. Kienel, M. Müller, A. Klenke, J. Limpert, and A. Tünnermann, "12 mJ kW-class ultrafast fiber laser system using multidimensional coherent pulse addition," *Opt. Lett.* 41, 3343-3346 (2016)
[6] F. Guichard, Y. Zaouter, M. Hanna, K-L. Mai, F. Morin, C. Hönninger, E. Mottay, and P. Georges, "High-energy chirped- and divided-pulse Sagnac femtosecond fiber amplifier," *Opt. Lett.* 40, 89-92 (2015)
[7] S. Zhou, F. W. Wise, and D. G. Ouzounov, "Divided-pulse amplification of ultrashort pulses," *Opt. Lett.* 32(7), 871–873 (2007)
[8] A. Baz, L. Bigot, G. Bouwmans, and Y. Quiquempois, "Single-Mode, Large Mode Area, Solid-Core Photonic BandGap Fiber With Hetero-Structured Cladding," *J. Lightwave Technol.* 31, 830-835 (2013)
[9] C. B. Olausson, A. Shirakawa, M. Chen, J. K. Lyngsø, J. Broeng, K. P. Hansen, A. Bjarklev, and K. Ueda, "167 W, power scalable ytterbium-doped photonic bandgap fiber amplifier at 1178nm," *Opt. Express* 18, 16345-16352 (2010)
[10] D. A. Gaponov, S. Février, M. Devautour, P. Roy, M. E. Likhachev, S. S. Aleshkina, M. Y. Salganskii, M. V. Yashkov, and A. N. Guryanov, "Management of the high-order mode content in large (40 μm) core photonic bandgap Bragg fiber laser," *Opt. Lett.* 35, 2233-2235 (2010)
[11] K. Peng, H. Zhan, L. Ni, X. Wang, Y. Wang, C. Gao, Y. Li, J. Wang, F. Jing, A. Lin, "Single-mode large-mode-area laser fiber with ultralow numerical aperture and high beam quality," *Appl. Opt.* 55, 10133-10137 (2016)
[12] Nicholson, Jeff. "Higher-order-mode fiber amplifiers." *Applications of Lasers for Sensing and Free Space Communications*. Optical Society of America, 2010.
[13] H. Song, B. Liu, Y. Li, Y. Song, H. He, L. Chai, M. Hu, and C. Wang, "Practical 24-fs, 1-μJ, 1-MHz Yb-fiber laser amplification system," *Opt. Express* 25, 7559-7566 (2017)
[14] Y. Deng, C-Y. Chien, B. G. Fidric, and J. D. Kafka, "Generation of sub-50 fs pulses from a high-power Yb-doped fiber amplifier," *Opt. Lett.* 34, 3469-3471 (2009)
[15] Chong, Andy, William H. Renninger, and Frank W. Wise. "Properties of normal-dispersion femtosecond fiber lasers." *JOSA B* 25.2 (2008): 140-148.
[16] Chong, Andy, William H. Renninger, and Frank W. Wise. "All-normal-dispersion femtosecond fiber laser with pulse energy above 20nJ." *Optics letters* 32.16 (2007): 2408-

2410.
[17] M. Baumgartl, C. Lecaplain, A. Hideur, J. Limpert, and A. Tünnermann, "66 W average power from a microjoule-class sub-100 fs fiber oscillator," *Opt. Lett. 37*, 1640-1642 (2012)
[18] R. W. Boyd, *Nonlinear optics* (Academic press, 2003)
[19] G. P. Agrawal, *Nonlinear fiber optics* (Academic press, 2007).
[20] Shen, Yuen-Ron. "The principles of nonlinear optics." *New York, Wiley-Interscience, 1984, 575 p.* 1 (1984).
[21] Drever, R. W. P., Hall, J. L., Kowalski, F. V., Hough, J., Ford, G. M., Munley, A. J., & Ward, H. "Laser phase and frequency stabilization using an optical resonator." *Applied Physics B* 31.2 (1983): 97-105.
[22] Bulushev, A. G., Eugene M. Dianov, and O. G. Okhotnikov. "Passive mode locking of a laser with a nonlinear fiber reflector." *Optics letters* 15.17 (1990): 968-970.
[23] Ippen, Erich P., Hermann A. Haus, and L. Y. Liu. "Additive pulse mode locking." *JOSA B* 6.9 (1989): 1736-1745.
[24] Siegman, Anthony E. "Lasers university science books." *Mill Valley, CA* 37 (1986): 462-466.
[25] Fang, Li. *Development of ultrafast saturable absorber mirrors for applications to ultrahigh speed optical signal processing and to ultrashort laser pulse generation at 1.55 μm*. Diss. Paris 11, 2014.
[26] Akhmediev, Nail N., and Adrian Ankiewicz. *Solitons: nonlinear pulses and beams*. Chapman & Hall, 1997.
[27] Kuznetsov, E. A. "Solitons in a parametrically unstable plasma." *Akademiia Nauk SSSR Doklady*. Vol. 236. 1977.
[28] Peregrine, D. H. "Water waves, nonlinear Schrödinger equations and their solutions." *The Journal of the Australian Mathematical Society. Series B. Applied Mathematics* 25.01 (1983): 16-43.
[29] Dudley, J. M., Dias, F., Erkintalo, M., & Genty, G. "Instabilities, breathers and rogue waves in optics." *Nature Photonics* 8.10 (2014): 755-764.
[30] Mollenauer, Linn F., Roger H. Stolen, and James P. Gordon. "Experimental observation of picosecond pulse narrowing and solitons in optical fibers." *Physical Review Letters* 45.13 (1980): 1095.
[31] Mollenauer, Linn F., and Roger H. Stolen. "The soliton laser." *Optics letters* 9.1 (1984): 13-15.
[32] Anderson, D., Desaix, M., Karlsson, M., Lisak, M., & Quiroga-Teixeiro, M. L. "Wave-breaking-free pulses in nonlinear-optical fibers." *JOSA B* 10.7 (1993): 1185-1190.
[33] Tamura, K., and M. Nakazawa. "Pulse compression by nonlinear pulse evolution with reduced optical wave breaking in erbium-doped fiber amplifiers." *Optics letters* 21.1 (1996): 68-70.
[34] Ilday, F. Ö., Buckley, J. R., Clark, W. G., & Wise, F. W. "Self-similar evolution of parabolic pulses in a laser." *Physical review letters* 92.21 (2004): 213902.
[35] Ruehl, A., Prochnow, O., Wandt, D., Kracht, D., Burgoyne, B., Godbout, N., & Lacroix, S. "Dynamics of parabolic pulses in an ultrafast fiber laser." *Optics letters* 31.18 (2006): 2734-2736.
[36] Oktem, Bulent, Coşkun Ülgüdür, and F. Ömer Ilday. "Soliton–similariton fibre laser." *Nature Photonics* 4.5 (2010): 307-311.
[37] Herda, Robert, and Oleg G. Okhotnikov. "Dispersion compensation-free fiber laser mode-locked and stabilized by high-contrast saturable absorber mirror." *IEEE journal of*

quantum electronics 40.7 (2004): 893-899.
[38] Baumgartl, M., Ortaç, B., Limpert, J., & Tünnermann, A. "Impact of dispersion on pulse dynamics in chirped-pulse fiber lasers." *Applied Physics B* 107.2 (2012): 263-274.
[39] Kobtsev, Sergey, Sergey Kukarin, and Yurii Fedotov. "Ultra-low repetition rate mode-locked fiber laser with high-energy pulses." *Optics Express* 16.26 (2008): 21936-21941.
[40] Woodward, R. I., Kelleher, E. J. R., Popa, D., Hasan, T., Bonaccorso, F., Ferrari, A. C., ... & Taylor, J. R. "Scalar nanosecond pulse generation in a nanotube mode-locked environmentally stable fiber laser." *IEEE Photon. Technol. Lett* 26.16 (2014): 1672-1675.
[41] Zhao, L. M., D. Y. Tang, and J. Wu. "Gain-guided soliton in a positive group-dispersion fiber laser." *Optics letters* 31.12 (2006): 1788-1790.
[42] Lecaplain, C., Chédot, C., Hideur, A., Ortaç, B., & Limpert, J. "High-power all-normal-dispersion femtosecond pulse generation from a Yb-doped large-mode-area microstructure fiber laser." *Optics letters* 32.18 (2007): 2738-2740.
[43] Ortaç, B., Schmidt, O., Schreiber, T., Limpert, J., Tünnermann, A., & Hideur, A. "High-energy femtosecond Yb-doped dispersion compensation free fiber laser." *Optics express* 15.17 (2007): 10725-10732.
[44] Ortaç, B., Lecaplain, C., Hideur, A., Schreiber, T., Limpert, J., & Tünnermann, A. "Passively mode-locked single-polarization microstructure fiber laser." *Optics express* 16.3 (2008): 2122-2128.
[45] Lecaplain, C., Ortaç, B., Machinet, G., Boullet, J., Baumgartl, M., Schreiber, T., ... & Hideur, A. "High-energy femtosecond photonic crystal fiber laser." *Optics letters* 35.19 (2010): 3156-3158.
[46] Cabasse, A., Gaponov, D., Ndao, K., Khadour, A., Oudar, J. L., & Martel, G. "130 mW average power, 4.6 nJ pulse energy, 10.2 ps pulse duration from an Er^{3+} fiber oscillator passively mode locked by a resonant saturable absorber mirror." *Optics letters* 36.14 (2011): 2620-2622.
[47] Cabasse, A., G. Martel, and J. L. Oudar. "High power dissipative soliton in an Erbium-doped fiber laser mode-locked with a high modulation depth saturable absorber mirror." *Optics express* 17.12 (2009): 9537-9542.
[48] Chang, W., Ankiewicz, A., Soto-Crespo, J. M., & Akhmediev, N. "Dissipative soliton resonances." *Physical Review A* 78.2 (2008): 023830.
[49] Duan, L., Liu, X., Mao, D., Wang, L., & Wang, G. "Experimental observation of dissipative soliton resonance in an anomalous-dispersion fiber laser." *Optics express* 20.1 (2012): 265-270.
[50] Wu, X., Tang, D. Y., Zhang, H., & Zhao, L. M. "Dissipative soliton resonance in an all-normal-dispersion erbium-doped fiber laser." *Optics express* 17.7 (2009): 5580-5584.
[51] Li, D., Tang, D., Zhao, L., & Shen, D. "Mechanism of dissipative-soliton-resonance generation in passively mode-locked all-normal-dispersion fiber lasers." *Journal of Lightwave Technology* 33.18 (2015): 3781-3787.
[52] Zheng, X. W., Luo, Z. C., Liu, H., Zhao, N., Ning, Q. Y., Liu, M., ... & Xu, W. C. "High-energy noiselike rectangular pulse in a passively mode-locked figure-eight fiber laser." *Applied Physics Express* 7.4 (2014): 042701.
[53] Semaan, G., Niang, A., Salhi, M., & Sanchez, F. "Harmonic dissipative soliton resonance square pulses in an anomalous dispersion passively mode-locked fiber ring laser." *Laser Physics Letters* 14.5 (2017): 055401.
[54] Li, D., Li, L., Zhou, J., Zhao, L., Tang, D., & Shen, D. "Characterization and compression of dissipative-soliton-resonance pulses in fiber lasers." *Scientific reports* 6 (2016).
[55] Ramachandran, Siddharth. *Fiber based dispersion compensation*. Vol. 5. Springer

Science & Business Media, 2007.
[56] Schneider, V. M., and J. A. West. "Analysis of wideband dispersion slope compensating optical fibres by supermode theory." *Electronics Letters* 38.7 (2002): 306-307.
[57] Yeh, Pochi, Amnon Yariv, and Emanuel Marom. "Theory of Bragg fiber." *JOSA* 68.9 (1978): 1196-1201.
[58] Gérôme, F., Février, S., Pryamikov, A. D., Auguste, J. L., Jamier, R., Blondy, J. M., ... & Dianov, E. M. "Highly dispersive large mode area photonic bandgap fiber." *Optics letters* 32.10 (2007): 1208-1210.
[59] Février, S., Gaponov, D.D., Roy, P., Likhachev, M.E., Semjonov, S.L., Bubnov, M.M., Dianov, E.M., Yashkov, M.Y., Khopin, V.F., Salganskii, M.Y. and Guryanov, A.N. "High-power photonic-bandgap fiber laser." *Optics letters* 33.9 (2008): 989-991.
[60] Lecaplain, C., Hideur, A., Février, S., & Roy, P. "Mode-locked Yb-doped Bragg fiber laser." *Optics letters* 34.18 (2009): 2879-2881.
[61] Schreiber, T., Ortaç, B., Limpert, J., & Tünnermann, A. "On the study of pulse evolution in ultra-short pulse mode-locked fiber lasers by numerical simulations." *Optics express* 15.13 (2007): 8252-8262.
[62] Wang, H., Houard, J., Arnoldi, L., Hideur, A., Silaeva, E. P., Deconihout, B., & Vella, A. "Effect of the laser pulse width on the field evaporation behavior of metals and oxides." *Ultramicroscopy* 160 (2016): 18-22.
[63] Cabasse, A., Khadour, A., Maulion, G., Martel, G., Nguyen, H. T., Oudar, J. L., ... & Trétout, B. "QUEL ABSORBANT SATURABLE POUR LES LASERS A FIBRES VERROUILLES EN PHASE: NANOTUBES DE CARBONE OU PUITS QUANTIQUES?."
[64] Lecaplain, C., Baumgartl, M., Schreiber, T., & Hideur, A. "On the mode-locking mechanism of a dissipative-soliton fiber oscillator." *Optics express* 19.27 (2011): 26742-26751.
[65] Baumgartl, M., Ortaç, B., Lecaplain, C., Hideur, A., Limpert, J., & Tünnermann, A. "Sub-80 fs dissipative soliton large-mode-area fiber laser." *Optics letters* 35.13 (2010): 2311-2313.
[66] Lefrançois, S., Kieu, K., Deng, Y., Kafka, J. D., & Wise, F. W. "Scaling of dissipative soliton fiber lasers to megawatt peak powers by use of large-area photonic crystal fiber." *Optics letters* 35.10 (2010): 1569-1571.
[67] Grelu, Philippe, and Nail Akhmediev. "Dissipative solitons for mode-locked lasers." *Nature Photonics* 6.2 (2012): 84-92.
[68] Cabasse, A., Ortaç, B., Martel, G., Hideur, A., & Limpert, J. "Dissipative solitons in a passively mode-locked Er-doped fiber with strong normal dispersion." *Optics express* 16.23 (2008): 19322-19329.
[69] Chichkov, N. B., Hausmann, K., Wandt, D., Morgner, U., Neumann, J., & Kracht, D. "High-power dissipative solitons from an all-normal dispersion erbium fiber oscillator." *Optics letters* 35.16 (2010): 2807-2809.
[70] Nie, B., Pestov, D., Wise, F. W., & Dantus, M. "Generation of 42-fs and 10-nJ pulses from a fiber laser with self-similar evolution in the gain segment." *Optics express* 19.13 (2011): 12074-12080.
[71] Renninger, William H., Andy Chong, and Frank W. Wise. "Self-similar pulse evolution in an all-normal-dispersion laser." *Physical Review A* 82.2 (2010): 021805.
[72] Liu, H., Liu, Z., Lamb, E. S., & Wise, F. "Self-similar erbium-doped fiber laser with large normal dispersion." *Optics letters* 39.4 (2014): 1019-1021.
[73] Tang, M., Wang, H., Becheker, R., Oudar, J. L., Gaponov, D., Godin, T., & Hideur, A.

"High-energy dissipative solitons generation from a large normal dispersion Er-fiber laser." *Optics letters* 40.7 (2015): 1414-1417.
[74] Scott, Ryan P., Carsten Langrock, and Brian H. Kolner. "High-dynamic-range laser amplitude and phase noise measurement techniques." *IEEE Journal of selected topics in quantum electronics* 7.4 (2001): 641-655.
[75] Hoover, Erich E., and Jeff A. Squier. "Advances in multiphoton microscopy technology." *Nature photonics* 7.2 (2013): 93-101.
[76] Xu, C., and F. W. Wise. "Recent advances in fibre lasers for nonlinear microscopy." *Nature photonics* 7.11 (2013): 875-882.
[77] M. Baumgartl, T. Gottschall, J. Abreu-Afonso, A. Díez, T. Meyer, B. Dietzek, M. Rothhardt, J. Popp, J. Limpert and A. Tünnermann, "Alignment-free, all-spliced fiber laser source for CARS microscopy based on four-wave-mixing", *Opt. Express*, 20, pp. 21010-21018 (2012)
[78] S. Lefrancois, D. Fu, G. R. Holtom, L. Kong, W. J. Wadsworth, P. Schneider, R. Herda, A. Zach, X. S. Xie, F. W. Wise,"Fiber four-wave mixing source for coherent anti-Stokes Raman scattering microscopy", *Opt. Lett.* 37, pp. 1652-1654 (2012)
[79] E. S. Lamb, S. Lefrancois, M. Ji, W. J. Wadsworth, X. S. Xie and F. W. Wise, "Fiber optical parametric oscillator for coherent anti-Stokes Raman scattering microscopy," *Opt. Lett.*, 39, pp. 4154-4157 (2013)
[80] T. Gottschall, T. Meyer, M. Baumgartl, B. Dietzek, J. Popp, J. Limpert, and A. Tünnermann, "Fiber-based optical parametric oscillator for high resolution coherent anti-Stokes Raman scattering (CARS) microscopy," *Opt. Express* 22(18) 21921-21928 (2014)
[81] Horton, N. G., Wang, K., Kobat, D., Clark, C. G., Wise, F. W., Schaffer, C. B., & Xu, C. "In vivo three-photon microscopy of subcortical structures within an intact mouse brain." *Nature photonics* 7.3 (2013): 205-209.
[82] Dinda, P. T., Seve, E., Millot, G., Sylvestre, T., Maillotte, H., & Lantz, E. "Raman-assisted three-wave mixing of non-phase-matched waves in optical fibres: application to wide-range frequency conversion." *Optics communications* 192.1 (2001): 107-121.
[83] Gu, Chenji, Christiane Goulart, and Jay E. Sharping. "Cross-phase-modulation-induced spectral effects in high-efficiency picosecond fiber optical parametric oscillators." *Optics letters* 36.8 (2011): 1488-1490.
[84] Chong, S. P., Merkle, C. W., Cooke, D. F., Zhang, T., Radhakrishnan, H., Krubitzer, L., & Srinivasan, V. J. "Noninvasive, in vivo imaging of subcortical mouse brain regions with 1.7 μm optical coherence tomography." *Optics letters* 40.21 (2015): 4911-4914.
[85] Lecaplain, C. *Oscillateurs à fibre femtosecondes haute énergie.* PhD thesis, Université de Rouen, 2010.
[86] Miranda, M., Kotur, M., Rudawski, P., Guo, C., Harth, A., L'Huillier, A., & Arnold, C. L. "Spatiotemporal characterization of ultrashort laser pulses using spatially resolved Fourier transform spectrometry." *Optics letters* 39.17 (2014): 5142-5145.
[87] Allen, L., Beijersbergen, M. W., Spreeuw, R. J. C., & Woerdman, J. P. "Orbital angular momentum of light and the transformation of Laguerre-Gaussian laser modes." *Physical Review A* 45.11 (1992): 8185.
[88] Gabet, Renaud, Elodie Le Cren, C. Jin, M. Gadonna, Bora Ung, P. Sillard, H. G. Nguyen, Y. Jaouën, Monique Thual, and S. LaRochelle. "Complete dispersion characterization of few mode fibers by OLCI technique." *Journal of Lightwave Technology* 33.6 (2015): 1155-1160.
[89] Yao, Alison M., and Miles J. Padgett. "Orbital angular momentum: origins, behavior and applications." *Advances in Optics and Photonics* 3.2 (2011): 161-204.
[90] Yao, X.C., Wang, T.X., Xu, P., Lu, H., Pan, G.S., Bao, X.H., Peng, C.Z., Lu, C.Y., Chen, Y.A.

and Pan, J.W. "Observation of eight-photon entanglement." *Nature Photonics* 6.4 (2012): 225-228.
[91] He, H., M. E. J. Friese, N. R. Heckenberg, and H. Rubinsztein-Dunlop. "Direct observation of transfer of angular momentum to absorptive particles from a laser beam with a phase singularity." *Physical Review Letters* 75.5 (1995): 826.
[92] Curtis, Jennifer E., Brian A. Koss, and David G. Grier. "Dynamic holographic optical tweezers." *Optics communications* 207.1 (2002): 169-175.

Résumé

Les lasers ultra-rapides fibrés sont aujourd'hui incontournables dans de nombreuses applications industrielles et scientifiques du fait de leur stabilité, de leur compacité et des hautes puissances disponibles. Les performances actuelles, rendues accessibles par le développement de fibres à larges aires modales et le concept d'amplification à dérive de fréquence, sont toutefois complexes à mettre œuvre et limitées par l'utilisation de composants massifs pour les étapes de compression et d'étirement des impulsions. Ces travaux de thèse, à la fois expérimentaux et numériques, avaient pour objectif d'explorer des régimes dynamiques originaux basés sur l'utilisation de fibres actives spécifiques combinant large aire modale et propriétés dispersives adéquates pour la génération d'impulsions ultra-courtes de haute énergie. Les études numériques ont ainsi permis de montrer que des régimes impulsionnels à haute dispersion normale pouvaient être atteints en exploitant les phénomènes de résonnance et de couplage de modes dans des fibres de Bragg ou à profil en W. L'étude de l'influence des paramètres de la cavité laser sur le mécanisme de verrouillage de modes a permis d'identifier des configurations attractives pour la montée en puissance. La mise en œuvre expérimentale de ces concepts a notamment permis le développement d'une source laser à soliton dissipatif produisant des impulsions énergétiques (38 nJ, 700 fs après compression) à des longueurs d'ondes autour de 1560 nm, record pour ce type d'oscillateur. La réalisation expérimentale de sources ultra-rapides basées sur des fibres actives spécifiques combinées au phénomène de couplage de mode ont permis d'identifier les potentialités et limitations de ces architectures originales à fortes dispersions totales pour la montée en énergie.

Mots clés : laser à fibre, laser ultra-rapide, absorbant saturable à semi-conducteur, fibre de Bragg, haute énergie.

Abstract

Ultrafast fiber lasers represent today a ubiquitous technology in various industrial and research applications thanks to their inherent advantages such as compactness, stability and high power. The best performances to date, mostly relying on large mode area fibers and chirped pulse amplification, however require complex experimental developments and are limited by the use of bulk components for pulse stretching and compression. The experimental and numerical work presented in this PhD thesis aimed at exploring original dynamical regimes based on specific active fibers combining large mode area and high dispersions for the generation of high-energy ultra-short pulses. The numerical studies then showed that pulsed regimes with high normal dispersions could be reached by exploiting resonance and mode-coupling phenomena in Bragg or W-type fibers. Studying the influence of the cavity parameters on mode-locking mechanisms allowed to target attractive configurations for energy scaling. The experimental implementation of this concept allowed the development of a dissipative soliton source delivering record high-energy chirped pulses (38 nJ, 700 fs after compression) at 1560 nm. The realization of ultrafast sources based on specific active fibers combined to mode-coupling phenomena then brought the possibility to identify the potentiality and limitations of these particular architectures with high dispersions for energy scaling.

Keywords: fibre laser, ultrafast laser, semiconductor saturable absorber, Bragg fibre, high energy.